Micromechanics Based Model for Long Fibre Polymer Matrix Composite Materials using a Functionally Graded Interphase

by

Trevor Donald Sabiston

A thesis
presented to the University of Waterloo
in fulfillment of the
thesis requirement for the degree of
Doctorate of Philosophy
in
Mechanical and Mechatronics Engineering
Waterloo, Ontario, Canada, 2018

Examining Committee Membership

The following served on the Examining Committee for this thesis. The decision of the Examining Committee is by majority vote.

External Examiner	Augustin Gakwaya Professor
Supervisor	Kaan Inal Associate Professor
Internal Member	Pearl Sullivan Dean of Engineering, Professor, P.Eng
Internal Member	Sanjeev Bedi Professor, P.Eng
Internal-external Member	Maria Anna Polak Professor, P.Eng

I hereby declare that I am the sole author of this thesis. This is a true copy of the thesis, including any required final revisions, as accepted by my examiners.

I understand that my thesis may be made electronically available to the public.

Abstract

In order to incorporate more composite materials in mass production vehicles within the automotive industry, compression moulding manufacturing techniques have been developed. Using processes such as Sheet Moulding Compound (SMC), and Direct Long Fibre Thermoplastic (DLFT), composite parts can be manufactured at a cycle time quick enough for use in mass production vehicles. Composites present a large opportunity to reduce vehicle mass as they have high specific strength and stiffness compared to metallic structural materials. They also do not corrode and are more formable then equivalent metallic materials. However, in order to design a vehicle in the virtual space one needs to be able to accurately predict the response of the materials used in crash simulations.

The microstructure of SMC and DLFT parts is very different from the laminated composite structures used in other industries. The orientation of the fibres in the material changes during the manufacturing process. The resulting fibre orientations are three dimensional in nature. The existing theories that have been developed for modelling laminated two dimensional composite materials are not applicable to these materials, especially for predicting material failure. To predict failure in composite materials details of the micromechanics are required, as they drive the failure phenomena. A framework which is three dimensional and takes the fibre orientation into account is required to accurately model these material systems.

A micro mechanics homogenization technique is developed where the material properties in the region surrounding the fibre change as a function of position within a unit cell representative of the composite. The change of properties around the fibre is known as a functionally graded interphase (FGI). This modelling method quasi satisfies the equilibrium condition between the fibre and matrix. Through the use of an interphase instead of an interface, it allows any number of aligned fibres to be represented as a single representative fibre. The stresses in the fibre and matrix are combined to predict the elastic stress strain response of a composite.

A generalized solution to this problem is developed, where the stress changes as a function of position within the FGI. This allows the modelling framework to be applied to instances where the matrix material is plastically deforming. The strain in the representative fibre is determined using Eshelby's solution to the inclusion problem from the strain applied to the far field of the composite unit cell (or finite element). Since the strain in the representative fibre and bulk matrix material is different a third deformation region called the interphase matrix is included within the FGI and accommodates the additional strain through a compatibility condition. The resulting solution allows for the stress and

strain in the fibres, the bulk matrix and the matrix material adjacent to the fibre to be separately determined and used in the prediction of failure.

The model is further developed by considering what happens when a composite material is unloaded and the stresses return to zero. The elastic strain in the bulk matrix material is related to the elastic strain in the fibre allowing for a more direct method of strain partitioning when the matrix is plastically deforming around an elastic inclusion. This is more computationally efficient than existing methods for incremental strain partitioning.

To incorporate fibre orientation in the model, a discrete number of representative fibre orientations are considered. A volume fraction of fibres is assigned to each of these orientations to predict the homogenized response of a compression moulded composite. Through studying three SMC microstructures under various applied strains it is determined that sixty representative fibres and associated fibre volume fractions are required to predict the response of an SMC material. This can be used to predict the response of the composite material required for the development cycle of new vehicles for the automotive industry.

Acknowledgements

I would like to acknowledge my supervisor Professor Kaan Inal for his excellent supervision in the completion of my doctoral studies. I would have not been able to complete my studies without funding, industrial support, and collaborations which I established through him. I would like to acknowledge the other members of Professor Kaan Inal's, computational mechanics research group for their contributions and aid in my research. In particular, I would like to thank former group members Mohsen Mohammadi, and Shari King for their contributions and idea sharing while they were here. I would like to acknowledge Jonathan Tham for working with me on SMC composite materials for General Motors. I would like to acknowledge the assistance of Chris Kohar for teaching me how to use some of the software required to complete my studies such as LS-DYNA and FORTRAN.

I would like to acknowledge the support I had from General Motors Canada in the completion of my research activities. I would like to acknowledge Justin Gammage for his support in my early research. I would like to acknowledge Dan Mepham for supervising the research project from General Motors Canada. I would like to acknowledge David Yu for providing materials for testing as well as Alwin Xu for working on related projects.

I would like to acknowledge the other researchers who I have collaborated with, Professor Mohammed Cherkaoui who is an expert in the field of homogenization and Eshelby mechanics for his help in the initial formulation of strain localization. Julie Lévesque for providing expertise and support on the mechanical testing of composite materials. Pascal Pinter for collaborating and providing fibre orientation data for the SMC material used herein. Pascal Pinter also wrote the code required to produce the fibre orientation histogram plots presented in Appendix A. Anna Trauth for completing three-point bend test on the SMC composite material. Both Anna and Pascal are students at Karlsruhe Institut für Technologie working with Professor Kay André Weidenmann.

I would like to acknowledge my family without whom I would have never been encouraged to study engineering. My grandfather Malcolm Sabiston (University of Toronto, Engineering Physics) for always pushing me to do things with my hands when I was younger. My parents John Sabiston (University of Toronto, Electrical Engineering), and Vida Stripinis (University of Toronto, Chemical Engineering) for influencing me towards an engineering career even though I chose to go to a different school. I would also like to acknowledge the assistance of my mother Vida Stripinis for proofreading and editing this thesis. I would finally like to acknowledge my wife Cailin Munroe for putting up with me and supporting me over the length of my doctoral studies, even though I originally expected to finish in only three years. I would also like to acknowledge our dogs Nida and Bailey for providing moral support over the years of my studies.

I would like to acknowledge the negligent vehicle operator who struck me with their pickup truck on April 25^{th}, 2012 while I was riding a bicycle and launched me over the length of their truck. I consider the rupture of the anterior cruciate ligament in my left knee when it took the brunt of the impact on the grill to hood transition of their truck the "Big Bang" required to start me on my graduate school journey. The subsequent four surgeries required to repair the damage they inflicted on my left knee have also had a significant impact on the length of my studies.

I would like to acknowledge funding from the Natural Sciences and Engineering Research Council of Canada (NSERC) PGSD2-489295-2016.

Dedication

I dedicate this thesis in the memory of Pranas "Frank" Stripinis who always wanted to have a doctorate in the family.

Table of Contents

List of Tables

List of Figures

List of Abbreviations

BMC	Bulk moulding compound
CT	Computed tomography
DLFT	Direct long fibre thermoplastic
FE	Finite element
FGI	Functionally graded interphase
FGM	Functionally graded material
NASA	National Aeronautics and Space Administration
PA	Polyamide
PIA	Polyamideimide
PC	Polycarbonate
PEEK	Polyethyletherketone
PMMA	Polymethylmethacrylate
RVE	Representative volume element
SMC	Sheet moulding compound

List of Symbols

$\mathbb{A}$	Fourth order fibre orientation tensor
$\mathbf{A}$	Second order fibre orientation tensor
A_{cm}	Free energy function
A_f	Fibre area or area fraction
$A_{f(i)}$	Fibre area fraction for a specific orientation
A_{intf}	Area of interface within a region of interest
a	Coefficient to relate the equivalent stress to fibre volume content
$\bar{\mathbf{B}}$	Deviatoric left Cauchy Green tensor
B	Placeholder variable to simplify expression of equations
b	Coefficient to relate the equivalent stress to fibre volume content
C	Placeholder variable to simplify expression of equations
C_t	Cohen-Turnbull constant
$\bar{\mathbf{D}}$	Deviatoric deformation rate
$\mathbf{D}_v$	Viscous deformation rate
D	Placeholder variable to simplify expression of equations
d	Derivative
E	Modulus
E_f	Fibre modulus used in defining interphase functions or for isotropic fibres
E_{f_A}	Fibre axial Young's modulus
E_{f_T}	Fibre transverse Young's modulus
E_m	Matrix Young's modulus
e	Natural exponent also used as exp
e_i	Error
$\mathbf{F}$	Deformation gradient
$\mathbf{F}_{im}$	Interphase matrix deformation gradient
$\bar{\mathbf{F}}$	Deviatoric deformation gradient
$\dot{\bar{\mathbf{F}}}$	Time derivative of the deviatoric deformation gradient
$\mathbf{G}$	Displacement gradient
$\mathbf{G}_{im}$	Interphase matrix displacement gradient
$\mathbf{G}_{rf}$	Representative fibre displacement gradient
G_b	Shear modulus for bond stretching stress
$G_{f_{TA}}$	Fibre transverse axial shear modulus
g	Gravitational constant
ΔH_0	Activation enthalpy

$\mathbb{I}$	Fourth order identity tensor
$\mathbf{I}$	Second order identity tensor
$_i$	Used in indicial notation to go between 1:3 or 1:6 depending on tensor order
$_j$	Used in indicial notation to go between 1:3 or 1:6 depending on tensor order
J	Volume ratio
K_m	Matrix bulk modulus
k	Interphase parameter related to the inner bound
$_k$	Used in indicial notation for fourth order tensors and stress components
k_B	Boltzmann constant
$\mathbb{L}$	Elasticity tensor
$\mathbb{L}_f$	Fibre elasticity tensor
$\mathbb{L}_m$	Matrix elasticity tensor
$\mathbb{L}_{UD}$	Unidirectional homogenized elasticity tensor
$\mathcal{L}$	Pseudo elastic tensor
$\bar{\mathbf{L}}$	Deviatoric velocity gradient
l	Interphase parameter related to the outer bound
$_l$	Used in indicial notation for fourth order tensors
ln	Natural logarithm
m	Interphase parameter defining the functionality of a quartic or exponential interphase function
N_s	Density of slip links
n	Number of fibres or orientations
$\hat{n}$	Fibre orientation unit vector
o	Order of a polynomial function
P	Pressure
p	Proportionality constant for interphase volume proof
$\mathbf{Q}$	Transformation tensor to describe the rotation of the representative fibre coordinate system
q	Interphase parameter used in the exponential interphase function
q_k	Eigenvector of the left Cauchy Green tensor ($\bar{\mathbf{B}}$)
$\mathbf{R}$	Rotation tensor part of the deformation gradient decomposition
R	Universal gas constant
r	Radius used in interphase functions
r^2	R-squared regression fit

r_{fit}	Fitting constant
r_{if}	Interphase finish radius
r_{is}	Interphase start radius
r_{ri}	Representative interface radius
r_f	Fibre radius (actual)
r_{rf}	Representative fibre radius
$\mathbb{S}_f$	Eshelby's inclusion tensor for a given fibre shape
$\mathbf{S}_b$	Bond stretching stress
$\dot{\mathbf{S}}_b$	Time derivative of the bond stretching stress
$\hat{\mathbf{S}}_b$	Jaumann rate of bond stretching stress
$\mathbf{S}_c$	Conformational stress
$\mathbb{T}$	Strain localization tensor
$\mathbb{T}_{mt}$	Mori Tanaka strain localization tensor
T	Temperature
T_∞	Vogel temperature
T_{fft}	Final fictive temperature
T_{fic}	Fictive temperature
T_{gl}	Glass transition temperature
Δt	Time step
$_{(t)}$	At the current time step
$_{(t+1)}$	At the next time step
$\mathbf{U}$	Right stretch tensor
u_i	Displacement of a point in terms of the reference axis system
u	Number of data points
$\mathbf{V}$	Left stretch tensor
V_f	Fibre volume fraction
$V_{f(i)}$	Orientation specific fibre volume fraction
V_{intp}	Volume of interphase material within a region of interest
V_m	Matrix volume fraction
V_p	Pressure activation volume
V_{rf}	Representative fibre volume fraction
V_s	Shear activation volume
$v_{\Delta E}$	Volume of difference of moduli
$v_{\Delta\sigma}$	Volume of difference of stress
$\mathbf{W}$	Spin tensor
W_f	Fibre weight fraction
w_f	Fibre weight
w_{fm}	Filled matrix weight

X	Coordinate direction in global coordinates
x_i	Coordinate direction for an orthogonal coordinate system in the reference frame
Y	Coordinate direction in global coordinates
Z	Coordinate direction in global coordinates
α	Inextensibility of polymer chains
γ	Shear strain alternate definition
δ_{ij}	Kronecker delta
Δ	Used to represent an increment
ε	Strain
$\Delta\varepsilon$	Strain increment
ε_0	Rejuvenation strain range
ε_{bm}	Bulk matrix strain
$\varepsilon_{bm}^{(e)}$	Bulk matrix elastic strain
ϵ_{bm}	Bulk matrix strain rotated to representative fibre direction
ε_f	Fibre strain
ε_{rf}	Representative fibre strain
ϵ_{rf}	Representative fibre strain aligned with the representative fibre
ε_{im}	Interphase matrix strain
ε_m	Matrix strain
ε_v	Viscous strain
η	Freedom of movement in slip links
θ	Euler angle for fibre orientation, or integration angle
$\bar{\lambda}_k$	Eigenvalues of the left Cauchy Green tensor ($\bar{\mathbf{B}}$)
ν_f	Fibre Poisson's ratio for isotropic fibres
$\nu_{f_{AT}}$	Fibre axial transverse Poisson's ratio
ν_{f_T}	Fibre transverse Poisson's ratio
$\nu_{f_{TA}}$	Fibre transverse axial Poisson's ratio
ν_m	Matrix Poisson's ratio
π	Mathematical constant relating the diameter and circumference of a circle
ρ	Density
ρ_c	Composite density
ρ_f	Fibre density
ρ_{fm}	Filled matrix density
ρ_m	Matrix density

σ	Stress
σ_{bm}	Bulk matrix stress
σ_{eq}	Von Mises equivalent stress
σ_f	Fibre stress
σ_{im}	Interphase matrix stress
σ_m	Matrix stress
σ_{mean}	Mean stress
σ_{oct}	Octahedral stress
τ	Relaxation time
τ_0	Linear relaxation time at the reference conditions
ϕ	Euler angle for fibre orientation
$\Psi()$	Fibre orientation distribution function

Note on Indicies

Indicial notation is used to represent the coordinate directions with indices $_i$ and $_j$. For tensors indices of 1 through 6 are used to describe directions with 1 to 3 representing the x coordinate directions or normals and 4 through 6 are used to represent shear where the indices $44 = 12$, $55 = 23$, and $66 = 13$. It is assumed that stress and strain are symmetric in a region of interest.

Note on Tensors

Tensors will be represented by bold font for second order tensors and blackboard bold font for fourth order tensors as $\mathbf{I}$ and $\mathbb{I}$ respectively for the identity tensor. It should also be noted that σ and ε are tensors where σ_{ij} and ε_{ij} represent specific stress or strain components within the tensors.

Chapter 1

Introduction

Automotive vehicle material selection is being driven by "fuel economy" regulations, and the increasing inclusion of heavy electronic components for infotainment and advanced powertrains. It is desirable to reduce the mass of the vehicles structure to meet these new regulations and mitigate the inclusion of heavy components [137]. The energy consumption of a vehicle can be broken down into three components: the energy required to overcome terrain, the energy required to overcome aerodynamic drag, and the energy required to overcome frictional forces such as rolling resistance [161]. The vehicle mass has a direct effect on the rolling resistance and overcoming terrain such as driving over hills, which effects the fuel economy. Another added benefit of decreasing the vehicle mass can be observed from Newton's second law, where reducing the mass decreases the force required to accelerate, which in turn aids with vehicle dynamics.

The mass of a material is related to its density. To design lightweight structures, the materials need to be low density, stiff, and strong. Densities of common engineering structural materials is given in Table 1.1.

Current automotive construction is dominated by steel based designs for passenger vehicles, with aluminum becoming more prevalent with the new vehicle regulations. Magnesium is used in some casting applications within the body structure, however it presents a serious corrosion issue when the vehicles are exposed to the environment. Other metallic materials such as steel and aluminum are also subject to corrosion. An opportunity exists in replacing metallic structures with composite materials for automotive applications as their densities are lower than any of the metallic structural materials. The density of composite materials (ρ) is governed by the rule of mixtures as

$$\rho = V_f \rho_f + (1 - V_f)\rho_m \tag{1.1}$$

Table 1.1: Densities of selected engineering materials; alloys, plastics, reinforcement fibres, and composites [59, 45]

Material	Density (kg/m^3)
Aluminum	2700
Carbon fibre	1600-2000
Epoxy	1200-1300
E Glass	2550
E Glass fibre 60% PMC	2000
Kevlar fibres	1440
Kevlar 60% PMC	1380
Polyamide (PA)	1460
Polyamideimide (PAI)	1380
Magnesium	1740
Titanium	4510
Steel	7870

where V_f is the fibre volume fraction, ρ_f is the fibre density, and ρ_m is the matrix density. The challenge in using composite materials is that the behaviour of the material is more difficult to predict than that of a metallic structure and the high cost associated with manufacturing techniques that have been previously used in the aerospace industry. The high cost has limited the use to high end vehicles for structural applications such as by Automobili Lamborghini in the early 2000's [66]. The manufacturing techniques use hand placed layers of unidirectional or woven composite sheets in a mould which is then processed to create the final part. This process is both labour and time intensive. Composites materials are very good in energy absorption applications such as structural safety members. They have more energy absorption mechanisms than metallic materials making them excellent candidates for replacing metallic structures in the vehicle body in white [43]. Recently the application of composite structures in automotive crush structures has been investigated with promising results [42, 186].

In this thesis, the composite materials under consideration are limited to two phase composites with long fibre reinforcements and polymer matrix materials. The polymer matrix materials under consideration are both thermoplastics and thermosets which can be used to manufacture composites with a quick production cycle time. Long fibres are described as having an aspect ratio (length to width) of over 100:1 allowing the end effects to be ignored. The fibres in consideration have a nominal diameter of approximately 10 μm.

Lower cost fibre glass composite materials have been used to manufacture the body work for every generation of Chevrolet Corvette since it was introduced in 1953. Low cost composite materials manufacturing techniques are required to use composite materials in high volume production vehicles to keep the material competitive with existing metallic technologies. Compression moulding materials and techniques exist such as Sheet Moulding Compound (SMC), Bulk Moulding Compound (BMC), and Direct Long Fibre Thermoplastics (DLFT). These compression moulding materials allow for forming similar to metallic materials with orders of magnitude lower production cycle times than traditional hand laid composites. The fibre content of compression moulding composites range between around 20 and 60 weight percent fibres. The structures made of these materials are complex and three dimensional in nature and do not behave as laminated composites. The theory to predict the response of laminated composites in the elastic regime has been well developed along with associated failure modes. However, the mechanics to describe the behaviour of three dimensional composite structures is less well developed. A model which is capable of capturing all composite failure modes is also required. Talreja has described this need to create a framework capable of including all existing composite failure theories [165].

Automotive design has become reliant on computer aided engineering simulations such as Finite Element (FE) methods to design and validate components for crash worthiness early in the design cycle. In order to incorporate composite materials within vehicles, the automotive industry requires material models capable of simulating their response. For the purpose of automotive design, analysis is limited to FE analysis using two dimensional shell elements of at least 5 mm in size for component level and full car crash simulations. However, this level of analysis may not be accurate enough to predict the response of complex shaped three dimensional composite structures. It is accepted that to be able to predict failure of composite materials the micromechanics response is required [165]. In order to optimize composite structures for automotive applications there is a need for a robust model, which accounts for the micromechanics of deformation for composite materials as well as their failure.

Micromechanics models are based on the interaction between the two phases in a composite material. It is common to create representative volume elements (RVE's) based on assumptions about the fibre packing to model the interaction between the fibres and matrix in a composite material. It is desired to create a modelling framework where the three-dimensional response of a long fibre composite material is predicted from the material properties of the two constituents. For compression moulding manufacturing techniques the fibre orientation distribution must be taken into account. The research hypothesis is:

The micromechanics response of a long fibre reinforced composite ma-

terial can be captured using a single unit cell, which takes into account the properties of the reinforcing fibre, the matrix and the mechanical interaction between the two represented by a functionally graded interphase by subdividing a region of interest into a number specific fibre orientations.

The material response of a polymer matrix long fibre composite material is a function of the response of its constituents, with the interaction between the fibres and matrix being accounted for through a functionally graded interphase. In the model a unit cell homogenizes the response from a micro level to a meso scale for use in computer aided engineering of automotive structures made out of long fibre reinforced composite materials. The model accounts for the response of the composite up to the point of failure and is formulated to allow for future implementation of failure theories.

1.1 Summary of Model Requirements

The requirements for the model are:

- Incorporate three dimensional
- Work for all loading directions
- Capture both elastic and plastic response
- Design for implementation of failure as a future enhancement
- Incorporate fibre orientation data
- Be computationally efficient
- Be size independent
- Develop for LS-DYNA FE software

Chapter 2

Literature Review

To achieve the goals outlined in the introduction, an understanding of composite materials is required and the relevant literature has been studied. To combine the material behaviour of the two phases, information regarding the material behaviour of the individual phases is required. The interaction between the phases and methods to describe the micromechanics are required. Understanding of existing homogenization schemes is necessary to develop a computationally efficient model. The mechanics of composite failure is necessary to develop the model such that failure can be implemented in the future. In order to incorporate fibre orientation, familiarity with methods others have used is necessary.

2.0.1 Existing Material Models in LS-DYNA

Due to the desire of these models to be used in the automotive industry the capabilities of the models in LS-DYNA must be known. LS-DYNA contains several material models developed specifically for composite materials are given in Table 2.1. These built in material models only capture the elastic response of laminated composites with some common failure theories accounted for. Therefore, in order to use LS-DYNA to model compression moulded composite materials a user defined material subroutine is required. Additionally details of the micromechanics response are desired for the future implementation of failure theories.

Table 2.1: Composite material models available in LS-DYNA

Material card	Name	Description
MAT_22	Composite Damage	Orthotropic elastic with Chang and Chang damage for laminates
MAT_54,MAT_55	Enhanced Composite Damage	Orthotropic elastic with damage
MAT_58	Laminated Composite Fabric	Orthotropic elastic with failure for laminates
MAT_59	Composite Failure Model	Orthotropic elastic with failure for laminates, works with solid elements
MAT_116	Composite Layup	Elastic response of composite layups
MAT_161, MAT_162	Composite MSC	Progressive failure of composite layups
MAT_219	CODAM2	Composite damage model for transversely isotropic laminates
MAT_235	Micromechanics Dry Fabric	Realignment of fabrics when formed
MAT_261	Laminated Fracture Daimler Pinho	Damage model for laminated orthotropic composites
MAT_262	Laminated Fracture Camanho	Damage model for laminated orthotropic composites

2.1 Phase Properties

In this section, the material properties of the phases in the composite materials of interest are discussed. In particular, modelling of the polymer matrix material and characterization is discussed in detail.

This research is focused on materials made by the combination of two distinct phases, however additional phases occur due to the combination of the two materials known as an interphase. For nano-composites where the fibre diameter is on the scale of nano-meters it is common to describe a third phase or interphase between nano reinforcements and the matrix material. Herasati et al. describe the interphase size based on the variation of the density of the polymer in the vicinity of carbon nanotubes [94].

2.1.1 Fibre Properties

It is widely accepted that carbon based reinforcing fibres exhibit transversely isotropic elastic material behaviour. Adams and Crane found that AS(industrial designation) class graphite fibres exhibit transversely isotropic material behaviour with a modulus 16 times greater in the axial direction than the transverse direction [13]. King et al. have also found that both pan and pitched based carbon fibres exhibit transversely isotropic behaviour [117]. Chamis working with the National Aeronautics and Space Administration (NASA) has published a list of the transversely isotropic properties for common reinforcing fibres [44].

Kant and Penumadu have investigated the fracture properties of individual carbon fibres by creating nano-scale surface defects to measure the fracture toughness and fracture patterns [114]. Sun et al. have shown that natural fibres have transversely isotropic properties, and using a transversely isotropic model is required for accurate prediction of composite properties [162]. The precursor used to manufacture carbon fibres affects the fibre failure modes due to the local atomic structure of the fibres [40]. Therefore, for the purpose of model development, transversely isotropic fibre properties will be assumed since they can be simplified to isotropic depending on the fibre material.

2.1.2 Polymer Experimental Characterization

Buckley et al. have characterized the strain rate sensitivity of epoxy using split Hopkison bar apparatus near the glass transition temperature with strains beyond 100% [36].

Richeton et al. have conducted experimental characterization of polycarbonate (PC), polymethylmethacrylate (PMMA) and polyamideimide (PIA) under a range of strain rates and temperatures under compression [146]. Increasing the strain rate will increase the stiffness and yield stress, which has a similar effect to decreasing the temperature and is caused by an increased resistance to polymer chain mobility [146]. Richeton et al. also noted that there is an increase in temperature due to adiabatic heating from deformation which cannot be ignored in material modelling [146].

Service conditions for polymer matrix composite have been found to have a profound effect on the degradation of material properties. In particular, the response of the polymer matrix is affected by temperature and humidity. An extensive review of polymer aging has been completed by Hutchison [107]. Humidity, temperature, and length of time exposed to both has shown to have an effect on the properties of polymers and their composites. Adams and Crane found that the temperature and humidity of samples affect their performance in terms of failure; in particular, the environmental effects on epoxy [13]. Shikhmanter et al. found that samples conditioned at elevated temperature and humidity experienced more fibre matrix debonding upon failure [156]. Olmos and Gonzalez-Benito have observed that the presence of water affects the interphase between a fibre and matrix [136]. Haghighi et al. have measured the moisture uptake of polycarbonate polymers [77].

Dasappa et al. conducted creep experiments on glass fibre mat reinforced thermoplastics to find the temperature and stress effects on strain [51]. Dassappa et al. have also decoupled the viscoplastic strain from the creep performance of the same composites by reloading the specimen multiple times at the same load for increasing time and examining the effect on creep [52]. Both temperature and humidity have effects on the overall performance of composites, however the exposure histories are required to assess the environmental effects on the composite. Therefore, although important, the environmental effects are excluded from the models presented in this thesis.

2.1.3 Polymer Modelling

Polymers exhibit different mechanical behaviour than other common engineering materials such as metals or ceramics. This is largely attributed to polymers not having a regular crystallographic arrangement, which metals and ceramics have. Instead, polymers have long hydrocarbon chains, which are intertwined and in the case of thermosetting polymers contain cross-links between the hydrocarbon chains. Metals deform plastically through dislocations of planes of atoms in the crystal structure [106]. Polymers deform plastically through the chains moving past each other and straightening out [177]. Early work on

explaining the deformation mechanics of polymer materials was done by Robertson [148] who based his model on shear stress and Eyring's model. Eyring's model is another fundamental work on the mechanics of polymers [64]. As polymers behave differently than metals, new constitutive laws were required to model the material behaviour. The phenomenological constitutive behaviour of metal is well established in the classic works of Hill on the subject of metal plasticity [96].

The strain rate sensitivity of necking under uniaxial tension was discussed by Hutchinson and Neale in 1977 [108]. In this work, the strain rate sensitivity and localization phenomena of viscous materials was defined in terms of overall strain in the material in a phenomenological sense. This work is seen as one of the early models, which could be adopted for use in modelling the plastic response of polymers. In 1983 Hutchison and Neale discussed the neck propagation of polymeric materials [109], in this work they captured the softening and subsequent hardening exhibited by polymer materials in a phenomenological model [109]. While these phenomenological based models can be fit to the stress-strain response of polymers, they do not contain enough detail to predict the full response of polymers under different loading and environmental conditions. Models based on the physical mechanisms for polymers are required for predictive models of polymers.

The mechanical behaviour of glassy polymers began to be studied in the late 1980's to improve predictions over the previously used phenomenological models. A few new models emerged to better capture the response of polymeric materials. The first model was developed by the group of Boyce at MIT in 1988 to capture the strain rate temperature and pressure dependence of these materials as well as post yield softening [32]. This work in particular was on poly methyl methacrylate (PMMA) and uses a Eyring dashpot and a Langevin spring to represent the material response and the incorporation of state variables to capture the physical response [32]. Boyce presented further developments in 1989 for use of this model and similar models for both single crystal and glassy polymers through the decomposition of the deformation gradient into a product of the elastic and plastic portion [33]. This model was extended to a full three-dimensional model with eight coupled chains for a constitutive model by Boyce's group in 1993 [17]. Richeton et al. have described how the yield stress changes as a function of temperature and strain rate as an extension to the cooperative model [146]. In Richeton et al. pressure sensitivity on the yield stress is based on the work of Boyce et al. [146, 32].

A group at Eindhoven University led by Govaert have developed an elasto-viscoplastic model for simulating the response of glassy polymers known as the Eindhoven glassy polymer model. They created a constitutive modelling framework for polymers up to yield point using a compressible Leonov model with expansion to multiple modes [166]. The model has been expanded to work for multiple stress relaxation times [174]. They have

modeled the effects of the temperature and strain rate effects on glassy polymers such as PMMA [173].

Another polymer constitutive model was developed around the same time by the group of C.P. Buckley at Oxford University. In this model, the stress is divided into three components: the mean stress arising from volumetric change, the bond stretching stress and the conformational stress [37]. Buckley's group has calibrated this model for various thermoplastic and thermosetting resins including epoxy, PMMA, polystyrene, and poly(ethylene terphthalate) [38, 36, 180, 67]. More details on this model and the implementation into finite element codes is given in [35, 124]. The advantage of this model over the other two is that all of the variables used in the constitutive model are physically based whereas the other models use state variables and fitting parameters which do not have physical bases. The glass rubber model also allows for multiple relaxation times to be accounted for by each relaxation time being given its own volume fraction of the polymer resulting in a relaxation time spectrum.

2.1.4 Functionally Graded Materials

Functionally Graded Materials (FGM) is a special class of materials where the material properties such as thermal or elastic moduli change as a function of position within the material. FGM's were first produced in Japan using a powder metallurgy technique discussed by Koizumi [118]. Birman and Byrd have reviewed works reporting that FGM's have superior energy absorption due to toughness compared to non FGM's [30]. Centrifugal casting is a technique that can be used to manufacture FGM's and the properties of these FGM's has been researched by Mohammadi et al. [131].

Some researchers have used a functionally graded material within composite material models. Benveniste and Miloh have defined a quasi FGI by having multiple spheres of interphase around an inclusion [29], however this does not capture the full functionally graded nature of composite interphases. Jasiuk and Kouider have described an interphase zone where the elastic properties change as a function of radial distance from the fibre described by a linear or power-law relation [112]. This work was extended to provide thermal properties by Ostoja-Starzewski at al. in this method the interphase zone is subdivided into regions where the properties are either that of the fibre or matrix these regions are arranged such that the properties change over the interphase zone [138]. Wang and Jasiuk defined a functionally graded interphase around spherical reinforcements and have successfully captured the elastic response of a composite using this functionally graded interphase [176]. Describing the interaction between a long fibre and matrix has not been

completed using a functionally graded interphase. Additionally, the current definitions only consider elastic deformation of the fibre and matrix a more robust model is required to describe the interaction when there is plastic flow in any of the constituents.

2.2 Micromechanics of Two Phase Composite Materials

Micromechanics involves modelling the interaction between the fibre and matrix to capture the response of composite materials. The importance of modelling composites at different size scales is discussed in a review paper by Hashin who reviewed the existing approaches at different size scales macro, mini and micro [83]. Micromechanics based methods became prevalent in the 1980's, one of the most influential authors on the subject is Jacob Aboudi who has written a textbook on the subject [10] and created the method of cells approach. Talreja concluded that is required to model the exact and complex failure modes of long fibre reinforced composite materials [165].

2.2.1 Composite Representative Volume Elements (RVE)'s

In order to account for the micromechanics of composites, one needs to consider a region in space containing a fibre surrounded by matrix material known as an RVE. The use of RVE's are especially relevant for woven fabrics where the fibre tows are repeated periodically. Hill is given credit of creating the concept of using an RVE [97]. Jacques et al. have proposed a representative unit cell model for 3-D woven textile fabrics where an RVE is used to define the overall constitutive law of the material and homogenize the meso scale model to macro scale [110]. Fliegener et al. have modeled the long fibre reinforced thermoplastics which are injection moulded evaluating the microstructure of the injection moulded samples and simulating the elastic response of the material using finite element analysis [70], however, they were only able to predict the response within 10% of experimental results.

RVE's are also common at micro scale and are the foundation of many of the models and theories for composites. Asp et al. used three different fibre packing arrangements in their finite element analysis of transverse tension failure of composites; square, hexagonal and diagonal square [20]. Asp et al. found that the failure initiation location under transverse tension was dependent on the fibre packing arrangement used [20]. Bulsara et al. have used a representative unit cell for modelling the damage in fibre reinforced composites considering the distribution and packing of fibres [41]. Chen and Liu have used a square

fibre packaging in their boundary element method model for composites [46]. Harper et al. have made a representative volume element to capture the response of a short fibre composite by considering a repeating unit cell for 2-D, and have considered the size effects on statistics of the unit cell such as the number of fibres included [78, 79].

There are two common fibre packing arrangements used when considering a unit cell containing individual fibres, either a square packing or hexagonal packing, which describe the array shape of the centerline of the fibres. There is also interest as how these two arrangements compare to experimentally observed fibre arrangements within composites. Wongsto and Li have researched the effect of fibre packing orientation on the micromechanics of composites, comparing the results from square and hexagonal packing to real random fibre orientations within an RVE [179]. Gommer et al. have developed an advanced image processing technique to determine the microstructure of composites and discovered that the packing arrangement is dependent on the degree of compaction of the composite while manufacturing [75]. The selection of the domain of the RVE is crucial to the overall predictive capabilities of composite models, and careful selection is required to capture the response of interest.

2.2.2 Generalized Method of Cells

Aboudi has derived the equations for the micromechanics of composites containing rectangular fibres within a rectangular region as an RVE [1]. This analysis method is referred to the generalized method of cells in later works, was developed for isotropic elastic metallic based composites [1]. Aboudi has generalized the method of cells to work with elasto-viscoplastic materials [2]. The equations for the method of cells are derived by assuming that the normal and shear stresses are continuous along the interface between the fibre and matrix. However, it is found that this condition cannot be satisfied for two phase composite materials where the phases have different stiffness's. The formulation was changed to have the average displacement match between the phases. It has also been shown that there is a deviation between Aboudi's method of cells and the solution if a cylindrical fibre is used for fibre volume fractions above 0.3 [2]. Therefore, this method has been demonstrated to only be valid for low volume fraction composites, although it has been used to analyse composites at high volume fractions as well.

Aboudi then derived the equations for the micromechanics effects of short fibre composite materials to develop continuum equations based on the micromechanics for an elastic system [3]. This work was extended to include the thermal properties of composites using a similar method as the elastic work [4]. Once again, a rectangular cross section of the

fibres is used and the model is not capable of predicting the plastic response of short fibre composites and is limited to low fibre volume fractions.

Benveniste and Aboudi researched the effects of fibre debonding on wave propagation and mechanical properties for boron epoxy composites using the method of cells [27]. The debonding was modeled using a displacement incompatibility between the fibre and matrix, such that the matrix would displace more when they become debonded [27]. Aboudi extended the method of cells further to model imperfect bonding between the fibres and the matrix, where a damage parameter is introduced to account for an imperfect interface between the fibres and matrix [5].

Aboudi extended the method of cells to micromechanics based strength analysis for long fibre composite materials [6]. In this work, it is assumed that the failure for both the matrix and the fibre are stress driven and three strength parameters are used to evaluate failure [6]. The failure criterion proposed is not very advanced and proposes constants as a cut off limit for failure, such as having one stress level, above which the composite fails. The model was extended to fatigue failure of composites using a micromechanics approach using a similar form to evaluating the strength of unidirectional composites [8]. A review of the implementations of Aboudi's model for the method of cells is given in [7].

Aboudi then implemented a non-linear viscoelastic behaviour of the matrix material to use the method of cells to predict the time dependent response of an epoxy carbon fibre composite [9]. A similar approach was used by Yancey and Pindera to predict the creep response of a graphite epoxy composite using the generalized method of cells [182].

Low et al. have used Aboudi's method of cells and extended it to work with a three-phase composite, where the interphase is also heterogeneous [127]. A quarter symmetry model was adopted for Aboudi's method of cells meaning that the method is not applicable to all loading conditions [127]. Low et al. expanded this methodology to include thermal properties changing as a function of position radially around the fibre [128]. However, in this method the changes in fibre properties happen in a rectangular pattern, which is not representative of the behaviour for round fibres.

Recently Sun et al. have used the generalized method of cells presented by Aboudi to model natural fibre composites [162]. Aboudi's model was selected to model the anisotropic behaviour of natural sisal fibres. The overall macroscopic elastic response of the sisal fibre composite was predicted using the method of cells [162]. Bednarcyk et al. have shown how the generalized method of cells can be applied to vectorized constitutive laws and have studied heat transfer modelling using the method of cells [23].

Aboudi's method of cells does not account for the transversely isotropic nature of common non-metallic fibre materials such as carbon fibre which Chamis has found to

exhibit transversely isotropic behaviour [44]. Although Aboudi's method was developed for isotropic metal composites using a rectangular fibre and only valid for low volume fractions it has been widely accepted and well established, due to shortcomings discussed various micromechanics models have been developed.

2.2.3 Development of Micromechanics Models

Other micromechanics models have been developed for long fibre composites. The focus of much of this effort has been to improve the prediction of transverse properties. Adams and Crane developed a micromechanics model around the same time as Aboudi, which is more applicable for long fibre reinforced composites. Their model uses plane strain symmetry of a quarter symmetric unit cell model where the matrix is elasto-plastic and follows a Prandtl-Reuss flow rule and the fibre is transversely isotropic [13]. Unfortunately this model does not account for loadings in all directions and is incapable of use with bending loads, however it is better for the prediction of transverse material properties than Aboudi's method of cells. An improved model is therefore desirable, which would be applicable to generalized loadings and have improved transverse material response.

2.2.4 Interface versus Interphase in Micromechanics Models

An interface is a surface, which separates two phases in a material. Classically an interface has been used to describe the force transfer between the fibre and the matrix in a composite material. It is also assumed that the force transfer occurs solely through shear stress acting across the surface of the interface known as an interfacial shear stress. The maximum value of interfacial shear stress for a given material pairing is known as the interfacial shear strength and is used in failure prediction. The perfect interface assumption made in many models assumes that the displacement is continuous across the interface i.e. the fibre and matrix displacements are the same.

An interphase is a separate phase located between the two or more other phases of the composite, an interphase occupies a volume whereas an interface has an associated surface area. Benveniste and Miloh have developed a model where there are imperfect interfaces between multiple interphases surrounding the spherical inclusion to account for the deformation of the composite [29]. Benveniste and Miloh have proposed seven different interface conditions depending on the material properties, and that the material properties change radially as a function of position [29]. This model violates stress and strain compatibility between the seven phases and is very complex compared to other micromechanics models.

Another approach to using the interphase for two phase composites is to assume that three phases are present within the material, the fibre, the matrix and the interphase. The interphase is used to account for the stress transfer between the reinforcement and matrix instead of considering the traction forces along an interface as shear stresses. Either strain or stress continuity between the phases is assumed and often neither of these conditions is completely satisfied.

The first implementation of an interphase was by Christensen in 1969 where the properties of composites with spheroidal rigid reinforcements and voids were considered [48]. This work was followed in 1979 by a work where the elastic solution for the interaction between a spheroidal inclusion and a matrix and a transversely isotropic fibre in a matrix are considered for the linear elastic case using an interphase [49]. Benveniste discussed the effects of an imperfect bond with a composite comprised of spherical reinforcements and a near field matrix as well as a far field matrix [24]. Benveniste et al. have discussed the micromechanics and stress fields of composites with coated spherical reinforcements with the coating being an interphase [28]. Achenbach and Zhu have described the load transfer between the fibre and the matrix as occurring through an interphase around a long fibre reinforcement where strain is discontinuous allowing for the load difference between the phases [12]. This model again uses a quarter symmetric unit cell model and is therefore not applicable to bending loads, there is also a strain incompatibility between the three phases which is not physical [12]. Chen and Lui have also used an interphase as a third phase between the fibre and matrix to model the transverse properties of composites [46]. Upadhyaya and Kumar have described the stress transition between the fibre and matrix through an interphase in the fibre pull out test. They described the stress distribution as a function of position around the fibre, for a single fibre being pulled out of a matrix. They compared the analytical results for the axisymmetric problem to a finite element simulation of the problem and found a good match. They have also shown that there is a large transition in the stress around the fibre [172]. An argument against the use of an interphase is that until recently there was little proof of the existence of a third distinct phase.

2.2.5 Experimental Evidence of the Existence of an Interphase

Experimental results support the existence of an interphase. There is no distinct third phase with independently characterized material properties. Instead, the material properties change in the vicinity of the fibre. Recently Karger-Kocsis et al. have conducted a review of the interphase concept discussing various aspects of the interphase such as tailoring the properties through the use of surface modifications of the fibres by sizing agents

[115]. Fibre sizing refers to fibre coatings or surface treatments used by fibre manufacturers to increase fibre wetability with certain matrix materials and is used to promote bonds between the fibre and matrix. It has been found by Yang and Pitchumani that the presence of a reinforcing fibre affects the structure of the polymer matrix in the immediate surroundings of the fibre. Affected are polymer properties like chain length, crystallinity, cross link density, etc. [183]. Concentration gradients of the curing agent for thermosetting polymers near the fibre and fibre sizing cause there to be a gradient in the material properties within the near field of the fibre [183]. The variation in polymer structure occurs within 30-170 nm of the fibre, which is about 0.6-3.4 % of a typical fibre radius away from the fibre [183]. Li et al. have shown using scanning electron microscopy that the concentration of atoms of both matrix and fibre changes as a function of position around the reinforcing fibre [125]. Li et al. have also observed that the degree of crosslinking around the fibre changes as a function of position from the fibre [125].

A review of nano indentation, which is a nano scale measurement of material hardness has been conducted by Gibson, highlighting how a grid pattern of nano indentation is used to evaluate the change in material properties as a function of position around a fibre [74]. Kim et al. have determined that the thickness of the interphase region surrounding a fibre is on the scale of 1 μm and varies depending on fibre sizing [116]. Olmos and Gonzalez-Benito have reported a change in material distribution up to 15 μm away from a fibre attributed to an interphase experimentally observed using nano indentation [136]. There is discrepancy between the size of the interphase experimentally measured by Kim et al. and Olmos and Gonzalez-Benito due to advancements in experimental techniques and the materials considered. Olmos and Gonzalez-Benito have also reported that the elastic moduli of the interphase changes as a function of distance away from the fibre [136]. The overall consensus from these experimental works is that representing the interphase as a phase with distinct properties is not an accurate representation of the natural phenomena. If an interphase is used, the best representation is to have the material properties change as a function of position away from the fibre.

2.3 Homogenization

Homogenization is a modelling technique used to simplify the problem and retrieve the effective properties of a multiphase material from the properties of the constituents without using a full field model. A full field model considers the interaction of the phases considering their actual size. For FE models this would requires a mesh with separation of the individual phases to capture their behaviour. Homogenization techniques are used

to predict the overall behaviour of the composite material from information about the materials and microstructure. Homogenization techniques were created to allow prediction of the effective properties of composites for engineering calculations before FE computer simulations where commonplace.

2.3.1 Classic Homogenization Techniques

The simplest form of homogenization are the bounds imposed by the rule of mixtures and assumes that the strains or stresses in the phases are the same. These bounds are known as the Voigt assumption when the strains in the phases are the same or the Reuss assumption when the stresses in each phase are the same. The Voigt and Reuss assumptions form the upper and lower bounds respectively on the predicted response of composite materials.

The Voigt assumption calculates the overall elastic tensor as a combination of elastic tensors of the phases as

$$\mathbb{L} = V_f \mathbb{L}_f + V_m \mathbb{L}_m \tag{2.1}$$

where V_f is the fibre volume fraction, $\mathbb{L}_f$ is the fibre elasticity tensor, V_m is the matrix volume fraction assuming negligible void content the matrix volume fraction is calculated as $V_m = 1 - V_f$, and $\mathbb{L}_m$ is the matrix elasticity tensor.

For the Reuss assumption the overall composite elasticity tensor is

$$\mathbb{L} = \left[V_f \mathbb{L}_f^{-1} + V_m \mathbb{L}_m^{-1} \right]^{-1}. \tag{2.2}$$

These fundamental assumptions serve as a basis for composite homogenization techniques.

Eshelby described the elastic field in an infinite material containing an inclusion of various shapes based on an ellipsoidal inclusion. The equations were derived for various inclusion geometries; spherical, ellipsoidal, cylindrical, assuming that both the matrix and the inclusion are isotropic elastic materials [62]. Eshelby performed a further study for the elastic field in the region surrounding an inhomogeneity, which is much closer to the inclusion than the initial solutions [63]. Mori and Tanaka used Eshelby's method to describe the strain fields in materials containing multiple inclusions of the same shape and alignment with a given inclusion volume fraction [132]. Benveniste extended the method presented by Mori and Tanaka to a form where it could be used to describe the strain partitioning between two phases in composite materials using Eshelby's solutions [25]. To et al. have derived the expressions for the elastic properties of composite materials in a wave-vector domain and have been able to reproduce the expressions of Eshelby [62] and Mori and

Tanaka [132, 167]. For Eshelby's solution, the strain in the fibre (ε_f) is calculated as a function of the overall strain applied to the far field (ε) through the localization tensor as

$$\varepsilon_f = \mathbb{T}\varepsilon \tag{2.3}$$

where the strain localization tensor $\mathbb{T}$ is

$$\mathbb{T} = \left[\mathbb{I} + \mathbb{S}_f \mathbb{L}_m^{-1} \left(\mathbb{L}_f - \mathbb{L}_m\right)\right]^{-1} \tag{2.4}$$

where $\mathbb{I}$ is the fourth order identity tensor, and $\mathbb{S}_f$ is Eshelby's inclusion tensor for the given fibre shape [144].

Early work on determining the overall elastic moduli of two phase composites was done by Hashin in 1961 and was based on Eshelbian mechanics known as the variational approach [92]. Hashin went on to derive the bounds on the moduli of a two-phase system for metallic materials which was used as a basis for composites [80, 93]. Hashin and Shtrikman have assumed that in a unit cell the stress and strain are the same as the overall composite material and have derived the bounds on elastic response based on the strain energy creating an upper and lower bound on the elastic constants [93]. The methodology was extended to be used with fibrous materials instead of randomly distributed second phase particles in 1964 [89]. In this early work, the fibres are given a hexagonal packing arrangement and it is shown that this can be representative of a random distribution in plane, which is the fibre distribution typical of unidirectional fibre plies [89]. This method was further extended to discuss plane strain loading with transversely isotropic reinforcements [81].

Hill developed theories on the mechanics of composite materials for perfectly bonded two phase composite materials based on the work of Eshelby. In this work, the bounds on the moduli for a composite material are discussed as related to Ruess and Voigt upper and lower bounds on the elastic modulus [97]. This methodology was then extended to work with fibre strengthened materials which are isotropic and elastic [98]. Hill extended this method to work for the case where the matrix acts in an elasto-plastic manner, as should be expected with metal matrix composites [99]. Hill then worked on implementing the self-consistent method for use in two phase isotropic composite with spheroidal inclusions to homogenize the method [100]. This was extended to work with fibre reinforcements for scenarios where the difference in stiffness between fibre and matrix is small and there is a low volume fraction of fibres [101]. Hill has proposed the self-consistent scheme where the orientation average stress or strain in the inclusion is set to be equal to the overall stress or strain applied to the material [100]. The self-consistent scheme gives better results for polycrystalline material where the stiffnesses are similar as opposed to multiphase

composite materials where there is a large difference in the stiffness of the phases [139]. Walpole has described the overall elastic moduli of two phase composites with needle and disc shaped inclusions building on the work of Hill and Eshelby [175].

Pioneering work on laminate theory for composites was completed by Tsai under contract to NASA [168]. In this work, the planar stiffness and strength of unidirectional plies of composite material was derived [168]. The transverse and shear loadings of unidirectional composites were researched by Adams and Doner in 1967 to extend the theory of laminated composites to off axis loadings [14, 15]. Aboudi extended the existing elastic theory developed by Hashin and Tsai to work with elastic viscoplastic composite materials for laminated materials and the wave propagation in these materials [11].

2.3.2 Advanced Homogenization Developments

Cherkaoui et al. have derived the equations for strain localization in materials with coated inclusions where a thin third phase surrounds the inclusion [47]. This is the double inclusion problem and was formulated for elastic materials.

Ghossein and Lévesque have compared homogenization methods for ellipsoidal inclusions to a full field numerical model and have found that for moderate volume fractions of inclusions used in Lielens' technique produces results closest to the numerical solution [73, 126]. For low volume fractions Eshelby and Mori-Tanaka methods produce reasonable estimates. In general, these homogenization techniques of the first order over predict the material response [73].

Ponte Castañeda proposed a variational approach known as the linear comparison composite based on the effective energy potentials to create bounds on the response of nonlinear composites by comparing them to linear composites [140].

Zhou and Meschke have extended the work of Ponte Castañeda to predict the homogenized strength of composites considering both inclusions and voids [187]. Boudet et al. have homogenized the elasto-visco-plastic response of composites with kinematic and isotropic work hardening using an extension to linear comparison composite framework by Ponte Castañeda and the effective internal variable approach [31]. Brassart et al. have used an incremental variational principle to homogenize the response of elasto-visco-plastic composites through another extension to the work of Ponte Castañeda [34]

Doghri et al. have proposed a method to homogenize elasto-visco-plastic composites using a backwards Euler implicit time integration scheme, linearizing the material behaviour over the time step [54]. It is also noted that the use of the Mori and Tanaka homogenization

[132] and Eshelby solution [62] within Doghri's method using these linearized elasto-visco-plastic responses results in the over prediction of the stress strain response where the inclusion is stiffer than the matrix material [54]. Doghri and Ouaar have compared two methods of using the instantaneous tangent modulus and the total secant modulus in the Mori-Tanaka framework compared to finite element full field response [56]. The two methods are based on considering either the incremental instantaneous tangent stiffness or the total secant method where the stiffness is found from the total stress and strain, instead of the instantaneous stress strain relationship where the materials flow according to J_2 plasticity [55]. Doghri et al. also indicate that they are not able to predict the response of random short fibre composites using the first and second order schemes for linearization of the problem using the two-step homogenization procedure since both over-predict the stress strain response compared to a full field FE model [55]. Czarnota et al. have used an additive tangent method for linearization to use the Mori-Tanaka method for materials with elasto-visco-plastic phases with the homogenization verified through full field finite element representative volume element simulations [50].

Dinzart and Sabar have extended Eshelby's method for materials with imperfect interfaces where displacement across the interface is not continuous. A Mori Tanaka approach is used to homogenize the response of elastic materials with imperfect interfaces [53]. Gu and He have derived the elastic moduli for unidirectional fibre reinforced composites with imperfect interfaces where there is a discontinuity of strain around the fibres based on the equations derived by Hill in 1964 [76, 98]. Xu et al. used the generalized self-consistent method to predict the elastic moduli of composites with imperfect interfaces where there is a jump in the stress and displacement across the boundary [181].

Lielens et al. introduced the concept of interpolating between the upper and lower Hashin Shtrikman bounds using a Mori-Tanaka scheme and the fibre volume fraction to improve the accuracy of the model's predictions [126]. Lielens et al. used their interpolation method to predict the response of a two-dimensional structure made out of SMC. Taking the effect of fibre orientation was included using a two-step homogenization procedure where the fibre orientations were grouped into grains of the same orientation [126]. The Mori Tanaka approach is used to homogenize the response of the grains, which are combined using the Voigt assumption of equal strain to homogenize to the overall composite response [126].

Pierard et al. have also used a two-step homogenization procedure for composites with different inclusion shapes and orientation, the first step is to group the like orientation into grains and then homogenize the grains into an overall material response [139]. The homogenization is done in two steps first define the grain homogenization using a method such as the Mori-Tanaka homogenization scheme then homogenize the grains using a generalized

procedure such as the Voigt or Ruess procedure to predict the overall material response [139]. This is different from the work of Lielens through the use of different inclusion shapes and presenting the results of the analysis [139, 126]. The method of using pseudo grains has also been used by Ogierman and Kokot who determined that nine pseudo grains using 27 parameters are required to efficiently subdivide the fibre orientations into enough unique orientations to capture the overall stiffness and stress strain response of a composite with non-spherical inclusions [135].

Tucker and Liang have reviewed techniques for homogenization of short fibre composites, comparing the results to FE for aligned fibres [171]. Müller et al. have compared homogenization techniques to predict the effective modulus of short fibre composites with full field models [133]. Sburlati and Cianci have proposed a model for spherically reinforced matrix materials where there is an interphase surrounding the inclusion and within the interphase the elastic properties transition between those of the inclusion and those of the matrix material as a function of the radial position within the interphase [152]. They have found that the thickness of the interphase effects the response and homogenized properties of the composite containing spherical inclusions [152].

2.4 Failure

Although incorporation of failure is not part of this thesis; future work will involve incorporating failure theories into the framework. It is important to understand failure theories to design the framework for their incorporation. The major composite failure modes are discussed in this section. Many failure and damage models exist for composite materials. In a recent review Talreja discusses the development of failure models and states that none of the existing models is successful at fully capturing all failure modes for composite materials [165]. The first composite failure model was created by Azzi and Tsai and used the method presented by Hill [95] to predict failure [21]. Hoffman proposed that all composite failure is brittle and a brittle fracture model was introduced using nine material parameters [103]. Another well known failure criterion which was used with classical laminate theory is the Tsai and Wu failure criterion [170]. Hashin et al. worked on developing failure models for unidirectional composite laminates by performing further work beyond that of Tsai to define the nonlinear behaviour of composite materials. They used a a Ramberg-Osgood approach to modelling the stress strain response for the transverse and shear directions [88]. Tsai summarized continuum based composite failure models including maximum stress and strain as well as yield functions [169]. Hashin also proposed a piecewise failure criterion for unidirectional composite materials separating the fibre and matrix modes of failure.

This resulted in improvements over the Tsai Wu criteria [82]. Composite failure models can be broken into two categories: one which considers the performance of a composite with accumulated damage and the second where the composite failure is considered. Most composite failure occurs due to micro scale phenomena, which will be further discussed.

Another aspect of composite failure is fatigue. This was first studied by Hashin who created a simple stress life approach for composite laminates [90]. Hashin went on to develop damage models for composite materials for lifecycle analysis of composite structures [91]. This work progressed to theories on the effects of delamination and damage due to delamination of laminated composite materials using a variational approach [84]. This work was furthered to talk about damage and the effects of cracks in laminated composites on their structural properties [85, 86, 87]. Benveniste and Aboudi looked into the crack propagation in laminated composites [26].

Micromechanics based failure models are required since the failure phenomena of composite materials is initiated at the microscale. Jelf and Fleck have categorized the failure of unidirectional composites into four categories, fibre failure, elastic microbuckling, matrix failure and plastic microbuckling [113]. Asp et al. have considered the transverse failure of composites due to matrix failure between the fibres as well as at the interface between the fibre and matrix [18]. Asp et al. have also found that all transverse composite failure is either due to interface failure or matrix microcracking and the initiation of these failure modes is competing [20]. Research into further micromechanics based failure modes is discussed in this section.

2.4.1 Composite Damage

Damage requires a quantification of the severity and quantity of local micro scale failures within the composite material and the composite structures ability to continue to support load. Most of the damage theories relate to laminated composite structures which are not considered in this thesis. Most of the developments of damage models for composites assume only two-dimensions and are not applicable to three-dimensional structures. Zhuang and Talreja have examined the effects of voids on the growth of delaminations and damage in unidirectional composite laminate plates subjected to compressive loading and buckling [188]. Talreja has discussed the failure modes applicable to the damage of laminated composite materials and has stressed the importance of accounting for these failure modes in structural design [164].

Damage detection using nondestructive testing techniques is crucial to knowing the exact damage in a composite. Recently there have been advances in detection technologies.

The damage in a glass fibre laminated composite was investigated by Sket et al. using x-rays and the different micro failure modes were identified for a three-point bend specimen [157]. Scott et al. have demonstrated a new technique using acoustic emission sensing to detect the presence of voids and matrix cracking within composite materials. They have also demonstrated the ability to determine the fibre orientation and spacing using this technique; allowing for microstructure analysis with nondestructive testing [155]. These advanced techniques can be used to better understand the damage accumulation in composites under repeated loadings and allow for improvements in the evaluation of predictive models.

Damage models have been developed to predict the failure of composites through damage accumulation. Bulsara et al. have developed a composite RVE model to consider the damage and failure, a maximum stress criterion. Failure evaluation is based on the matrix strength, fibre strength and interfacial strength. Two damage initiation modes are considered: matrix cracking and fibre matrix debonding. Temperature effects on damage are also studied [41]. This model is applicable to transverse properties and resulting damage but is not generalized to 3-dimensions.

Another major contributing factor to damage in composites are the inherent presence of voids within laminated composites manufactured using hand laid techniques. Ricotta et al. have studied the effect of voids on crack growth in laminated composite fabrics [147]. Lambert et al. have studied the growth of voids during fatigue and the effect of voids on the fatigue life of laminated composites [121]. Garcia et al. have developed a model for spherical inclusions where the effects of debonding of the particles is solved analytically to capture the effects of debonding and the progressive nature of debonding using a coupled fracture energy and stress criterion [71]. The presence of voids is important to the understanding of damage, however the quantity of voids produced using new manufacturing techniques is not documented.

Damage is a useful tool for evaluating the service life of components or their ability to function following an impact event. Damage prediction is also useful when evaluating the overall failure of a component due to an accumulation of failure modes. These developments are beyond the scope of the work outlined in this thesis. However, knowledge of damage theories is important in model development to allow a future implementation of damage frameworks.

2.4.2 Composite Macro Failure

Phenomenological based failure models have been relatively well established for the field of composite laminate theory [170, 21, 82]. These failure criterions are sufficient for overall predictions; however, they have many short comings including the fact that they are unable to account for the various failure initiation modes experienced by fibrous composites.

A worldwide failure exercise containing 19 different approaches for modelling failure of composite materials was conducted from 1998-2004 to bring together all the relevant failure criteria for laminated composites [102]. This exercise has been reviewed by Soden et al., the project comprised of compiling existing failure models for laminated composites. The major shortcomings identified in the available failure models are: no 3-D failure criteria, no delamination initiation and propagation criteria, no creep and fatigue behaviour, no temperature effects, no cyclic loading and limited implementation of the failure criterion into commercial analysis software [160]. More recently a 3-D failure criterion has been developed by Raimondo et al. allowing for a phenomenological fit for unidirectional composites [145], this still does not have predictive capabilities in the case of changing the materials comprising the composite.

Puck and Schürmann developed a failure model for laminated composites at a phenomenological level to predict failure for engineering design. The individual contributions to failure are discussed including multiple modes for fibre failure and inter-fibre failure and the degradation of strength due to fibre failure [142]. This failure model is extended to include three different failure modes and three different laminate configurations by Puck and Schürmann [143]. The calibration and implementation of this laminate failure criterion is discussed by Puck et al. [141]. Dong et al. have improved upon the failure theory developed by Puck and have incorporated fracture mechanics into the phenomenological failure theory [58]. These phenomenological failure criteria are reasonable for use in laminates, however they do not contain the detail required to predict localized failure in composites as are expected to occur in complex automotive structures. Therefore, micromechanics based failure criteria are required to successfully predict the onset and propagation of failure in automotive composite structures.

2.4.3 Fibre Matrix Debonding

Debonding is the process where the bond between the fibre and matrix is broken, leading to no load transfer between the fibre and matrix. Interface debonding is a common failure mode in transverse tension as well as under axial loading. The interfacial shear strength is

commonly associated with this failure mode and is based on the assumption of shear along the fibre matrix interface.

King et al. have used an interphase to describe the interface failure between the fibre and matrix due to coating on the fibres, with various different coating materials [117]. Asp et al. have defined the interface failure between the fibre and matrix under transverse loads as being a function of the stress triaxiality in the matrix [18]. Bulsara et al. have discussed how the distribution of fibres in the cross section effects the transverse strength and fibre matrix debonding [41]. The initiation of debonding is dependent on the model used and the initiation criteria.

Zhandarov and Mäder have reviewed literature on laboratory tests of interfacial shear strength, which is typically done by embedding a length of fibre within the matrix and testing how much force is required to pull the fibre out of the matrix. They also conducted experiments testing the bond strength of glass and aramid fibres in cement and epoxy matrices and comparing their results to existing theories [185]. Nano indentation testing can also be used to determine the interfacial shear strength of a fibre matrix pairing as reviewed by Gibson, by applying a load to a punch in contact with only the fibre and compressing until the fibre begins to move relative to the matrix [74].

2.4.4 Fibre Microbuckling

Fibre microbuckling is a failure mode that occurs while the composite is under compressive loading. The buckling mechanism is similar to Euler buckling for a slender member. Due to the high aspect ratio of the fibre there is a tendency for lateral deflection while subjected to compressive loading with little lateral support from the matrix. The matrix supports the tendency for lateral buckling of the fibre to a point but above this point the fibres buckle in a fashion known as micro buckling or kink banding.

Budiansky described the micromechanics of microbuckling of carbon fibres and named the phenomena fibre kinking, and found that high angle failures were most common [39]. One of the main characteristics of failure under axial compression experimentally observed by Shikhmanter et al. is the failure mechanism through microbuckling of the fibres in the matrix [156]. Jelf and Fleck found that of the four failure modes, plastic microbuckling is the most prevalent for compressive loading [113]. Budiansky and Fleck have derived the equations to describe fibre microbuckling and have found that the phenomena is driven by plastic deformation of the matrix and has strong dependency on the degree of fibre misalignment [40]. Slaughter and Fleck have developed a viscoelastic model for the microbuckling of composites based on the plastic model developed by Budiansky and Fleck

[158, 40]. Slaughter and Fleck moved on to discuss the effects of fibre waviness and distribution on the microbuckling of a composite laminate and found the compressive strength of the composite to be very sensitive to the fibre waviness [159]. Sutcliffe and Fleck have experimentally observed and characterized the microbuckling of fibres [163]. Fleck and Shu implemented a fibre buckling initiation criterion in a 2-D finite element code for simulating the onset of failure through microbuckling [69].

Lui et al. have devised a failure model based on fibre microbuckling dependent on the 2-D distribution of fibre waviness using the research done previously by Fleck and co-authors [129]. Recently Bar-On and Wagner have proposed a model for fibre reinforced materials with platelets in the matrix to provide additional reinforcement, and studied the effects of the platelets on failure modes such as micro-buckling of the fibres [22]. Raimondo et al. have captured microbuckling by considering a shear and kinking based failure criterion [145]. The phenomenon for fibre microbuckling is well understood, however the implementation of failure criterion in unique to the model being used and should be considered while developing a new model framework.

2.4.5 Fibre Tensile Failure

Fibre failure is usually considered to be brittle failure when the maximum stress that the fibre can support is exceeded. Fibre failure predominately occurs when the composite is under tension, whereas microbuckling is the dominant failure mode that occurs under compression. It is common to assume that the fibres only support load along their axis, and transverse fibre failure is not considered.

Raimondo et al. have used a maximum stress failure criterion to describe the axial failure of the fibres [145]. At high loads Lambert et al. found fibre failure to be the main failure mechanism of composites under cyclic loading [121]. Kant and Penumandu have researched how fibres fail in tension under the presence of an existing surface flaw [114]. Most failure models incorporate a maximum tensile failure stress. This is considered in the development of the model framework in this thesis.

2.4.6 Matrix Microcracking

Matrix microcraking is a failure mode by which the matrix material fails in between the fibres. In this failure mode crack initiation occurs within the matrix material and the crack spreads within the matrix but not into the fibre. This failure mode is more likely to

occur in the direction perpendicular to the fibre under transverse and shear loading. For non-unidirectional composites this failure mode occurs more often in resin rich areas.

Microcracking development and propagation in the matrix has been discussed under combined and shear loadings by Fleck and Jelf [68]. Asp et al. have suggested that matrix microcracking between the fibres is due to the stress triaxiality experienced in the region surrounding the fibres [18]. Asp et al. went on to develop crack initiation criteria for glassy polymers dependent on the stress state using common metallic yield criterion such as Von Mise's and Tresca [19]. Asp et al. have also identified that the yield and subsequent crack formation in the matrix occurs at much lower stresses in composites than it does for the matrix on its own [20].

The matrix cracking between fibres subject to transverse loading has been studied by Bulsara et al. [41]. Lambert et al. have found matrix microcracking to be an important fatigue failure mechanism at low loads [121]. Matrix cracking was also found to be a precursor for delamination under cyclic loading [121]. The implementation of microcrack initiation is dependent on the model used and there is disagreement between researchers on the initiation criteria. All initiation criteria are considered during the model development.

2.4.7 Cohesive Elements for use in Failure Modelling

Cohesive elements can be used to simulate the interface between the reinforcing fibres and the matrix. Most of the work on this method has occurred within the past ten years due to computational advancements. Typically, the matrix and the fibre are meshed in finite element software using two distinct sets of material properties, the meshes of the fibre and matrix are attached to one another using cohesive elements. Cohesive elements are used for micromechanics modelling as well as modelling delamination at the ply level in laminated composites. Jalalvand et al. have demonstrated how cohesive elements can be used to capture damage due to delamination of laminated composites [111]. The use of cohesive elements in a full field model is very computationally expensive.

Kushch et al. used cohesive elements between the fibre and matrix to simulate the micro-scale debond and crack initiation along the interface between the fibre and matrix. They also observed through the use of the cohesive model that the stress is reduced in the neighbouring fibres of the debond, however the load has to be increased around other fibres leading to crack propagation of the debond [119]. O'Dwyer et al. have used cohesive elements to describe two failure modes at the micromechanics level when a composite is subjected to mode I and mode II loading, the bond between the fibre and matrix is simulated using cohesive elements. They also considered these loads on an adhesive bond

between the composite ply and an adjacent ply to see if there was debonding between the fibres and matrix first or debonding of the adhesive layer [134]. Yang et al. have implemented both interface debonding and matrix microcracking through the use of cohesive elements around fibres using a Drucker-Pranger model to account for the matrix microcracking [184]. Cohesive elements are promising in their use in modelling of debonding, however other modelling techniques are required to capture the other failure modes.

2.5 Fibre Orientation Effects in Compression Moulded Composites

Composite structures manufactured using compression moulding techniques such as SMC, BMC, and DLFT do not have aligned fibres and their strength and stiffness is dependent on the fibre orientation distribution within the composite. Feld et al. have described how anisotropy arises in SMC material due to flow and change in fibre orientation during processing [65]. For short fibre composites manufactured using injection moulding or similar compression moulding techniques, the fibre orientation plays a crucial role in the properties of the structure. In Section 2.3 homogenization techniques were discussed to homogenize fibre orientations into the overall response such as Lielens et al., Pierard et al., and Ogierman and Kokot [126, 139, 135].

Massardier-Nageotte et al. have discussed techniques for evaluating fibre orientation and fibre volume content in SMC materials including X-ray and optical techniques [130]. Le et al. have discussed using X-ray microtomography to analyse the fibre and void content in SMC materials [122]. Le et al. found that there is a variation in fibre volume fraction over the thickness of a SMC plate with lower volume fraction at the surfaces and higher volume fraction in the core of the material (roughly 1.8 times higher). They also found that the void content was higher in the core of the material. They have also shown that before forming the fibre orientation of the raw SMC is in the x_1, x_2 plane with preferential orientation in the x_1 manufacturing direction [122]. Garesci and Fliegener have used microtomography to evaluate the fibre orientations in a DLFT composite and have predicted the through thickness change in elastic properties using the Halpin Tsai relations [72]. Schladitz et al. evaluated the fibre orientation of SMC using both x-ray micro computed tomography and scanning acoustic microscopy to determine the effects of preferential orientation on the fatigue life of the material [154].

Advani and Tucker have developed a method to represent fibre orientation distributions as the probability that a fibre will be in a specific orientation given as $\Psi(\theta, \phi)$, where the

probability is represented as a function of Euler angles θ and ϕ or alternatively as the fibre unit vector $\hat{n}$ as $\Psi(\hat{n})$ [16]. The fibre orientation tensors are created by integrating the orientation distribution over the fibre directions to obtain either a second or fourth order tensor as

$$\mathbf{A} = \oint \hat{n}_i \hat{n}_j \Psi(\hat{n}) dn \tag{2.5}$$

$$\mathbb{A} = \oint \hat{n}_i \hat{n}_j \hat{n}_k \hat{n}_l \Psi(\hat{n}) dn \tag{2.6}$$

[16]. The fibre orientation distribution can also be recovered from the fibre orientation tensors where the fibre orientation distribution allows for the details of the angular distributions to be visualized, closure approximations are used to relate the second and fourth order orientation distribution functions [16].

Schjødt-Thomsen and Pyrz have discussed the non-symmetric stiffness tensors that arise using the Mori Tanaka approach when incorporating fibre orientations into the homogenization scheme. They proposed a method to create symmetric stiffness tensors which works for specific cases of inclusion shape and orientation [153].

Dray et al. have used a two-stage homogenization for short fibre composites. First the overall elasticity tensor for the unidirectionally aligned composite is calculated as

$$\mathbb{L}_{UD} = \mathbb{L}_m + V_f \left(\mathbb{L}_f - \mathbb{L}_m\right) : \mathbb{T}_{mt} \tag{2.7}$$

where $\mathbb{T}_{mt}$ is the Mori-Tanaka strain localization tensor given as

$$\mathbb{T}_{mt} = \mathbb{T} : [(1 - V_f)\mathbb{I} + V_f \mathbb{T}] \tag{2.8}$$

where $\mathbb{T}$ is the strain localization tensor presented in Eq. 2.4. The unidirectional stiffness tensor is then modified through the orientation tensor to calculate a new modified stiffness tensor as the second part of the homogenization [60].

A two-step homogenization has become a commonly used method for dealing with composites containing misaligned inclusions [57]. This method requires the fibre orientation distribution function to be discretized into a number of pseudo grains each with a unique orientation and associated fibre volume fraction. Commonly, the Mori Tanaka homogenization scheme is implemented as the first step of the homogenization, followed by assuming that the strain applied to each pseudo grain is the same (Voigt homogenization) as the second step.

Chapter 3

Elastic Functionally Graded Interphase Model

Currently, to capture the micromechanics response of composite materials it is common to create a full field finite element model with separate meshes for the fibre and the matrix material, which are joined using cohesive elements. This approach is computationally inefficient. The goal with the new framework is to capture the same fidelity with respect to the stresses and strains in each material while improving computational efficiency. In order to eliminate the need for cohesion between two separate material models, the homogenized response of both materials combined is required. The model needs to account for the interaction between the fibres and the matrix material within the constitutive framework.

This chapter covers the development of an elastic model depicting the micromechanics response of long fibre composites through the use of a functionally graded interphase (FGI) surrounding a single representative fibre. The model itself contains no physically distinct phases since it accounts for the presence of the fibre through homogenization of the response. The model was calibrated and validated using published experimental data by Hsiao and Daniel [104] and Kyriakides et al. [120].

3.1 Model Formulation

In this section, the formulation of the elastic FGI model is presented. After the completion and publication of this model it was found that a model developed by Sburlati and Cianci [152] uses similar principles to determine the effective modulus of a composite material

with spherical inclusions subjected to a hydrostatic pressure, however the model developed herein is for general three-dimensional load cases and cylindrical inclusions. It should also be noted that the work of Sburlati and Cianci was published after the model presented in this section had been submitted for publication [152, 150].

3.1.1 Model Assumptions

The matrix material is assumed to be an isotropic elastic material with a Young's modulus and Poisson's ratio. The fibres are assumed to be a transversely isotropic elastic material requiring the transverse axial shear modulus, two Young's moduli and two independent Poisson's ratios to describe the deformation. It is assumed that the fibres are stiffer than the matrix. The elastic material models relate stress to strain using the relationship

$$\begin{Bmatrix} \sigma_{11} \\ \sigma_{22} \\ \sigma_{33} \\ \sigma_{12} \\ \sigma_{23} \\ \sigma_{13} \end{Bmatrix} = \big[\mathbb{L}\big] \begin{Bmatrix} \varepsilon_{11} \\ \varepsilon_{22} \\ \varepsilon_{33} \\ \varepsilon_{12} \\ \varepsilon_{23} \\ \varepsilon_{13} \end{Bmatrix}. \tag{3.1}$$

Note that the definition of shear strain is the ε form which is half of the γ definition of shear strain and all the related tensors will be presented in this form for consistency.

For the isotropic matrix material, the elasticity tensor $\mathbb{L}$ is

$$\big[\mathbb{L}\big] = \frac{E_m}{(1+\nu_m)(1-2\nu_m)} \begin{bmatrix} 1-\nu_m & \nu_m & \nu_m & 0 & 0 & 0 \\ \nu_m & 1-\nu_m & \nu_m & 0 & 0 & 0 \\ \nu_m & \nu_m & 1-\nu_m & 0 & 0 & 0 \\ 0 & 0 & 0 & 1-2\nu_m & 0 & 0 \\ 0 & 0 & 0 & 0 & 1-2\nu_m & 0 \\ 0 & 0 & 0 & 0 & 0 & 1-2\nu_m \end{bmatrix} \tag{3.2}$$

where the matrix Young's modulus is E_m and the Poisson's ratio is ν_m. For the transversely isotropic fibre material the general response follows Eq. 3.1, but the elasticity tensor $\mathbb{L}$ has the form

$$\big[\mathbb{L}\big] = \begin{bmatrix} L_{11} & L_{12} & L_{12} & 0 & 0 & 0 \\ L_{12} & L_{22} & L_{23} & 0 & 0 & 0 \\ L_{12} & L_{23} & L_{22} & 0 & 0 & 0 \\ 0 & 0 & 0 & L_{44} & 0 & 0 \\ 0 & 0 & 0 & 0 & L_{66} & 0 \\ 0 & 0 & 0 & 0 & 0 & L_{44} \end{bmatrix}. \tag{3.3}$$

Where the six elastic terms are

$$L_{11} = \frac{E_{f_A}(1-\nu_{f_T})}{1-\nu_{f_T}-2\nu_{f_{TA}}^2\left(\frac{E_{f_T}}{E_{f_A}}\right)} \tag{3.4}$$

$$L_{12} = \frac{E_{f_T}\nu_{f_{TA}}}{1-\nu_{f_T}-2\nu_{f_{TA}}^2\left(\frac{E_{f_T}}{E_{f_A}}\right)} \tag{3.5}$$

$$L_{22} = \frac{E_{f_T}\left(1-\nu_{f_{TA}}^2\left(\frac{E_{f_T}}{E_{f_A}}\right)\right)}{\left(1-\nu_{f_T}-2\nu_{f_{TA}}^2\left(\frac{E_{f_T}}{E_{f_A}}\right)\right)(1+\nu_{f_T})} \tag{3.6}$$

$$L_{23} = \frac{E_{f_T}\left(\nu_{f_T}+\nu_{f_{TA}}^2\left(\frac{E_{f_T}}{E_{f_A}}\right)\right)}{\left(1-\nu_{f_T}-2\nu_{f_{TA}}^2\left(\frac{E_{f_T}}{E_{f_A}}\right)\right)(1+\nu_{f_T})} \tag{3.7}$$

$$L_{44} = 2G_{f_{TA}} \tag{3.8}$$

$$L_{66} = \frac{E_{f_T}}{1+\nu_{f_T}} \tag{3.9}$$

the elastic constants are the fibre axial modulus E_{f_A}, the fibre transverse modulus E_{f_T}, the transverse axial fibre shear modulus $G_{f_{TA}}$, the fibre transverse Poisson's ratio ν_{f_T} and the fibre transverse axial Poisson's ratio $\nu_{f_{TA}}$. It should be noted that the fibre axial transverse Poisson's ratio is related to the fibre transverse axial Poisson's ratio as

$$\nu_{f_{AT}} = \left(\frac{E_{f_T}}{E_{f_A}}\right)\nu_{f_{TA}} \tag{3.10}$$

and has been omitted from the terms of the elastic matrix for the transversely isotropic elastic fibre for simplicity.

The transversely isotropic elasticity tensor for the fibre is referred to as $\mathbb{L}_f$ from here forward and the isotropic elasticity tensor for the matrix material is referred to as $\mathbb{L}_m$.

It is assumed that the strain in the fibre and the matrix is the same as the strain applied to the material. This is the Voigt assumption which forms the upper bounds on the homogenized response of composite materials. It is known to work well when the material is loaded along the fibre direction, but over predicts for the transverse response. This assumption is incorrect as it is well documented that the strain in the fibre and matrix are not the same, however it served as a starting point for model development.

It is assumed that the fibres are round in cross section and have a constant cross sectional area along their length. It is also assumed that there is a constant fibre volume

fraction within the region of interest. The fibre volume fraction is equivalent to the fibre area fraction by making these assumptions. It is also assumed that the fibres all have the same diameter. The area of a fibre (A_f) is related to the fibre radius (r_f) as

$$A_f = \pi r_f^2. \tag{3.11}$$

The number of fibres within a unit area can therefore be determined as

$$n = \frac{A_f}{V_f} \tag{3.12}$$

It is assumed that the fibres have a square packing and are evenly spaced, which limits the maximum volume fraction to 0.77.

3.1.2 Unit Cell Definition

In order to homogenize the model more effectively, the mechanism of load transfer has to be considered. Traditional composite modelling is based on the use of the surface area of the fibres being used to transfer the load as an interface. The amount of load which is transferred across the interface depends on the interface quantity and properties. Shear is the method for the force transfer across the boundary and this leads to large stress concentrations in the vicinity of the fibre for the Voigt assumption which is being used. It is crucial for a model to correctly capture the stress transition in order to predict the breakdown or failure of the interface. Considering a region within a composite material with one unit of volume, the quantity of interface is

$$A_{intf} = 2\sqrt{\pi n V_f} \tag{3.13}$$

where A_{intf} is the area of interface within the volume being considered. The quantity of interface is dependent on the number of fibres within the region of interest and also the fibre diameter.

An interphase is another method that can be used to represent the load transfer between the fibre and matrix. An interphase is a third material phase which has different material properties from both the fibre and the matrix. The interphase approach is used in the double inclusion problem where it is assumed that the inclusion is surrounded by a second inclusion of the same shape. If the interphase size is assumed to be proportional to the fibre radius with some proportionality constant p, then the volume of interphase material within a region of interest is

$$V_{intp} = \frac{(p-1)V_f}{\pi}. \tag{3.14}$$

Assuming that the interphase size is proportional to the fibre radius allows the total quantity of interphase to be independent of the number of fibres. Therefore, one fibre surrounded by an interphase can represent any number of aligned fibres. An interphase based approach is used in the proposed model framework.

A unit cell is defined using a natural system of coordinates where the domain of each axis is $-1 \leq x_1 \leq 1$, $-1 \leq x_2 \leq 1$, and $-1 \leq x_3 \leq 1$. A single representative fibre is aligned with the x_1 axis of the unit cell as illustrated in Figure 3.1. The representative

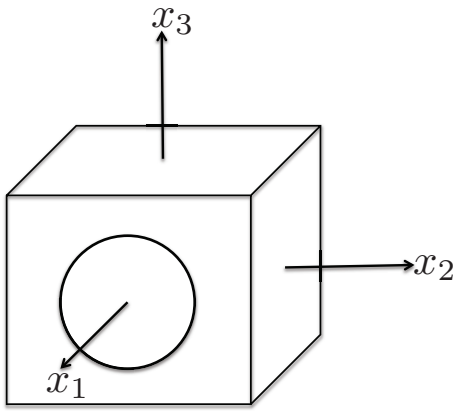

Figure 3.1: Unit cell configuration with a representative fibre along the x_1 axis [149]

fibre radius (r_{rf}) for the unit cell is defined as

$$r_{rf} = \sqrt{\frac{4V_f}{\pi}}. \tag{3.15}$$

It is assumed that the interphase starts within the representative fibre and extends beyond the representative fibre into the matrix material. Two proportionality constants k and l are defined to describe the boundaries of the interphase zone. The interphase start radius (r_{is}) occurs within the boundary of the representative fibre and is given by

$$r_{is} = kr_{rf} \tag{3.16}$$

where the range of k is $0 \leq k \leq 1$. The outer boundary of the interphase is the interphase finish radius (r_{if}) which is given by

$$r_{if} = lr_{rf} \tag{3.17}$$

where $l \geq 1$. It was decided later that an upper limit on l can be assigned such that the interphase zone ends at the edge of the unit cell and does not go into neighbouring unit

cells. This limit is

$$l \leq \sqrt{\frac{\pi}{4V_f}}, \tag{3.18}$$

which is similar to Eq. 3.15 and comes from setting the representative fibre radius to 1. The bounds on the interphase zone on the x_2, x_3 plane is shown in Figure 3.2. We have

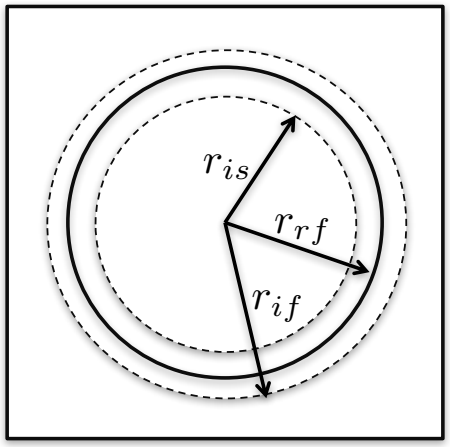

Figure 3.2: Interphase zone limits on the x_2, x_3 plane

defined our unit cell containing a single representative fibre surrounded by an interphase zone based only on the fibre volume fraction and two interphase parameters k and l.

3.1.3 Functionally Graded Interphase

The material properties within the interphase are unknown, they will be different from the fibre and matrix but are undefined for a two-phase composite material. The material properties of the fibre and matrix are obtained from experiments, however the interphase properties will influence the response of the overall composite material.

As the Voigt assumptions forms the upper bounds on the elastic modulus for composite materials, the interphase is used as a method to reduce the stiffness by reducing the amount of material which is as stiff as the fibres. This is accomplished by transitioning the elastic properties in the interphase zone from those of the representative fibre to the matrix properties as a function of position around the representative fibre. This creates a FGI. Since only the properties of the representative fibre and the matrix are known, the interphase is used to define an abrupt transition between the two materials.

Given that the elastic material properties are assumed to change as a function of radial position within the interphase zone, the elastic moduli are used to initially define the interphase functions. Since the fibres are transversely isotropic the generic fibre modulus E_f is used to define the interphase functions and can represent either the axial or transverse fibre modulus depending on the loading direction. The end points of the interphase function in cylindrical coordinates about the representative fibre are (r_{is}, E_f) and (r_{if}, E_m) as the inner and outer endpoint respectively. The interphase functions are defined using control points. The simplest case uses the two end points as values of the function. Control points can also be the derivative of the function evaluated at a specific point.

Compatibility between the phases is enforced due to the Voigt assumption where the strain in each phase is equivalent. Although the stress equilibrium between the phases is violated, there is a transition in stress along the FGI so that locally the violation of equilibrium is small even though there is a discontinuity between the stress in the fibre and that of the matrix material.

The interphase functions are integrated to create a representative interface radius (r_{ri}) where there is a sharp transition between the fibre and matrix properties. The representative interface radius is used to modify the fibre volume fraction in a rule of mixtures approach to predict the response of the two-phase composite. The process for calculating the representative interface radius is to integrate the interphase function in cylindrical coordinates about the representative fibre then equate the volume to that of a tube with the inner radius of r_{is} and an outer radius of r_{ri} known as the volume of difference in moduli ($v_{\Delta E}$). The volume of this tube is given as

$$v_{\Delta E} = \pi \left(E_f - E_m\right) \left(r_{ri}^2 - r_{is}^2\right), \tag{3.19}$$

which can be rearranged to calculate the representative interface radius as

$$r_{ri} = \sqrt{\frac{v_{\Delta E}}{E_f - E_m} + r_{is}^2}. \tag{3.20}$$

Linear Interphase Function

A linear function is defined using the two end points of the interphase zone (r_{is}, E_f) and (r_{if}, E_m) as control points where the value of the function is known. The modulus within the interphase zone is described as a function of the radius as

$$E(r) = -\left(\frac{E_f - E_m}{r_{if} - r_{is}}\right) r + \frac{E_f r_{if} - E_m r_{is}}{r_{if} - r_{is}}. \tag{3.21}$$

The volume of difference in moduli is calculated by integrating the interphase function around the representative fibre as

$$v_{\Delta E} = \int_0^{2\pi} \int_{r_{is}}^{r_{if}} \int_{E_m}^{-\left(\frac{E_f - E_m}{r_{if} - r_{is}}\right) r + \frac{E_f r_{if} - E_m r_{is}}{r_{if} - r_{is}}} r dE dr d\theta \tag{3.22}$$

where θ is a rotation about the x_1 axis of the unit cell. Evaluating the integral the resulting volume of difference in moduli is

$$v_{\Delta E} = \frac{\pi}{3} \left(r_{if} - r_{is}\right) \left(r_{if} + 2r_{is}\right) \left(E_f - E_m\right). \tag{3.23}$$

Equating this volume of the difference of moduli to the case of the tube given in Eq. 3.19 and rearranging to find the representative interface radius given in Eq. 3.20. The resultant representative interface radius for the linear interface function is

$$r_{ri} = \sqrt{\frac{1}{3}\left(r_{if}^2 + r_{if} r_{is} + r_{is}^2\right)}. \tag{3.24}$$

For comparison of the interphase functions and interface radii the two end points of the interphase functions were set to $(r_{is}, E_f) = (0.5, 213.7 \text{ GPa})$, and $(r_{if}, E_m) = (0.8, 3.45 \text{ GPa})$. Using these end points the interphase function and representative interface radius are plotted in Figure 3.3. It is noted that the use of a linear interphase function leads to an abrupt transition in the slope of the elastic moduli at the end points of the interphase zone. This transition between the linear function and the constant values beyond the end points cause the derivative at the end points to not be definable.

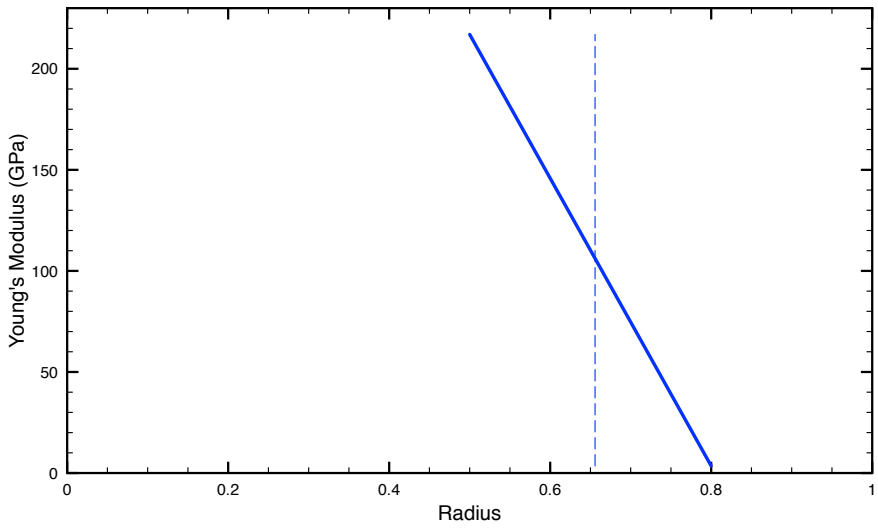

Figure 3.3: Elastic modulus as a function of position in cylindrical coordinates about the x_1 axis using the linear interphase function and the associated linear representative interface radius [150]

Quadratic Interphase Functions

For quadratic interphase functions, the two end points are used as control points where the value of the interphase function is known, using a similar approach to that used for the linear interphase function. Two distinct interphase functions are defined by setting the value of the derivative of the end points of the interphase function to zero. The first quadratic interphase function uses the derivative set to zero at (r_{is}, E_f) resulting in the radius being defined as a function of modulus as

$$r(E) = \frac{r_{if} - r_{is}}{(E_m - E_f)^2} (E - E_f)^2 + r_{is}. \tag{3.25}$$

The order of integration for the interphase function changes from modulus, radius, and then around the x_1 axis used for the linear interphase function to radius, modulus and then about the x_1 axis. The volume of differences of stress is calculated by integrating the equation

$$v_{\Delta E} = \int_0^{2\pi} \int_{E_m}^{E_f} \int_{r_{is}}^{\frac{r_{if}-r_{is}}{(E_m-E_f)^2}(E-E_f)^2+r_{is}} r dr dE d\theta, \tag{3.26}$$

which results in a volume of difference of moduli of

$$v_{\Delta E} = \frac{\pi}{15}\left(r_{if} - r_{is}\right)\left(3r_{if} + 7r_{is}\right)\left(E_f - E_m\right). \tag{3.27}$$

The representative interface radius for the case of the first quadratic interphase function is calculated in the same fashion as that for the linear interphase function given in Eq. 3.24, which is determined to be

$$r_{ri} = \sqrt{\frac{1}{5}r_{if}^2 + \frac{4}{15}r_{if}r_{is} + \frac{8}{15}r_{is}^2}. \tag{3.28}$$

The first quadratic interphase function and associated representative interface radius are shown in Figure 3.4

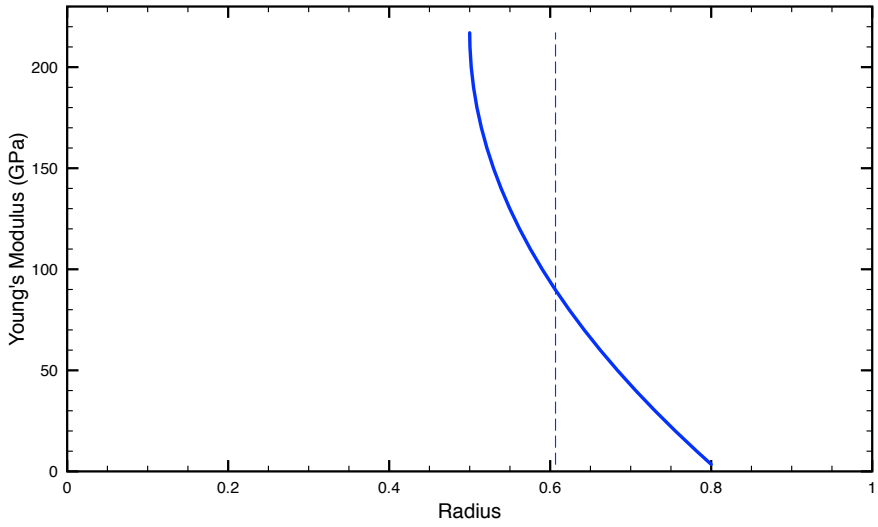

Figure 3.4: Elastic modulus as a function of position in cylindrical coordinates about the x_1 axis using the quadratic 1 interphase function and the associated quadratic 1 representative interface radius [150]

The second quadratic interphase function has the derivative of the function set to zero at (r_{if}, E_m), which results in there being a continuous derivative of the modulus across this point. For this interphase function the modulus is defined as a function of the radius as

$$E(r) = \frac{E_f - E_m}{\left(r_{if} - r_{is}\right)^2}\left(r - r_{if}\right)^2 + E_m. \tag{3.29}$$

The integration order for the second quadratic interphase function is the same as for the linear interphase function given in Eq. 3.22. The equation to calculate the volume in difference of modulus is

$$v_{\Delta E} = \int_0^{2\pi} \int_{r_{is}}^{r_{if}} \int_{E_m}^{\frac{E_f - E_m}{\left(r_{if} - r_{is}\right)^2}\left(r - r_{if}\right)^2 + E_m} r dE dr d\theta. \tag{3.30}$$

The resulting volume of difference of Young's modulus through integration is

$$v_{\Delta E} = \frac{\pi}{6}\left(r_{if} - r_{is}\right)\left(r_{if} + 3r_{is}\right)\left(E_f - E_m\right). \tag{3.31}$$

This volume is again equated to that of a tube to calculate the representative interface radius, which for the second quadratic interphase function is

$$r_{ri} = \sqrt{\frac{1}{6}r_{if}^2 + \frac{1}{3}r_{if}r_{is} + \frac{1}{2}r_{is}^2}. \tag{3.32}$$

The second quadratic interphase function and associated representative interface radius are shown in Figure 3.5

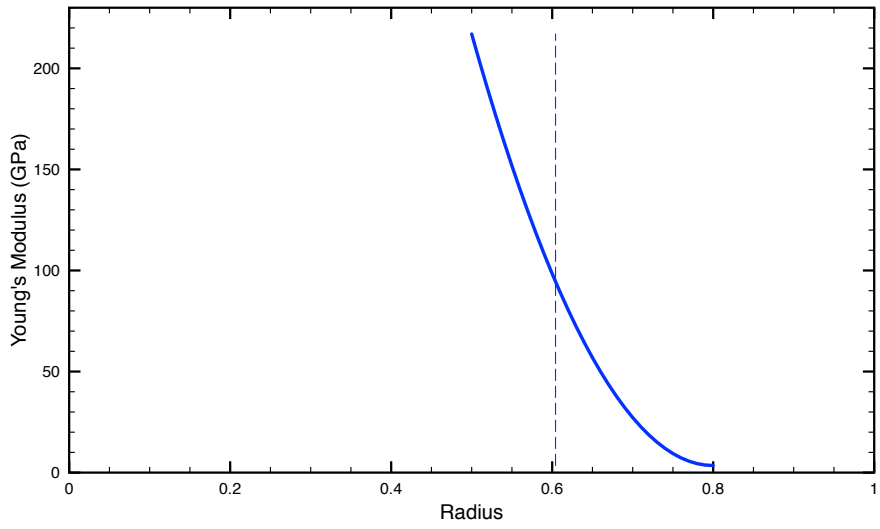

Figure 3.5: Elastic modulus as a function of position in cylindrical coordinates about the x_1 axis using the quadratic 2 interphase function and the associated quadratic 2 representative interface radius [150]

Exponential Interphase Function

An exponential function is used to describe the Young's modulus as a function of position anywhere within the domain of the unit cell as the function is continuous over the domain. The derivatives of the function can also be evaluated at any point within the unit cell and not just over the domain of the interphase zone. Two additional material paring parameters m and q are used to further define the functionality of the exponential interphase function and they are used to change the curvature depending on the material pairing used. The exponential interphase function defines the modulus as a function of the position as

$$E(r) = E_f - \frac{E_f - E_m}{1 + e^{\left(\frac{-20m}{r_{if}-r_{is}} + 10q + \frac{20mr_{is}}{r_{if}-r_{is}}\right)}}. \tag{3.33}$$

As the function is continuous within the unit cell the limits of integration on the radius are changed to start at a radius of zero and extend to the interphase finish radius r_{if}. Thus, the volume calculated is compared to a cylinder instead of a tube to evaluate the representative interface radius. The volume of difference in Young's modulus is

$$v_{\Delta E} = \int_0^{2\pi} \int_o^{r_{if}} \int_{E_m}^{E_f - \frac{E_f - E_m}{1+e^{\left(\frac{-20m}{r_{if}-r_{is}} + 10q + \frac{20mr_{is}}{r_{if}-r_{is}}\right)}}} r dE dr d\theta \tag{3.34}$$

Evaluating the integral the volume in difference of Young's modulus is

$$v_{\Delta E} = B \begin{bmatrix} 20 \ln\left(1 + e^C\right) r_{if} m + {}_3F_2\left(1,1,1;2,2;-e^C\right) r_{if} e^C \\ - {}_3F_2\left(1,1,1;2,2;-e^C\right) r_{is} e^C - {}_3F_2\left(1,1,1;2,2;-e^D\right) r_{if} e^D \\ + {}_3F_2\left(1,1,1;2,2;-e^D\right) r_{is} e^D \end{bmatrix} \tag{3.35}$$

where

$$B = -\frac{\pi\left(r_{if} - r_{is}\right)\left(E_f - E_m\right)}{200m^2}, \tag{3.36}$$

$$C = -20m + 10q, \tag{3.37}$$

$$D = \frac{10\left(2mr_{is} + qr_{if} - qr_{is}\right)}{r_{if} - r_{is}}. \tag{3.38}$$

The ${}_3F_2\left(1,1,1;2,2;-e^B\right)$ functions are hypergeometric functions given in Pochhammer's notation [61]. The volume is compared to that of a cylinder with the outer radius of r_{ri} as

$$v_{\Delta E} = \pi\left(E_f - E_m\right) r_{ri}^2. \tag{3.39}$$

Eq. 3.35 is equated to Eq. 3.39 resulting in a representative interface radius of

$$r_{ri} = \frac{1}{20m} \begin{bmatrix} -40\ln\left(1+e^{C}\right) m r_{if}^{2} + 40\ln\left(1+e^{C}\right) m r_{if} r_{is} \\ -{}_3F_2\left(1,1,1;2,2;-e^{C}\right) 2r_{if}^{2}e^{C} + {}_3F_2\left(1,1,1;2,2;-e^{C}\right) 4r_{is}r_{if}e^{C} \\ -{}_3F_2\left(1,1,1;2,2;-e^{C}\right) 2r_{is}^{2}e^{C} + {}_3F_2\left(1,1,1;2,2;-e^{D}\right) 2r_{if}^{2}e^{D} \\ -{}_3F_2\left(1,1,1;2,2;-e^{D}\right) 4r_{if}r_{is}e^{D} + {}_3F_2\left(1,1,1;2,2;-e^{D}\right) 2r_{is}^{2}e^{D} \end{bmatrix}^{\frac{1}{2}} . \quad (3.40)$$

The solution to the representative interface radius for the exponential interphase function is a sum of six infinite series and has dependence on the m and q values used to define the function. Therefore, although the exponential interphase function has favorable mathematic properties it is not practical for an engineering application where the computational efficiency of the process is important. The representative interface radius has not been evaluated due to these reasons. A plot of the exponential interphase function is given in Figure 3.6 where the values of m and q are set to unity.

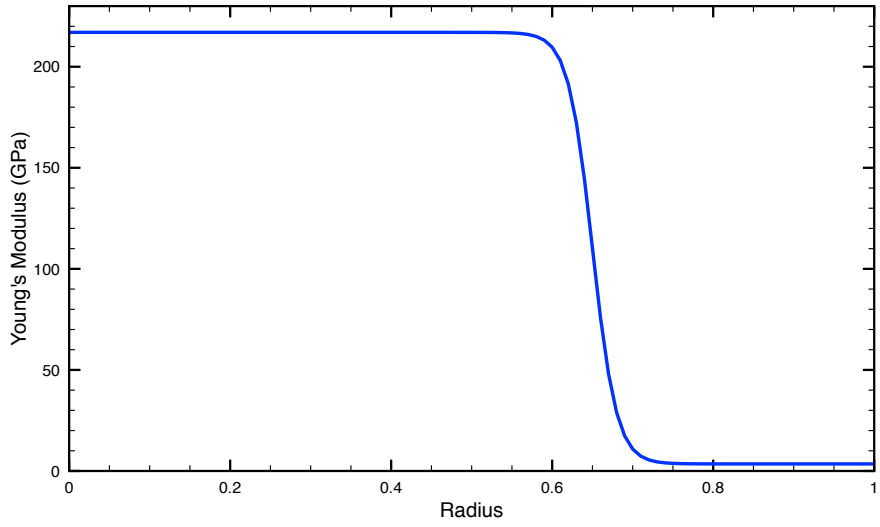

Figure 3.6: Elastic modulus as a function of position in cylindrical coordinates about the x_1 axis using the exponential interphase function [150]

Comparison of Interphase Functions

Four functions have been derived to describe the transition in Young's modulus in the region known as the interphase zone, which surrounds and includes a portion of the representative

fibre. The interphase zone occupies the volume in cylindrical coordinates about the x_1 axis of the unit cell in between the interphase start and interphase finish radii, r_{is} and r_{if} respectively. A plot comparing the four functions is shown in Figure 3.7, which uses the same values previously stated.

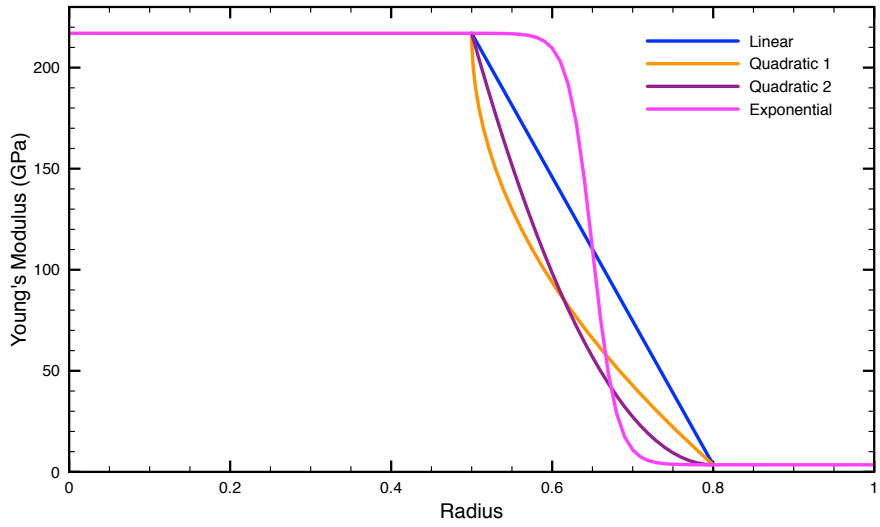

Figure 3.7: Elastic modulus as a function of position in cylindrical coordinates about the x_1 axis a comparison of the proposed interphase functions [150]

3.1.4 Stress Calculation

The average stress is used to compare the results of the proposed model to experimental results. The stress in the fibre and that of the matrix are combined volumetrically by defining a representative fibre volume fraction from the representative interface radius calculated using the interphase function. The representative fibre volume fraction is

$$V_{rf} = \frac{\pi}{4} r_{ri}^2. \tag{3.41}$$

The average stress is calculated by the rule of mixtures modified by the representative fibre volume fraction as

$$\sigma = V_{rf}\sigma_f + (1 - V_{rf})\,\sigma_m, \tag{3.42}$$

where σ_f is the stress calculated for the representative fibre and σ_m is the stress calculated for the matrix material. As both materials are elastic and since the Voigt assumption is used, the strain in both materials is equivalent. Therefore, the rule of mixtures applies to the constitutive laws and the average stress is calculated as

$$\sigma = \mathbb{L}\varepsilon \tag{3.43}$$

where the overall elasticity tensor $\mathbb{L}$ is a combination of that of the fibre and matrix as

$$\mathbb{L} = V_{rf}\mathbb{L}_f + (1 - V_{rf})\,\mathbb{L}_m. \tag{3.44}$$

The combination of an isotropic elastic material model with a transversely isotropic material model results in a transversely isotropic material with the generalized elasticity tensor of

$$\mathbb{L} = \begin{bmatrix} L_{11} & L_{12} & L_{12} & 0 & 0 & 0 \\ L_{12} & L_{22} & L_{23} & 0 & 0 & 0 \\ L_{12} & L_{23} & L_{22} & 0 & 0 & 0 \\ 0 & 0 & 0 & L_{44} & 0 & 0 \\ 0 & 0 & 0 & 0 & L_{66} & 0 \\ 0 & 0 & 0 & 0 & 0 & L_{44} \end{bmatrix} \tag{3.45}$$

where the six elastic constants are

$$L_{11} = (1 - V_{rf}) \left[\frac{E_m(1-\nu_m)}{1-\nu_m-2\nu_m^2} \right] + V_{rf} \left[\frac{E_{f_A}(1-\nu_{f_T})}{1-\nu_{f_T}-2\nu_{f_{TA}}^2 \left(\frac{E_{f_T}}{E_{f_A}}\right)} \right], \tag{3.46}$$

$$L_{12} = (1 - V_{rf}) \left[\frac{E_m\nu_m}{1-\nu_m-2\nu_m^2} \right] + V_{rf} \left[\frac{E_{f_T}\nu_{f_{TA}}}{1-\nu_{f_T}-2\nu_{f_{TA}}^2 \left(\frac{E_{f_T}}{E_{f_A}}\right)} \right], \tag{3.47}$$

$$L_{22} = (1 - V_{rf}) \left[\frac{E_m(1-\nu_m)}{1-\nu_m-2\nu_m^2} \right] + V_{rf} \left[\frac{E_{f_T}\left(1-\nu_{f_{TA}}^2 \left(\frac{E_{f_T}}{E_{f_A}}\right)\right)}{\left(1-\nu_{f_T}-2\nu_{f_{TA}}^2 \left(\frac{E_{f_T}}{E_{f_A}}\right)\right)(1+\nu_{f_T})} \right], \tag{3.48}$$

$$L_{23} = (1 - V_{rf}) \left[\frac{E_m\nu_m}{1-\nu_m-2\nu_m^2} \right] + V_{rf} \left[\frac{E_{f_T}\left(\nu_{f_T}+\nu_{f_{TA}}^2 \left(\frac{E_{f_T}}{E_{f_A}}\right)\right)}{\left(1-\nu_{f_T}-2\nu_{f_{TA}}^2 \left(\frac{E_{f_T}}{E_{f_A}}\right)\right)(1+\nu_{f_T})} \right], \tag{3.49}$$

$$L_{44} = (1 - V_{rf}) \left[\frac{E_m}{2(1+\nu_m)} \right] + V_{rf} 2G_{f_{TA}}, \tag{3.50}$$

$$L_{66} = (1 - V_{rf}) \left[\frac{E_m}{2(1+\nu_m)} \right] + V_{rf} \left[\frac{E_{f_T}}{1+\nu_{f_T}} \right]. \tag{3.51}$$

Seven elastic material constants are required to model the overall elastic response of a unidirectional composite material using the functionally graded interphase approach.

The stress in the fibre and stress in the matrix are calculated using their individual constitutive law, the fibre stress is

$$\sigma_f = \mathbb{L}_f \varepsilon \tag{3.52}$$

and for the matrix

$$\sigma_m = \mathbb{L}_m \varepsilon. \tag{3.53}$$

The stresses in the fibre and the matrix are stored to allow for the implementation of stress based failure criteria for the materials.

3.1.5 Model Implementation

The proposed model and Aboudi's method of cells [10] were implemented into user defined material models in the commercial finite element code LS-DYNA. The explicit dynamic version of LS-DYNA was used for the implementation of the User MATerial models (UMAT). LS-DYNA provides the user with the current deformation gradient $\mathbf{F}$, the strain increment $\Delta\varepsilon$, and time step Δt. The UMAT calculates the stress update to be returned to LS-DYNA. The stresses in each phase are stored as history variables to be used in subsequent time steps.

3.2 Results

Three studies were conducted to evaluate the proposed model, the existing modelling framework of Aboudi using the generalized method of cells [10], and experimental data. The first study compares the proposed model to that of Aboudi over a range of fibre volume fractions. The second study compares the model to the stress strain response of a carbon fibre epoxy system studied by Hsiao and Daniel [104]. The third study compares the proposed model to the stress strain response of a carbon fibre peek system studied by Kyriakides et al. [120]. For all studies a single 8 noded hexahedral element was used.

3.2.1 Comparison Over a Range of Fibre Volume Fractions

For this study, a factitious carbon fibre epoxy system were considered with material properties taken from Chamis 1986 [44]. The material properties are given in Table 3.1.

Table 3.1: Material properties taken from Chamis 1986 [44] used to compare the proposed model to Aboudi's model

Carbon Fibre	
E_{f_A} (GPa)	213.7
E_{f_T} (GPa)	13.8
$G_{f_{TA}}$ (GPa)	13.8
ν_{f_T}	0.2
$\nu_{f_{TA}}$	0.25
Epoxy	
E_m (GPa)	3.45
ν_m	0.35

Table 3.2: Interphase parameters calibrated to Aboudi's model

Interphase Function	k	l
Linear	0.89	1
Quadratic	0.92	1

The fibre volume fraction is varied between 0.25 and the upper limit of the unit cell model of 0.77. Both linear and quadratic interphase functions were considered, although as the model is calibrated to find an appropriate representative interface radius value, the functionality of the model does not affect the accuracy. All that would change when going between the linear and quadratic interphase function would be the values of the interphase parameters k and l to produce the same value of r_{ri}. The model was calibrated to match Aboudi's model for uniaxial deformation along the fibre direction, the interphase parameters are given in Table 3.2. It is noted that the difference between using the quadratic 1 and quadratic 2 interphase function is not distinguishable by varying the interphase parameters in increments of 0.01, therefore it is reported as just the quadratic interphase function.

One end of the single element had all four nodes fixed in place while the opposite end allowed for motion along the x_1 direction which is aligned with the fibre. The four corner nodes on the face which moves in the x_1 direction are constrained from motion in the x_2 and x_3 directions. Thus, the boundary conditions induce a stress in all three directions with an applied displacement only in one direction. The stress induced by the displacement is compared between the two models. The normal stress induced in the x_1 direction is compared in Figure 3.8. The stress induced in the x_1 direction by the proposed model predicts a stress within 2% of that predicted by Aboudi's model. The overall trends of the

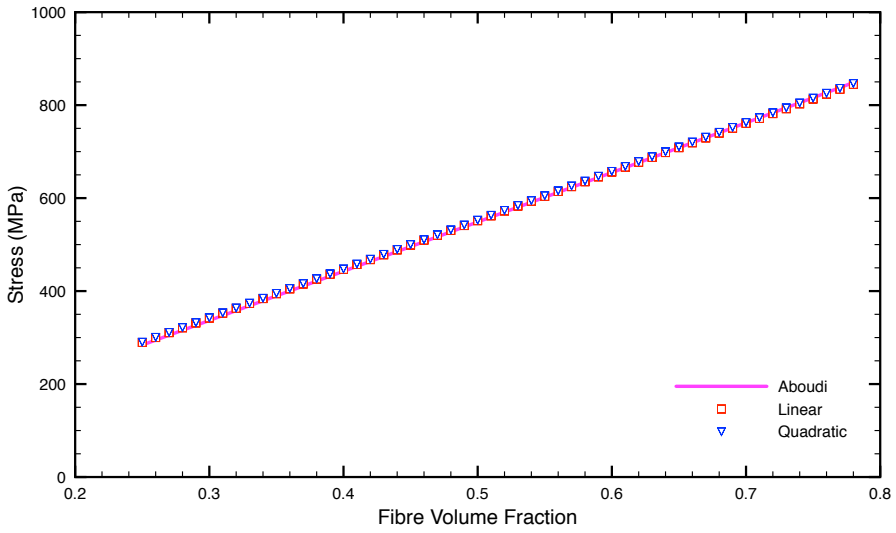

Figure 3.8: Stress induced normal to the x_1 direction by the applied displacement over a range of fibre volume fractions [150]

two models are the same, however the slope of the proposed model is slightly lower than that of Aboudi's model over the range of fibre volume fractions.

As stress was induced in all directions due to the boundary conditions applied to the finite element, the Von Mises stress predicted by the models is compared in Figure 3.9. The Von Mises stress is within 1% of each other over the range, with the proposed model slightly under predicting Aboudi's model for low volume fractions. The calibration of the model was conducted at a volume fraction of 0.6, as such the results will differ at the ends of the range of fibre volume fractions considered.

The results of the normal stress in the transverse direction to the fibre was also evaluated. This stress is normal to the x_2 and x_3 directions of the unit cell and the magnitude is equivalent due to the applied displacement. A comparison of the transverse normal stress induced by the applied displacement is shown in Figure 3.10 There is a large difference between the predicted response of the two models. The proposed model is linearly related to the fibre volume fraction, however, Aboudi's model has an inverse relation to the fibre volume fraction. In Aboudi's model the two elasticity constants that influence the

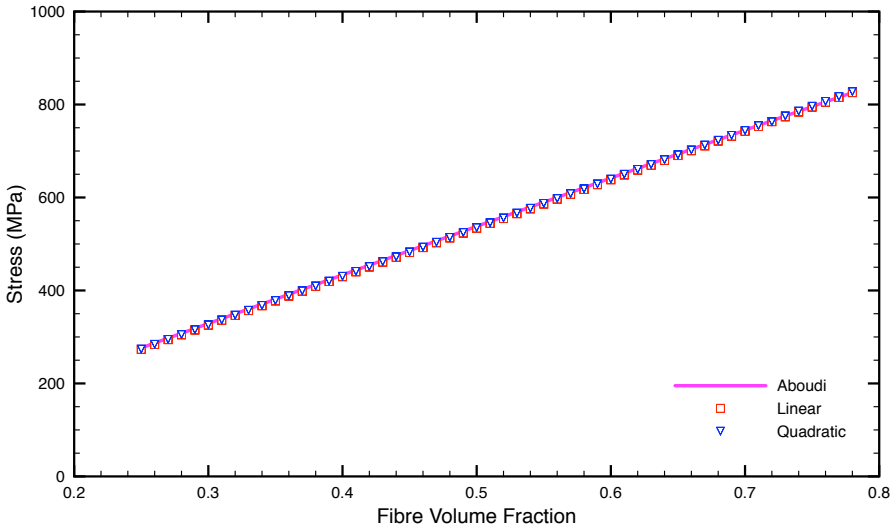

Figure 3.9: Von Mises stress induced by the applied displacement over a range of fibre volume fractions [150]

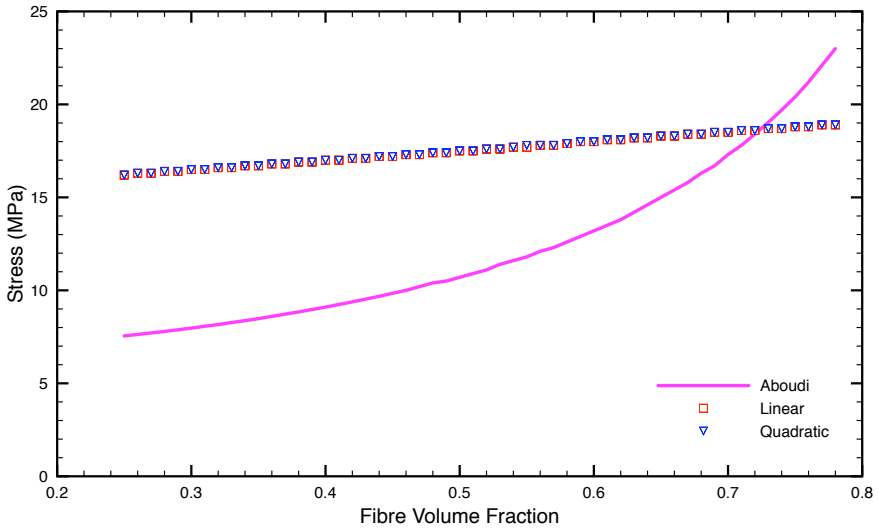

Figure 3.10: Transverse stress induced by the applied displacement over a range of fibre volume fractions [150]

transverse stress strain response are

$$\begin{aligned} L_{12} =& \frac{E_f E_m}{V_f E_m + V_m E_f} \left[\frac{V_f \nu_f E_f (1+\nu_m)(1-2\nu_m) + V_m \nu_m E_m (1+\nu_f)(1-2\nu_f)}{V_f E_f (1+\nu_m)(1-2\nu_m) + V_m E_m (1+\nu_f)(1-2\nu_f)} \right] \\ & \left[1 - \frac{V_m E_f + V_f E_m}{V_f \nu_f E_m + V_m \nu_m E_f} \right] - \frac{V_f E_f + V_m E_m}{2} \\ & \left[\frac{V_f E_f (1+\nu_m)(1-2\nu_m) + V_m E_m (1+\nu_f)(1-2\nu_f)}{V_f \nu_f E_f (1+\nu_m)(1-2\nu_m) + V_m \nu_m E_m (1+\nu_f)(1-2\nu_f)} \right], \end{aligned} \tag{3.54}$$

and

$$\begin{aligned} L_{22} =& - \frac{E_f E_m}{2(V_f \nu_f E_m + V_m \nu_m E_f)} - \frac{E_f E_m (V_m E_f + V_f E_m)}{2(V_f \nu_f E_m + V_m \nu_m E_f)} \\ & - \frac{(V_f E_f + V_m E_m)\left[V_f E_f (1+\nu_m)(1-2\nu_m) + V_m E_m (1+\nu_f)(1-2\nu_f)\right]^2}{4\left[V_f \nu_f E_f (1+\nu_m)(1-2\nu_m) + V_m \nu_m E_m (1+\nu_f)(1-2\nu_f)\right]^2}. \end{aligned} \tag{3.55}$$

The first term in both of the elastic tensor terms for Aboudi's model have inverse dependence of the fibre volume fraction resulting in the curvature shown. The intersection point for the two models is at 0.72 volume fraction. The proposed model over-predicts Aboudi's model by 115% at 0.25 volume fraction and under-predicts by 18 % at 0.78 volume fraction. The trends of Aboudi's model are those established for the lower bound on elasticity such as the Reuss assumption where the stress in both phases is assumed to be the same or other estimates such as the Hashin Shtrikman lower bound [93]. One key difference between the models is that Aboudi assumes there is an isotropic fibre whereas in the current implementation the assumption of transverse isotropy in the fibres is used to reduce the transverse stiffness. Aboudi's model requires this inverse dependence to reduce the transverse stiffness due to the assumption of isotropic fibres.

3.2.2 Comparison with Data from Hsiao and Daniel, 1996

The proposed elastic model is calibrated to the stress strain curves provided by Hsiao and Daniel for a unidirectional carbon fibre epoxy system [104]. The system consisted of IM6G fibres with a 3501-6 epoxy prepreg with 0.6 volume fraction, which is an aerospace grade material. The calibration parameters for this model are given in Table 3.3, a quadratic interphase function was chosen as it increases the k value to seem more physically likely compared to the linear interphase function. Stress strain data was given for axial compression, transverse compression, and shear by Hsiao and Daniel [104]. The Stress strain

Table 3.3: Model parameters for IM6G/3501-6 composite to match the experimental data of Hsiao and Daniel

IM6G Fibre	
E_{f_A} (GPa)	279
E_{f_T} (GPa)	13.8
$G_{f_{TA}}$ (GPa)	13.8
ν_{f_T}	0.3
$\nu_{f_{TA}}$	0.3
3501-6 Epoxy	
E_m (GPa)	3.45
ν_m	0.35
Interphase	
k	0.7
l	1

response were compared up to 1% strain where there was clear separation between the elastic models and the experimental results.

For axial compression, the stress strain results of the models compared to the experiment are shown in Figure 3.11. The proposed model provides a very accurate prediction of the experimental stress strain response up to 0.8% strain where the experimental data curves downwards. The stress predicted by Aboudi's model is 18.4% higher than the calibrated proposed model for all strains as they are both linear elastic models. At 1% strain the proposed model predicts a stress 7.6% higher than the experiment and the stress predicted by Aboudi's model is 27% higher than the experiment.

The comparison of the stress strain results for transverse compression between the two models and experiment are shown in Figure 3.12. For transverse compression, the proposed model matches the experiment very closely predicting a 1.5% higher stress at 1% strain. Aboudi's model predicts a 21% lower strain than the proposed model, which results in it predicting a 19% lower than experimental stress at 1% strain.

A comparison of the shear stress strain response of the models compared to the experimental response is given in Figure 3.13. At 1% strain the proposed model predicts an 11% higher stress than the experimental results. Similarly to the axial compression case, there is curvature to the shear stress strain response. The point of divergence is at around 0.65% strain. Aboudi's model predicts 116% higher stress than the proposed model at all strains, which results in a predicted stress which is 140% too large at 1% strain.

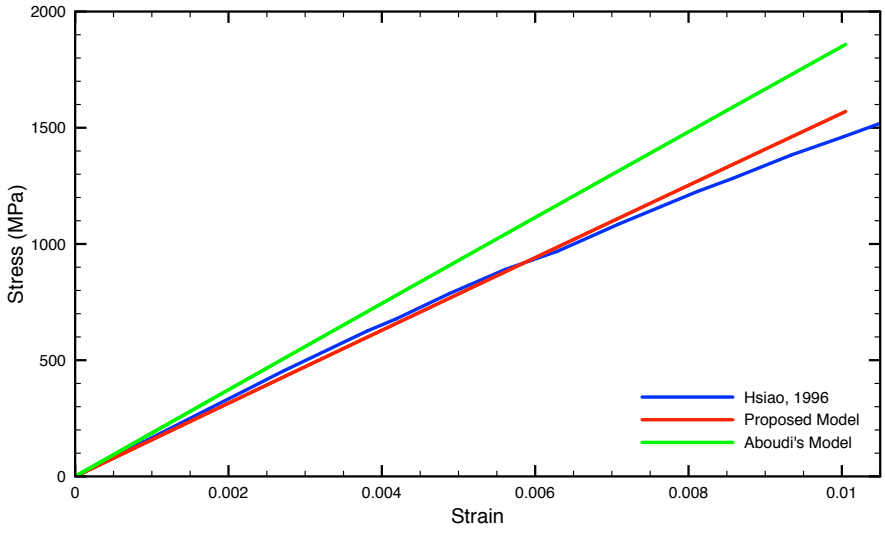

Figure 3.11: Axial compression stress strain response of the proposed model and Aboudi's model compared to the experimental data of Hsiao and Daniel [104] [150]

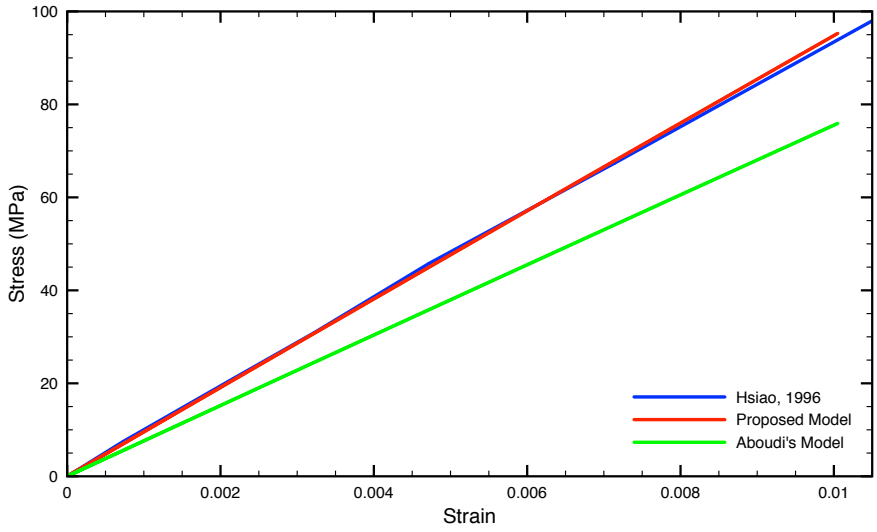

Figure 3.12: Transverse compression stress strain response of the proposed model and Aboudi's model compared to the experimental data of Hsiao and Daniel [104] [150]

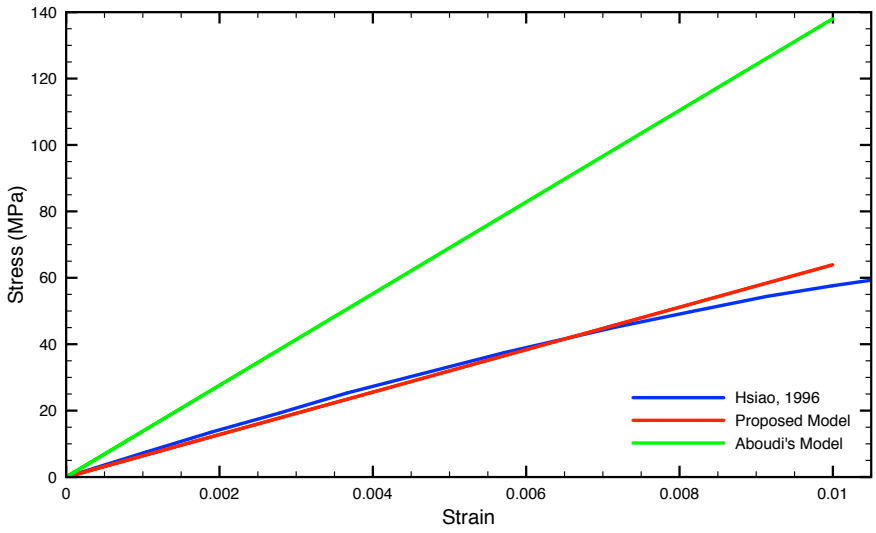

Figure 3.13: Shear stress strain response of the proposed model and Aboudi's model compared to the experimental data of Hsiao and Daniel [104] [150]

3.2.3 Comparison with Data from Kyriakides et al., 1995

The third set of data for comparison is for a unidirectional AS4 carbon fibre in an APC-2 Poly(ethyl ether ketone) (PEEK) matrix composite system published by Kyriakides et al. [120]. Stress strain data for uniaxial tension and compression in the fibre direction and transverse to the fibre direction where presented along with shear stress strain data. The material parameters used in the model calibration are given in Table 3.4. The fibre volume fraction for this composite system is 0.6. The stress strain response is compared up to 1 % strain, as with the previous data set.

Loading in the fibre direction for tension and compression is given in Figure 3.14 where the experimental stress strain results are compared to the proposed model and Aboudi's micromechanics model. In tension the experimental curve exhibited upward curvature resulting in Aboudi's model being a better fit in tension where as there is very good agreement for the proposed model in compression. In tension at 1% strain the proposed model under-predicts the stress by 9% where as Aboudi's model over-predicts the response by 1.3%. Aboudi's model predicts 12% higher stress than the proposed model for the given calibration. In compression at 1% strain the proposed model over-predicts the stress by 6.8% where Aboudi's model over predicts the stress by 19.5%. In compression, the proposed model is a very good match up to 0.7% strain where the response transitions to

Table 3.4: Model parameters for AS4/APC-2 composite to match the experimental data of Kyriakides et al.

AS4 Fibre	
E_{f_A} (GPa)	214
E_{f_T} (GPa)	13.8
$G_{f_{TA}}$ (GPa)	13.8
ν_{f_T}	0.2
$\nu_{f_{TA}}$	0.28
APC-2 PEEK	
E_m (GPa)	4.10
ν_m	0.356
Interphase	
k	0.71
l	1

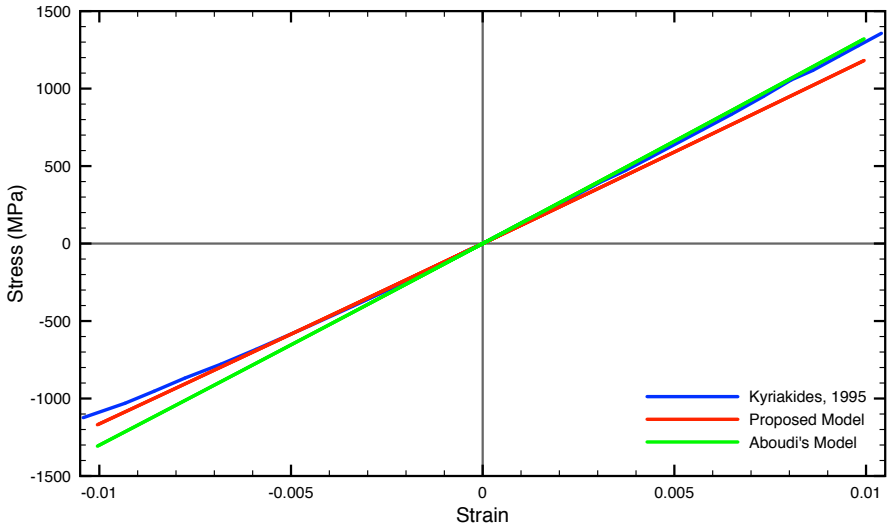

Figure 3.14: Fibre direction stress strain response of the proposed model and Aboudi's model compared to the experimental data of Kyrakides et al. [120] [150]

plastic behaviour.

The results for loading in the direction transverse to the fibres is shown in Figure 3.15 where the experimental data is compared to the prediction from the proposed model and Aboudi's model. Under transverse tension the experiment failed at under 1% strain.

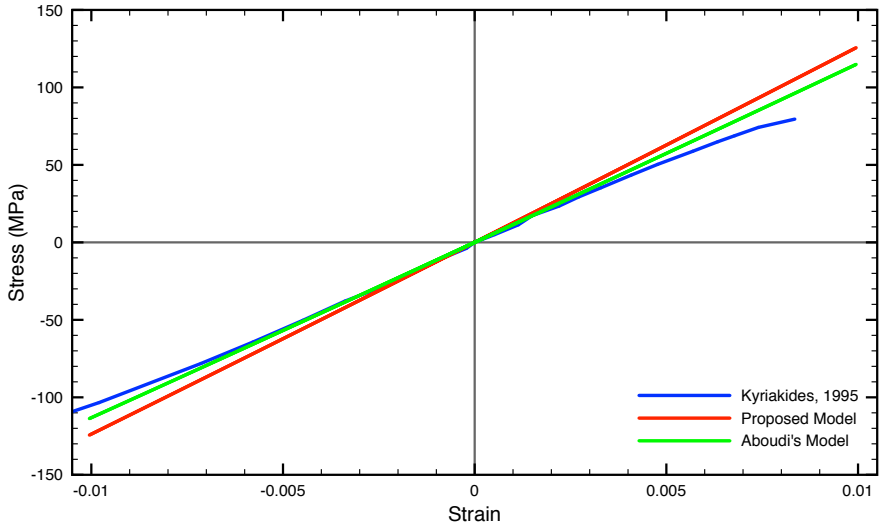

Figure 3.15: Transverse fibre direction stress strain response of the proposed model and Aboudi's model compared to the experimental data of Kyrakides et al. [120] [150]

A comparison of the models' predictions was conducted at 0.5% strain as there was a clear early onset of plasticity in the composite system. In tension the proposed model over predicts the stress by 19.8% where as Aboudi's model only over predicts the stress by 9.7%. In compression, the proposed model over predicts the stress at 0.5% strain by 11.4%, Aboudi's model only over predicts the stress by 1.8% at the same strain. Aboudi's model predicts an 8.5% lower stress for a given strain compared to the proposed model.

The shear stress strain response is compared between the proposed model, Aboudi's model and the experiment in Figure 3.16. In shear, nonlinear deformation onsets at a much lower strain compared to the axial and transverse fibre directions and the stress is compared at a shear strain of 0.25%. The proposed model over predicts the stress by 8% at this strain and Aboudi's model over predicts the stress by 138% at this strain. Aboudi's model predicts a 119% higher stress than the proposed model over the strain range compared.

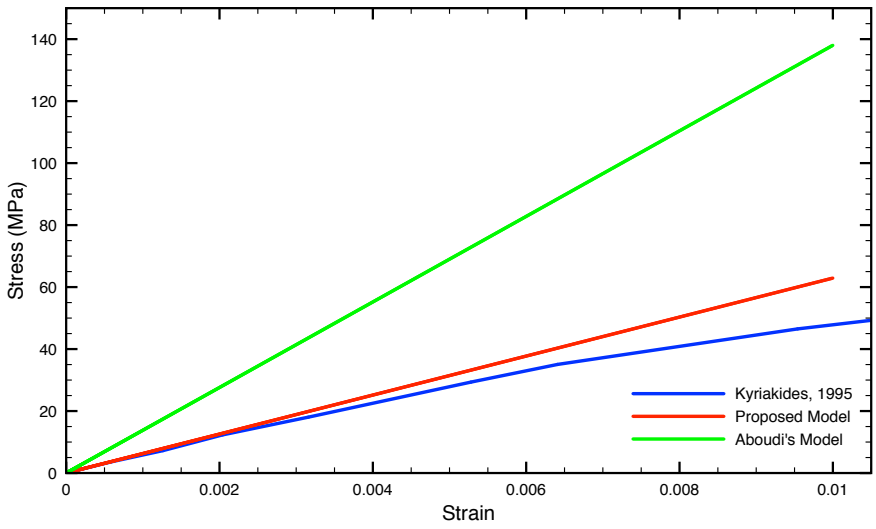

Figure 3.16: Shear stress strain response of the proposed model and Aboudi's model compared to the experimental data of Kyrakides et al. [120] [150]

3.3 Discussion

The material parameters used in the calibration were not obtained from the respective papers where the experimental results were published as they were not included in the papers. Most of the parameters came from Chamis who published the material properties of similar class materials such as the AS4 and IM6G fibres [44]. In particular, the transverse properties of the fibres is not given when fibres are assumed to be isotropic. A key assumption of this model which allows it to accurately predict the transverse stiffness is that the fibres are transversely isotropic, allowing for a reduced stiffness in the plane normal to the fibre direction. Other models change the assumption to not having equal strain in the fibre and matrix which induces the curvature seen in Aboudi's model over the range of volume fractions in Figure 3.10.

The transverse fibre properties are relatively hard to obtain compared to the axial properties. Experimentally, the transverse properties of individual fibres are tested by compressing them in between glass slides however the measurements are very difficult to complete as the fibre diameter is on the order of 10 micro meters. The contact of fibre on the glass slides leads to stress concentrations, which affect the resulting material properties. Measurement of the very small force and displacement of the individual fibres also leads

to increased measurement error and uncertainty. Often fibre properties are found inversely by performing experimental measurement on a composite and using a micromechanics model to calculate the fibre properties. The problem with this approach is that the fibre properties are dependent on the model and assumptions of the model formulation.

Comparing the transverse stress strain results of Aboudi's model to the proposed model the intersection point is at $V_f = 0.72$. At volume fractions above this Aboudi's model predicts a higher stress where as volume fractions below this the proposed model predicts a higher stress. It is interesting to note that this cross over point occurs near the upper limit of the fibre volume fraction arising from the assumed square fibre packing arrangement. The proposed model requires the transversely isotropic fibre assumption to bring the stress back in line with experimental data due to the Voigt assumption. the transverse predictions could be further improved through the use of strain localization in the fibre such as by the method introduced by Eshelby [62].

The results for the axial fibre direction are a close match to the experimental result for both models. This is a much easier problem to solve for as one can obtain the axial properties of fibres through single fibre testing where the ends of a single fibre are imbedded in matrix material. Such tests provide accurate results as the interface between the fibre and matrix does not fail through fibre pull out.

It is also possible to experimentally measure the matrix properties for some classes of polymer materials, however the presence of the fibres does have an effect on the material properties of the matrix. Li et al. have shown through the use of transmission electron microscopy and energy dispersive x-ray analysis that the degree of curing of a thermosetting resin changes as a function of radial position around fibres due to bonds established with the sizing on the fibres [125]. Reactions of the sizing change the amount of specific elements in the resin as a function of radial position away from the fibre [125]. These experimental techniques used by Li e al. could be to determine the bounds of the interphase zone.

Another method that could be used to determine the size of the interphase zone is nano-indentation. Karger-Kocsis et al. have reviewed the recent advancements and experimental characterization of the interphase [115]. The fibre sizing also effects the size of the interphase zone and the functionality.

The stress strain response of the matrix material has been simplified to linear elastic, however in reality polymers exhibit rate, temperature, and stress triaxiality dependent response. These effects are also present in the elastic regime, which could explain the differences in the stress strain response between tension and compression with the experimental data from Kyriakides et al. Weeks and Sun have demonstrated the strain rate dependence of the AS4/Peek system [178].

3.4 Conclusions of Elastic Model

The elastic response of a unidirectional composite system is modeled using the functionally graded interphase model. The model consists of a unit cell containing a single representative fibre, which is surrounded by a functionally graded interphase where the elastic properties change as a function of radial position. Four interphase functions are proposed to define this transition in material properties within the interphase. The material pairing parameters k and l are fit to match the stress strain response of the composite. In the model, the effects of the Voigt assumption as an upper bound on the elastic response is reduced through an effective modification of the fibre volume fraction. Coupled with the assumption of a transversely isotropic fibre this allows for accurate prediction of the material's elastic response in all directions.

The results predicted by the model are similar to those of Aboudi's model and it is possible to calibrate the interphase parameters to match the results of Aboudi's model. The exception is in the transverse direction due to the Voigt assumption. The use of the interphase allows for improved prediction of the elastic stress strain response of composite materials as the material pairing constants are adjusted to match the experimental results. There is also a physical interpretation of the functionally graded interphase which has been observed experimentally. The model calculates the overall stress from the stress of the individual phases. The stress in both the fibre and matrix phases are stored for use in implementation of failure theories.

3.5 Summary of Model Limitations

The limitations of this model are:

- It is limited to elastic deformation and is not applicable to the point of failure
- It is limited to a maximum fibre volume fractions of 0.77 resulting from the assumed square packing
- The strains in the fibre and matrix are assumed to be the same which is not correct for the implementation of strain based failure
- The transitions within the interphase zone have discontinuous derivatives at the boundaries
- The rate and stress state dependent response of the polymer material is neglected

Chapter 4

Generalized Functionally Graded Interphase Model

Polymers are known to exhibit an elasto-visco-plastic material response and therefore this behaviour must be accounted for in the model. Whereas the elastic model discussed previously assumed that the fibres were transversely isotropic and the strain was equal between the phases, the generalized model assumes that the strain in the fibre arises due to Eshelby's inclusion problem [62]. The generalized model assumes that the stress state changes as a function of position within the interphase, whereas previously, it was the material properties that were changing. This assumption is applicable to elastic, plastic, and viscous effects of the material response. It is also noted that the elastic assumption made previously is a sub set of the generalized solution as by changing the elastic properties in a functionally graded manner results in the stress changing as a function of position related to the functionality of the interphase.

4.1 Model Formulation

For the generalized model the same unit cell approximation given in Figure 3.1 is used. As the Voigt assumption is no longer used, the deformation is no longer constant across the unit cell. The deformation is subdivided into three regions based on the functionality of the interphase. The three regions are shown in Figure 4.1 where the white region is the bulk matrix deformation region, the yellow region is the interphase matrix deformation region and the green region is the representative fibre deformation region.

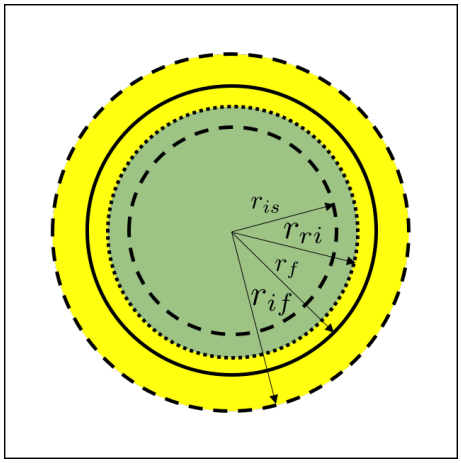

Figure 4.1: Deformation regions of the unit cell model defined by the interphase radii

The critical radii for the definition of the deformation regions are the representative interface radius (r_{ri}), which is the boundary between the representative fibre deformation region and the interphase matrix deformation region, and the interphase finish radius (r_{if}), which is the boundary between the interphase matrix deformation region and the bulk matrix deformation region. The interphase finish radii are a function of the material pairing constant l, which has the relation given in Eq. 3.17. The representative interface radius is a function of the integration of the interphase functions.

4.1.1 Stress Based Functionally Graded Interphase Functions

For the generalized model the interphase functions are defined using a stress gradient in any direction. The stress in the interphase varies between that of the fibre (σ_f) and the stress state of the bulk matrix material (σ_{bm}). It is important to note that the fibre stress is different from the representative fibre stress as they act over different regions. The interphase end points are (r_{is}, σ_f) and (r_{if}, σ_{bm}). Additional polynomial functions up to a quartic function are defined to describe the stress gradient within the interphase. The number of control points required to define a polynomial is $o+1$ where o is the order of the polynomial function. The control points used in defining the interphase functions consist of the values of the function at the end points and the derivatives of the function at the end points along with values or derivatives of the function evaluated at other locations.

Linear Interphase Function

The two stress values at the end points of linear interphase function are used as control points for the interphase function. The control points of the interphase function are (r_{if}, σ_{bm}) and (r_{is}, σ_f). The stress as a function of radius in the interphase zone is given by

$$\sigma(r) = -\left(\frac{\sigma_f - \sigma_{bm}}{r_{if} - r_{is}}\right) r + \frac{\sigma_f r_{if} - \sigma_{bm} r_{is}}{r_{if} - r_{is}} \tag{4.1}$$

Eq. (4.1) is integrated over the interphase zone in cylindrical coordinates to obtain the volume of the difference in stress in the interphase zone $v_{\Delta\sigma}$, which is calculated as

$$v_{\Delta\sigma} = \int_0^{2\pi} \int_{r_{is}}^{r_{if}} \int_{\sigma_{bm}}^{\sigma(r)} r d\sigma dr d\theta \tag{4.2}$$

Substituting for the interphase function

$$v_{\Delta\sigma} = \int_0^{2\pi} \int_{r_{is}}^{r_{if}} \int_{\sigma_{bm}}^{-\left(\frac{\sigma_f - \sigma_{bm}}{r_{if} - r_{is}}\right) r + \frac{\sigma_f r_{if} - \sigma_{bm} r_{is}}{r_{if} - r_{is}}} r d\sigma dr d\theta \tag{4.3}$$

Evaluating the integral, the resulting volume of difference in stress is

$$v_{\Delta\sigma} = \frac{\pi}{3} \left(r_{if} - r_{is}\right) \left(r_{if} + 2r_{is}\right) \left(\sigma_f - \sigma_{bm}\right). \tag{4.4}$$

Equating the volume found through integration given in Eq. 4.4 to the volume of a tube with end points at σ_f and σ_{bm}, with an outer radius of r_{ri} and inner radius of r_{is} given as

$$v_{\Delta\sigma} = \pi \left(\sigma_f - \sigma_{bm}\right) \left(r_{ri}^2 - r_{is}^2\right), \tag{4.5}$$

which is rearranged to calculate the representative interface radius r_{ri} as

$$r_{ri} = \sqrt{\frac{v_{\Delta\sigma}}{\sigma_f - \sigma_{bm}} + r_{is}^2}. \tag{4.6}$$

The representative interface radius for the linear interphase function is calculated as

$$r_{ri} = \sqrt{\frac{1}{3}\left(r_{if}^2 + r_{if} r_{is} + r_{is}^2\right)}, \tag{4.7}$$

which is the same result as for the linear elastic interphase function given in Eq. 3.24. This is a fairly obvious result as it has previously been shown that the representative interface radius is only a function of the interphase start and finish radii and has no dependence on the elastic constants or in this case the stress in the fibre and the stress of the bulk matrix.

Quadratic Interphase Functions

Three control points are required to define a quadratic interphase function. The stress at the two end points of the function are used as control points for the function. The third control point is defined by setting derivative of the interphase function to zero at one of the two ends. In this way two quadratic interphase functions are defined in the same way as for the elastic interphase functions, with the zero-derivative located at (r_{if}, σ_{bm}) and (r_{is}, σ_f).

For the case of the derivative evaluated at (r_{is}, σ_f) the interphase function defines radius as a function of stress, which is given as

$$r(\sigma) = \frac{r_{if} - r_{is}}{(\sigma_{bm} - \sigma_f)^2}(\sigma - \sigma_f)^2 + r_{is}. \tag{4.8}$$

The order of integration has to be changed as the function is defined differently as radius as a function of stress as opposed to stress as a function of radius.

$$v_{\Delta\sigma} = \int_0^{2\pi} \int_{\sigma_{bm}}^{\sigma_f} \int_{r_{is}}^{r(\sigma)} r dr d\sigma d\theta \tag{4.9}$$

Solving the integral by substituting Eq. 4.8 into Eq. 4.9 the volume of difference of stress is

$$v_{\Delta\sigma} = \frac{\pi}{15}\left(r_{if} - r_{is}\right)\left(3r_{if} + 7r_{is}\right)\left(\sigma_f - \sigma_{bm}\right), \tag{4.10}$$

which is substituted into Eq. 4.6 to calculate the representative interface radius as

$$r_{ri} = \sqrt{\frac{1}{5}r_{if}^2 + \frac{4}{15}r_{if}r_{is} + \frac{8}{15}r_{is}^2}. \tag{4.11}$$

Again this representative interface radius is equivalent to that calculated for the elastic interphase function given in Eq. 3.28.

The second quadratic interphase function arises from the derivative control point evaluated at (r_{if}, σ_m). In this quadratic interphase function the stress is given as a function of radius about the x_1 axis as

$$\sigma(r) = \frac{\sigma_f - \sigma_{bm}}{(r_{if} - r_{is})^2}(r - r_{if})^2 + \sigma_{bm}. \tag{4.12}$$

The interphase function is integrated as per Eq. 4.2 to calculate the volume of difference of stress which is

$$v_{\Delta\sigma} = \frac{\pi}{6}\left(\sigma_f - \sigma_{bm}\right)\left(r_{if} + 3r_{is}\right)\left(r_{if} - r_{is}\right). \tag{4.13}$$

The representative interface radius is calculated using Eq. 4.6, for the quadratic interphase function given in Eq. (4.12) it is

$$r_{ri} = \sqrt{\frac{1}{6}r_{if}^2 + \frac{1}{3}r_{if}r_{is} + \frac{1}{2}r_{is}^2}, \tag{4.14}$$

which again is equivalent to the representative interface radius for the elastic case given in Eq. 3.32.

Cubic Interphase Function

Four control points are used to define a cubic function, the values of the points at the end points of the functions (r_{if}, σ_{bm}) and (r_{is}, σ_f) are known and the derivative of the function at those points is set to zero giving the four control points. The stress as a function of position within the interphase zone is given as

$$\sigma(r) = \frac{\sigma_f - \sigma_{bm}}{\frac{1}{6}\left(r_{if}^3 - r_{is}^3\right) + \frac{1}{2}\left(r_{if}r_{is}^2 - r_{is}r_{if}^2\right)}\left[\frac{1}{3}r^3 - \frac{r_{is} - r_{if}}{2}r^2 + r_{is}r_{if}r + \frac{r_{if}^3}{6} - \frac{r_{is}r_{if}^2}{2}\right] + \sigma_{bm}. \tag{4.15}$$

This is integrated using Eq. 4.2 to calculate the volume of difference in stress as

$$v_{\Delta\sigma} = \frac{\pi}{10}(\sigma_f - \sigma_{bm})(3r_{if} - 7r_{is})(r_{if} - r_{is}). \tag{4.16}$$

The representative interface radius is then calculated using Eq. 4.6 resulting in the following representative interface radius

$$r_{ri} = \sqrt{\frac{3}{10}r_{if}^2 + \frac{4}{10}r_{if}r_{is} + \frac{3}{10}r_{is}^2}. \tag{4.17}$$

A plot of the cubic interphase function and its associated representative interface radius is shown in Figure 4.2.

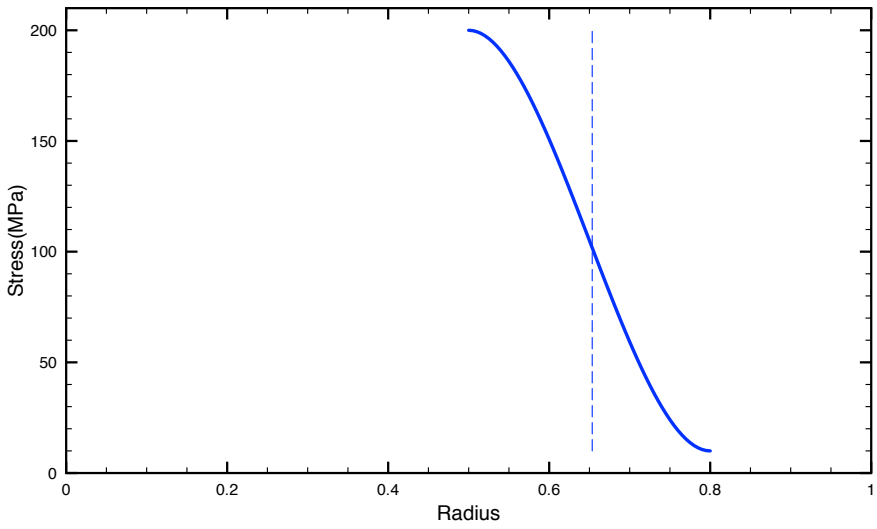

Figure 4.2: Cubic interphase function and associated representative interface radius defined around the x_1 axis of the unit cell

Quartic Interphase Function

To define a quartic function, a fifth control point is required. At the end points of the function the values are known and the derivatives are set to zero which gives four control points. The fifth control point defines the stress half way between r_{is} and r_{if} and has the following coordinate in cylindrical coordinates about the x_1 axis of the unit cell $\left(\frac{r_{if}+r_{is}}{2}, m(\sigma_f - \sigma_{bm}) + \sigma_{bm}\right)$ where the parameter m is added to define the stress as having a value between σ_{bm} and σ_f by varying the parameter m between 0 and 1. Using the five control points along with the new material pairing parameter m the quartic interphase function is easily calculated as

$$\begin{aligned}\sigma(r) = \frac{1}{(r_{if}-r_{is})^4}\Big[&(\sigma_f - \sigma_{bm})\left((16m-8)\,r^4 - (32mr_{if} + 32mr_{is} - 18r_{if} - 14r_{is})\,r^3\right.\\ &+ \left(16mr_{if}^2 + 64mr_{if}r_{is} + 16mr_{is}^2 - 11r_{if}^2 - 32r_{is}r_{if} - 5r_{is}^2\right)r^2\\ &- \left(32r_{if}^2 r_{is} + 32mr_{if}r_{is}^2 - 22r_{if}^2 r_{is} - 10r_{if}r_{is}^2\right)r + 16mr_{if}^2 r_{is}^2\Big)\\ &+ \sigma_f\left(r_{if}^4 - 4r_{if}^3 r_{is} - 5r_{if}^2 r_{is}^2\right) + \sigma_{bm}\left(11r_{if}^2 r_{is}^2 - 4r_{if}r_{is}^3 + r_{is}^4\right)\Big].\end{aligned} \tag{4.18}$$

The volume of difference in stress is calculated by substituting Eq. 4.18 into Eq. 4.2 resulting in

$$v_{\Delta\sigma} = \frac{\pi}{30}\left(\sigma_f - \sigma_{bm}\right)\left(16mr_{if} + 16mr_{is} + r_{if} + 13r_{is}\right). \tag{4.19}$$

Again, this volume is used in Eq. 4.6 to calculate the representative interface radius resulting in

$$r_{ri} = \frac{1}{30}\sqrt{480m\left(r_{if}^2 - r_{is}^2\right) + 30r_{if}^2 + 360r_{if}r_{is} + 510r_{is}^2}. \tag{4.20}$$

Note that unlike the other interphase functions, which result in the representative interface radius being a function of r_{if} and r_{is} this interface radius is also a function of the material pairing parameter m, which was introduced for this interphase function. A plot of the quartic interphase functions and their associated representative interface radii is given in Figure 4.3 for 6 different values of m. It is observed that for a low m value such as $m = 0.0$

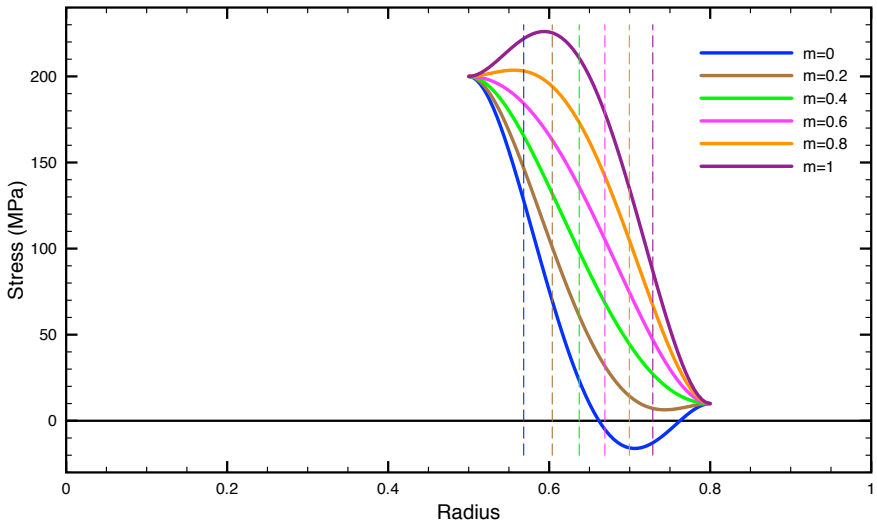

Figure 4.3: Quartic interphase functions and their associated representative interface radii defined around the x_1 axis of the unit cell for varying m values

the sense of the stress switches from tension to compression or compression to tension depending on the stress state, which is not physically possible. Therefore, m values should not be less than approximately 0.2 to avoid this issue.

Comparison of Interphase Functions

The proposed polynomial interphase functions are compared for a set of endpoints in Figure 4.4. The associated representative interface radii for the interphase functions shown

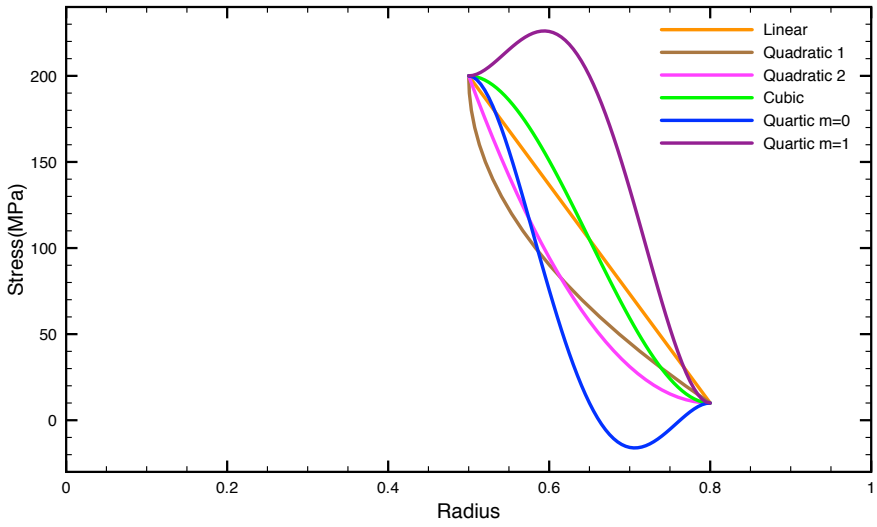

Figure 4.4: Comparison of the interphase functions defined around the x_1 axis of the unit cell

in Figure 4.4 are illustrated in Figure 4.5 along with the interphase bounds r_{is}, r_{if}, and r_f. It is noted that the two quadratic interphase functions give almost identical representative interface radii. The linear and cubic interphase functions also give nearly identical representative interface radii. The quartic interphase function provides the largest range of representative interface radii along with the derivatives being continuous at the ends, which is why it is used in all future model calibrations.

4.1.2 Deformation Partitioning

The fibre strain is calculated using Eshelby's solution, for a single infinitely long cylindrical inclusion. For the case of our unit cell the representative fibre extends to the ends of the unit cell, such that there is a finite length fibre within the unit cell. The important distinction is that in the fibre direction, the end effects are ignored and it is assumed that the strain

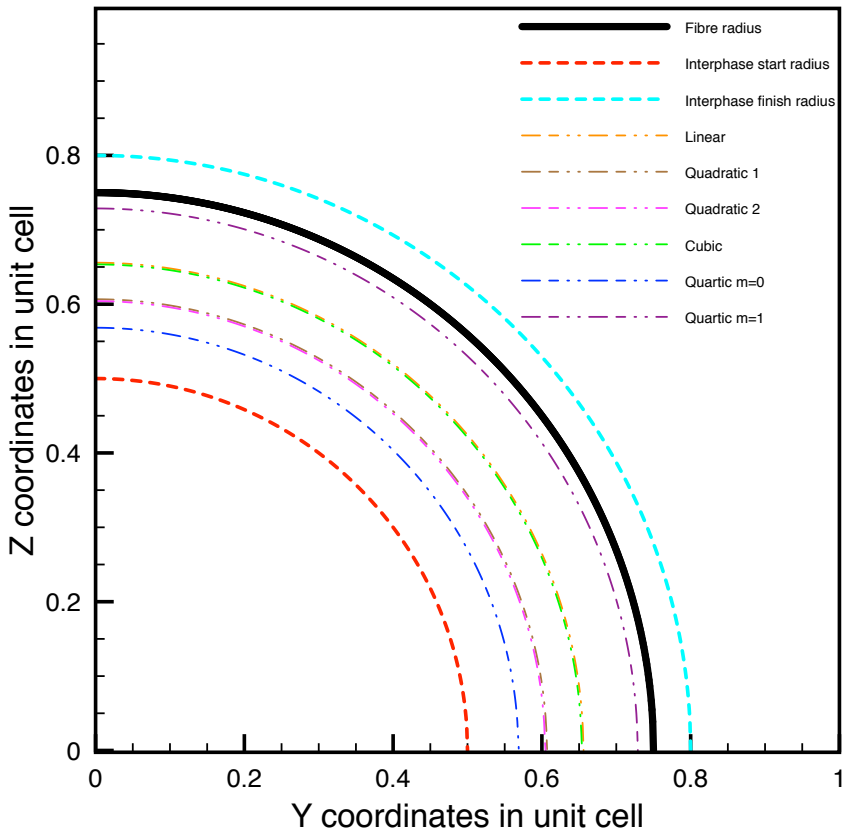

Figure 4.5: Comparison of the representative interface radii on the plane normal to x_1

in the x_1 direction is the same for the fibre as the overall unit cell, which is the result of the infinitely long cylindrical inclusion. The representative fibre strain is calculated as

$$\varepsilon_{rf} = \mathbb{T}\varepsilon \tag{4.21}$$

where ε is the strain applied to the far field, which in our case is equivalent to the overall unit cell strain. The strain localization tensor is given in Eq. 2.4. Eshelby's inclusion tensor for the case of an infinitely long cylindrical inclusion is

$$\mathbb{S}_f = \begin{bmatrix} 0 & 0 & 0 & 0 & 0 & 0 \\ \frac{\nu_m}{2-2\nu_m} & \frac{5-4\nu_m}{8-8\nu_m} & \frac{4\nu_m-1}{8-8\nu_m} & 0 & 0 & 0 \\ \frac{\nu_m}{2-2\nu_m} & \frac{4\nu_m-1}{8-8\nu_m} & \frac{5-4\nu_m}{8-8\nu_m} & 0 & 0 & 0 \\ 0 & 0 & 0 & \frac{1}{4} & 0 & 0 \\ 0 & 0 & 0 & 0 & \frac{3-4\nu_m}{8-8\nu_m} & 0 \\ 0 & 0 & 0 & 0 & 0 & \frac{1}{4} \end{bmatrix}. \tag{4.22}$$

The elasticity tensors $\mathbb{L}_m$ and $\mathbb{L}_f$ are the isotropic elasticity tensor for the matrix material and the transversely isotropic elasticity tensor for the fibre given in Eq. 3.2 and Eq. 3.3 respectively.

The strain is partitioned using compatibility between the phases which is enforced through the displacement gradients. The deformation is partitioned into three segments volumetrically as

$$\mathbf{G} = V_{rf}\mathbf{G}_{rf} + V_{im}\mathbf{G}_{im} + (1 - V_{rf} - V_{im})\mathbf{G} \tag{4.23}$$

where $\mathbf{G}$ is the overall displacement gradient applied to the unit cell, V_{im} is the volume fraction of the interphase matrix portion, $\mathbf{G}_{rf}$ is the displacement gradient in the representative fibre and $\mathbf{G}_{im}$ is the displacement gradient in the matrix portion of the interphase.

The overall displacement gradient is known as it is applied to the unit cell. The fibre displacement gradient is calculated from the overall displacement gradient through the strain localization tensor using the proof shown in Section 4.1.2. The matrix portion of the interphase displacement gradient is calculated as

$$\mathbf{G}_{im} = \frac{\mathbf{G}(V_{rf} + V_{im}) - V_{rf}\mathbf{G}_{rf}}{V_{im}} \tag{4.24}$$

Fibre Displacement Gradient Proof

We will start by assuming that the fibres undergo small strain to failure and therefore, only undergo infinitesimal strain prior to failure. Infinitesimal strain is defined as

$$\varepsilon_{ij} = \frac{1}{2}\left(\frac{\partial u_i}{\partial x_j} + \frac{\partial u_j}{\partial x_i}\right) \tag{4.25}$$

where the indices i and j have values between one and three. For the case where $i = j$, the normal strain simplifies to

$$\varepsilon_{ii} = \frac{\partial u_i}{\partial x_i}. \tag{4.26}$$

The displacement gradient $\mathbf{G}$ is defined as

$$\mathbf{G} = \begin{bmatrix} \frac{\partial u_1}{\partial x_1} & \frac{\partial u_1}{\partial x_2} & \frac{\partial u_1}{\partial x_3} \\ \frac{\partial u_2}{\partial x_1} & \frac{\partial u_2}{\partial x_2} & \frac{\partial u_2}{\partial x_3} \\ \frac{\partial u_3}{\partial x_1} & \frac{\partial u_3}{\partial x_2} & \frac{\partial u_3}{\partial x_3} \end{bmatrix}. \tag{4.27}$$

The deformation gradient $\mathbf{F}$ is related to the displacement gradient as

$$\mathbf{F} = \mathbf{G} + \mathbf{I}, \tag{4.28}$$

where $\mathbf{I}$ is the second order identity tensor. The deformation gradient can be written in terms of the displacement gradient as

$$\mathbf{F} = \begin{bmatrix} \frac{\partial u_1}{\partial x_1} + 1 & \frac{\partial u_1}{\partial x_2} & \frac{\partial u_1}{\partial x_3} \\ \frac{\partial u_2}{\partial x_1} & \frac{\partial u_2}{\partial x_2} + 1 & \frac{\partial u_2}{\partial x_3} \\ \frac{\partial u_3}{\partial x_1} & \frac{\partial u_3}{\partial x_2} & \frac{\partial u_3}{\partial x_3} + 1 \end{bmatrix}. \tag{4.29}$$

The deformation can be decomposed into either the left $\mathbf{V}$ or right $\mathbf{U}$ stretch tensor and a rotation $\mathbf{R}$ as

$$\mathbf{F} = \mathbf{VR} = \mathbf{RU} \tag{4.30}$$

respectively. We will assume that the fibres undergo no rotation such that the left and right stretch tensors are equivalent. We will also assume that the displacement gradient of the fibre is symmetrical such that

$$\frac{\partial u_i}{\partial x_j} = \frac{\partial u_j}{\partial x_i}. \tag{4.31}$$

We can therefore rewrite the off diagonal terms of the displacement gradient as

$$\frac{\partial u_i}{\partial x_j} = \frac{1}{2}\left(\frac{\partial u_i}{\partial x_j} + \frac{\partial u_j}{\partial x_i}\right), \tag{4.32}$$

which is equivalent to our infinitesimal strain tensor given in Eq. 4.25. The displacement gradient for the representative fibre is equivalent to the representative fibre strains and can be rewritten as

$$\mathbf{G}_{rf} = \begin{bmatrix} \varepsilon_{rf_{11}} & \varepsilon_{rf_{12}} & \varepsilon_{rf_{13}} \\ \varepsilon_{rf_{12}} & \varepsilon_{rf_{22}} & \varepsilon_{rf_{23}} \\ \varepsilon_{rf_{13}} & \varepsilon_{rf_{23}} & \varepsilon_{rf_{33}} \end{bmatrix}. \tag{4.33}$$

Therefore, the displacement gradient in the representative fibre is equivalent to the strain in the representative fibre

$$\mathbf{G}_{rf} = \varepsilon_{rf}. \tag{4.34}$$

4.1.3 Fibre Model

The representative fibre is assumed to deform elastically and the fibre stress is calculated from the fibre strain which is given by Eq. 4.21 as

$$\sigma_f = \mathbb{L}\varepsilon_{rf}. \tag{4.35}$$

4.1.4 Matrix Model

As discussed in Section 2.1.3 polymers do not follow typical metallic material models and require material models which have been developed specifically for polymeric materials. The model developed by the Buckley and co-authors [37, 36, 35] is implemented to simulate the response of an epoxy matrix material. The input to the glass rubber model is the deformation gradient $\mathbf{F}$. Two regions within the model use the glass rubber constitutive law, the bulk matrix region and the interphase matrix region. The deformation gradients for these regions are the overall deformation gradient $\mathbf{F}$ and the interphase matrix deformation gradient $\mathbf{F}_{im}$ respectively. The deformation gradient for the interphase matrix is calculated as

$$\mathbf{F}_{im} = \mathbf{G}_{im} + \mathbf{I}. \tag{4.36}$$

In this section the equations are derived in terms of the deformation gradient regardless of the specific region.

The volume ratio is defined in order to derive the deviatoric deformation gradient for the polymer

$$J = \det \mathbf{F}. \tag{4.37}$$

The deviatoric portion of the deformation gradient is then calculated as

$$\bar{\mathbf{F}} = J^{-\frac{1}{3}}\mathbf{F}. \tag{4.38}$$

Note that this differs from the classical continuum mechanics definition of

$$\bar{\mathbf{F}}_{ij} = \mathbf{F}_{ij} - \frac{1}{3}trace(\mathbf{F})\delta_{ij}, \tag{4.39}$$

and arises due to the partially incompressible nature of polymeric materials. The time derivative of the deviatoric deformation gradient $\dot{\bar{\mathbf{F}}}$ is required to calculate the deviatoric velocity gradient as

$$\bar{\mathbf{L}} = \dot{\bar{\mathbf{F}}}\bar{\mathbf{F}}^{-1}. \tag{4.40}$$

The deviatoric velocity gradient is decomposed into the symmetric and skew symmetric portions being the deviatoric deformation rate ($\bar{\mathbf{D}}$), and the spin ($\mathbf{W}$) respectively given as

$$\bar{\mathbf{D}} = \frac{1}{2}\left(\bar{\mathbf{L}} + \bar{\mathbf{L}}^T\right), \tag{4.41}$$

$$\mathbf{W} = \frac{1}{2}\left(\bar{\mathbf{L}} - \bar{\mathbf{L}}^T\right). \tag{4.42}$$

Note that the spin is independent of the velocity gradient being deviatoric and is therefore not a deviatoric quantity. The deviatoric left Cauchy Green tensor is calculated from the deviatoric deformation gradient as

$$\bar{\mathbf{B}} = \bar{\mathbf{F}}\bar{\mathbf{F}}^T \tag{4.43}$$

In the glass rubber model the stress is split into three components; the mean stress (σ_{mean}), the bond stretching stress ($\mathbf{S}_b$), and the conformational stress ($\mathbf{S}_c$). The mean stress is due to the volumetric change and is calculated from the matrix bulk modulus (K_m) as

$$\sigma_{mean} = K_m \ln J. \tag{4.44}$$

The relaxation time of the polymer includes viscous and creep effects and is crucial to calculating the bond stretching stress. It is assumed that the mean value of a relaxation spectra represents that spectrum of relaxation times, and that the relaxation time remains constant within the numerical integration scheme used to solve the problem. The bond stretching stress is updated objectively using the Jaumann rate ($\hat{\mathbf{S}}_b$) as

$$\dot{\mathbf{S}}_b = \hat{\mathbf{S}}_b + \mathbf{W}\mathbf{S}_b - \mathbf{S}_b\mathbf{W}. \tag{4.45}$$

The Jaumann rate is calculated as

$$\hat{\mathbf{S}}_b = 2G_b\bar{\mathbf{D}} - \frac{\mathbf{S}_b}{\tau} \tag{4.46}$$

where G_b is the shear modulus associated with bond stretching, and τ is the relaxation time. The first step in the calculation of the relaxation time is to calculate the octahedral bond stretching stress (σ_{oct}) as

$$\sigma_{oct} = \sqrt{\frac{1}{3}\mathbf{S}_b : \mathbf{S}_b}. \tag{4.47}$$

The viscous portion of the deformation rate is calculated as

$$\mathbf{D}_v = \bar{\mathbf{D}} - \frac{\hat{\mathbf{S}}_b}{2G_b}. \tag{4.48}$$

The viscous portion of the deformation rate is used to calculate the Mises average viscous strain (ε_v) as

$$\varepsilon_v = \sqrt{\frac{2}{3}\mathbf{D}_v : \mathbf{D}_v}. \tag{4.49}$$

The viscous strain is used to calculate the fictive temperature (T_{fic}) as

$$T_{fic} = T_{gl} + (T_{fft} - T_{gl})\left(1 - exp\left(-\frac{\varepsilon_v}{\varepsilon_0}\right)\right) \tag{4.50}$$

where T_{gl} is the glass transition temperature of the polymer, T_{fft} is the final fictive temperature of the polymer, and ε_0 is the reference rejuvenation strain range. The relaxation time is calculated as

$$\tau = \frac{V_s\sigma_{oct}}{2RT}\frac{\exp\left(-\frac{V_p\sigma_{mean}}{RT}\right)}{\sinh\left(\frac{V_s\sigma_{oct}}{2RT}\right)}\tau_0 \exp\left(\frac{C_t}{T_{fic} - T_\infty} - \frac{C_t}{T_{gl} - T_\infty} + \frac{\Delta H_0}{RT} - \frac{\Delta H_0}{RT_{gl}}\right) \tag{4.51}$$

where V_s is the shear activation volume, R is the universal gas constant, T is the temperature of the polymer, V_p is the pressure activation volume, τ_0 is the linear relaxation time at the reference conditions, C_t is the Cohen-Turnbull constant, T_∞ is the Vogel temperature, and ΔH_0 is the activation enthalpy.

The third contribution to the stress is the conformational stress. To evaluate this stress, first the eigenvalues ($\bar{\lambda}_k$) of the left Cauchy Green tensor given in Eq. 4.43 are calculated. The principal components of the conformational stress are calculated from the eigenvalues as

$$\mathbf{S}_{c_k} = \frac{\bar{\lambda}_k}{J}\frac{\partial A_{cm}}{\partial \bar{\lambda}_k} - P \qquad \text{for } k = 1, 2, 3 \tag{4.52}$$

where A_{cm} is the free energy function, and P is the pressure resulting from the constraint that the trace of the conformational stress is zero. The free energy function is

$$A_{cm} = \frac{N_s k_B T}{2}\left[\frac{(1+\eta)(1-\alpha^2)}{1-\alpha^2\sum_{i=1}^{3}\bar{\lambda}_i^2}\sum_{i=1}^{3}\frac{\bar{\lambda}_i^2}{1+\eta\bar{\lambda}_i} + \sum_{i=1}^{3}\ln\left(1+\eta\bar{\lambda}_i^2\right) + \ln\left(1-\alpha^2\sum_{i=1}^{3}\bar{\lambda}_i^2\right)\right] \tag{4.53}$$

where N_s is the density of the slip links in the polymer, k_B is the Boltzmann constant, η represents the freedom of movement in the slip links, and α is a measure of the inextensibility of the polymer chains. The principal stresses are rotated back to the reference frame using the associated eigenvectors (q_k) of the eigenvalues ($\bar{\lambda}_k$) calculated from the left Cauchy Green tensor ($\bar{\mathbf{B}}$), the conformational stress is

$$\mathbf{S}_c = \mathbf{S}_{c_k} q_k \otimes q_k \qquad \text{for } k = 1, 2, 3. \tag{4.54}$$

Note that superposition of the stress states applies for each of the three stress states rotated from the principal values.

The three stress contributions are added together to obtain the overall stress state of the polymer as

$$\sigma = \sigma_{mean} + \mathbf{S}_b + \mathbf{S}_c. \tag{4.55}$$

Note that it is assumed that temperature remains constant during the deformation, however it is possible to include temperature rise due to deformation in the future.

A major advantage the glass rubber model has over state variable based models is that all the parameters are physically based and can be measured through experimentation. The model is based on thermodynamics and is able to capture the temperature effects of the polymer, which is crucial for polymers when they are close to their glass transition temperatures.

4.1.5 Stress Calculation

The representative fibre volume fraction (V_{rf}) is calculated using Eq. 3.41. Additionally, the volume fraction of interphase matrix material is required, which is

$$V_{im} = \frac{\pi}{4}\left(r_{if}^2 - r_{ri}^2\right) \tag{4.56}$$

The average stress is calculated by volumetrically averaging the stress in each region as

$$\sigma = (1 - V_{im} - V_{rf})\,\sigma_{bm} + V_{im}\sigma_{im} + V_{rf}\sigma_f. \tag{4.57}$$

The average stress is used to compare the model predictions to experimental results.

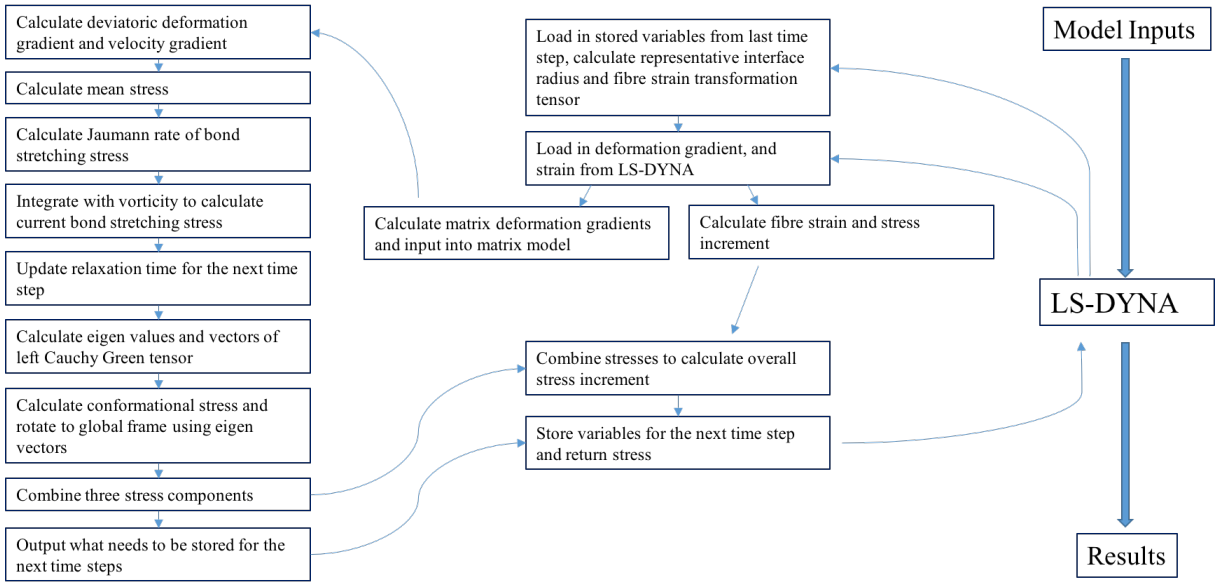

Figure 4.6: Flow chart of how the user defined material model works within LS-DYNA [149]

4.2 Model Implementation

The model described in section 4.1 is implemented in a user defined material model within LS-DYNA. The explicit dynamic solver in LS-DYNA is used. A flow chart showing how the user defined material model code is set up as shown in Figure 4.6. The model requires 24 input parameters comprising of material properties, and interphase parameters along with the interphase function to be used.

Two studies were conducted, the first using a 1 unit cubic element to replicate the quasi static results presented by Hsiao and Daniel [104], the second was to reproduce the results under moderate strain rates and used a sample of the same geometry as Hsiao and Daniel [105]. The second model geometry is a drop tower test specimen 24.5 mm tall, 12.7 mm wide and 8.7 mm thick made up of unidirectional aligned fibres. For the drop tower test the nodes on one of the contact faces where constrained from motion in the direction of the applied motion. They were only allowed to move in the plane normal to the applied displacement to prevent barreling of the specimen. The nodes along the opposite face had an applied velocity controlled displacement applied to them, but were also free to move in the plane normal to the applied velocity. The velocity was ramped up to the required velocity to achieve the reported strain rates, the strain rates, velocities and simulation

Table 4.1: Prescribed velocities and simulation times to replicate the results from Hsiao and Daniel [105], note the value in parenthesis is for axial compression

Strain rate (/s)	Velocity (mm/msec)	Simulation time (msec)
120	3.048	0.31
110	2.794	0.1
10	0.254	0.92
2	0.0508	16.65
0.4	0.01016	21.03
0.01	0.000254	3456[795]

times for the drop tower tests are given in Table 4.1.

4.3 Results

Material parameter calibrations were carried out for the two different model set ups considered at quasi static strain rates and with strain rate sensitivity. A quartic interphase function was used for the calibration of both, as it offers the most tune ability of r_{ri} as shown in Figure 4.4. The material parameters for both models are given in Table 4.2. The values of the material constants for the polymer matrix material were calibrated within the range of data provided by Buckley et al. for epoxy matrix materials [35]. The material system for both of the experimental works that are being compared is IM6G/3501-6 carbon epoxy prepreg.

Table 4.2: Material parameters for both models

Material Parameter	Quasi-static	Strain rate sensitive
Fibre modulus (GPa)	279	279
Fibre Poisson's ratio	0.2	0.2
Fibre volume fraction	0.6	0.6
Matrix shear modulus for bond stretching stress (G_b) (GPa)	1.3	2.0
Matrix bulk modulus (K_m) (GPa)	4.6	4.3
Matrix activation enthalpy (ΔH_0) ($kJmol^{-1}$)	102	102
Matrix glass transition temperature (T_{gl}) (K)	383	445
Matrix Vogel temperature (T_∞) (K)	331	375
Matrix Cohen Turnbull constant (C_t) (K)	2068	2068
Matrix shear activation volume (V_s) (m^3mol^{-1})	2.23×10^{-3}	1.43×10^{-3}
Matrix pressure activation volume (V_p) (m^3mol^{-1})	2.06×10^{-4}	2.06×10^{-4}
Matrix linear relaxation time (τ_0) (msec)	3.49×10^{12}	3.3×10^{9}
Matrix final fictive temperature (T_{fft}) (K)	413	465
Matrix rejuvenation strain range (ε_0)	0.337	0.330
Matrix slip link density (N_s) (m^{-3})	4.58×10^{27}	6.16×10^{27}
Matrix inextensiability factor of the network (α)	0.288	0.310
Matrix freedom of sliplink movement (η)	0	0
Interphase inner bound (i)	0.70	0.85
Interphase outer bound (l)	1.15	1.13
Interphase quartic parameter (m)	0.25	0.40
Temperature (K)	293	293

4.3.1 Quasi Static Results

Compression along the fibre direction, and transverse to the fibre direction along with pure shear. Modelling was carried out using a single element of size 1 unit, at a quasi-static strain rate of 0.01/s. The model is calibrated to the transverse compression curve as it is most effected by the polymer stress strain behaviour. The transverse compression stress strain curve is given in Figure 4.7. The model matches the experimental curve very well

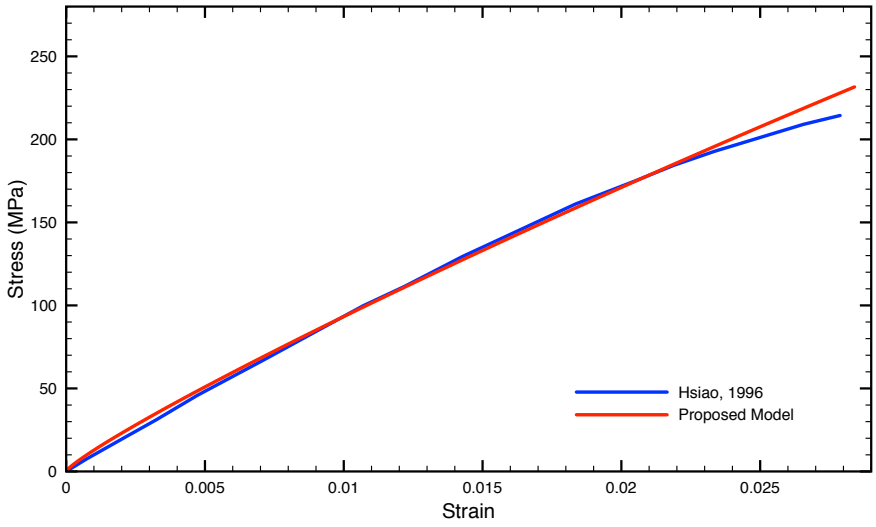

Figure 4.7: Quasi static transverse compression stress strain results compared with experimental data from [104] [149]

up to 2.25% strain. After that, the model over-predicts the stress. The divergence of the model predictions is likely due to the onset of failure in the experiment resulting in damage, which is not accounted for in the model. The likely failure modes for this loading are matrix microcracking and fibre matrix debonding, which are discussed in [18, 19, 20]. Another possible explanation is that as the matrix deforms plastically the deformation in the fibre is no longer described by Eq. 4.21 as the strain localization considers the total strain in the bulk matrix portion and does not consider the effects of including plastic strains in the scheme.

For validation, the model is compared to the axial compression and shear. The axial compression is given in Figure 4.8. Under axial compression there is a good match between the model and experiment up until 0.8% strain where the stress strain response deviates.

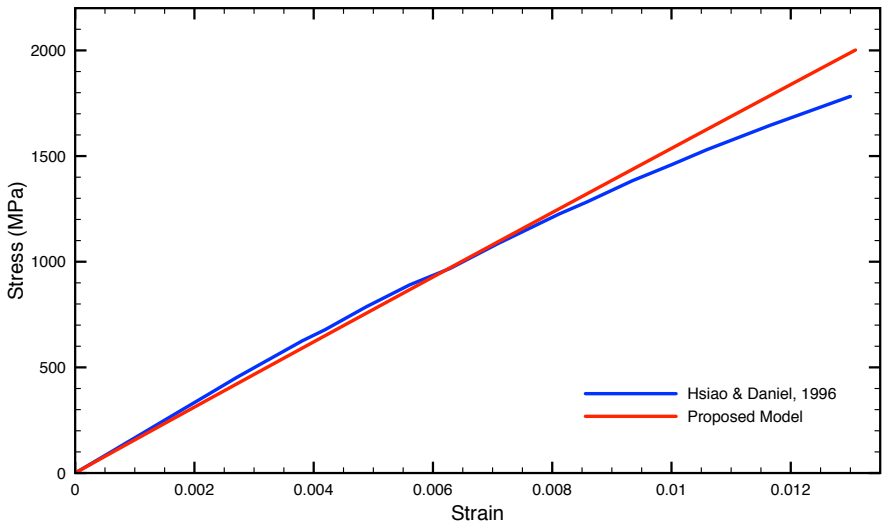

Figure 4.8: Quasi static axial compression stress strain results compared to experimental data from [104] [149]

In the experimental work of Hsiao and Daniel the effects of fibre waviness were observed [104], the model does not include these effects. Fibre waviness could lead to an increase and earlier onset to fibre microbuckling, which also leads to matrix micro cracking and fibre matrix debonding. None of these failure modes are accounted for in the model.

The second validation is against the shear data shown in Figure 4.9. It is observed that the proposed model over predicts the stress strain response up to 0.65% strain then there is excellent correlation until 1.45% strain where the models diverge again. The over prediction in the elastic regime is interesting as elasticity was captured more accurately in Figure 3.13 when the strain in the fibre and matrix were equal. The difference at the higher strains is again attributed to the onset of failure modes not accounted for in the model.

4.3.2 Rate Sensitive Results

Hsiao and Daniel also conducted drop tower testing on thick unidirectional composites to evaluate the strain rate sensitivity of the material [105]. Finite element modelling was conducted on a sample of the same dimensions as mentioned previously and typical stress distributions for the loadings considered are shown in Figure 4.10. It is noted that there

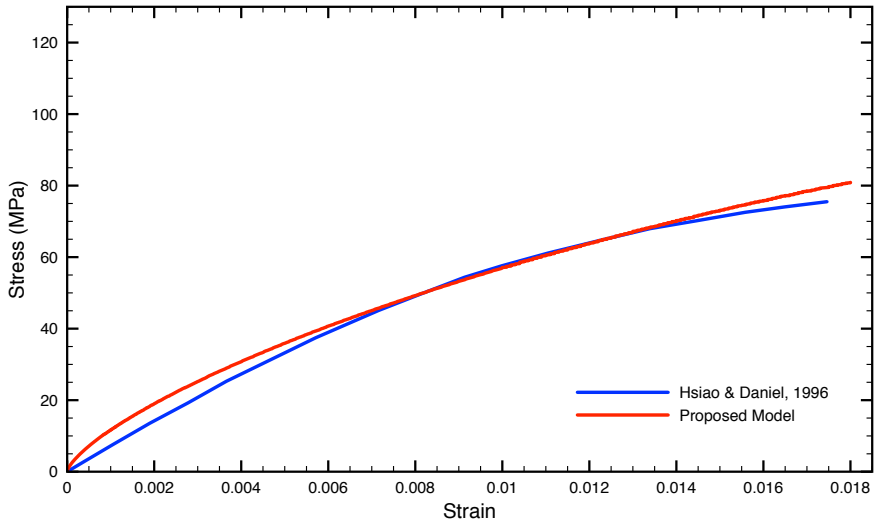

Figure 4.9: Quasi static shear stress strain results compared to experimental data from [104] [149]

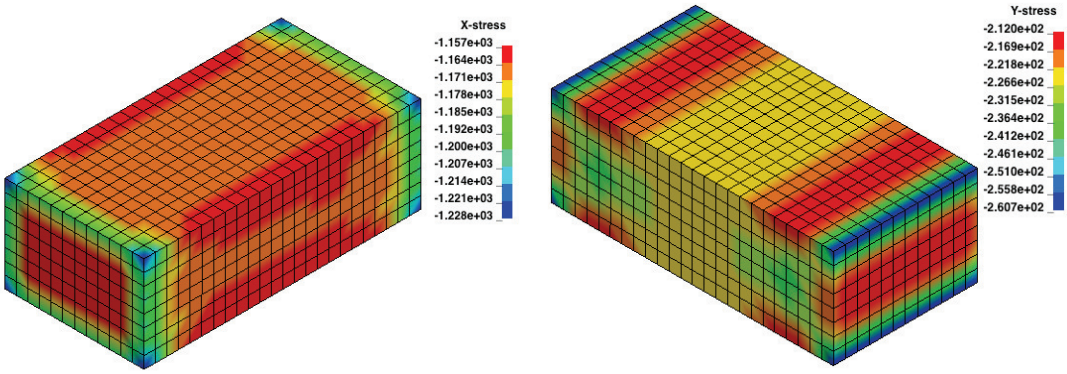

(a) Axial 0.4/s (b) Transverse 2/s

Figure 4.10: Typical stress distributions in the specimens subjected to the two loading conditions [149]

is a reduction in stress at the ends of the specimen where the boundary conditions are applied. The stress strain curves shown in the results are the average of the elements at the middle of the specimen to avoid the effects of the boundary conditions from Saint Venant's principle.

The material only exhibits strain rate sensitivity when subjected to transverse compression as the deformation is dominated by the matrix material response. The model parameters were calibrated for the 120/s and 2/s strain rate and validated with the 0.01/s stress strain response. The transverse compression stress strain response is shown in Figure 4.11. To evaluate the model's accuracy a plot of the percentage error between the model

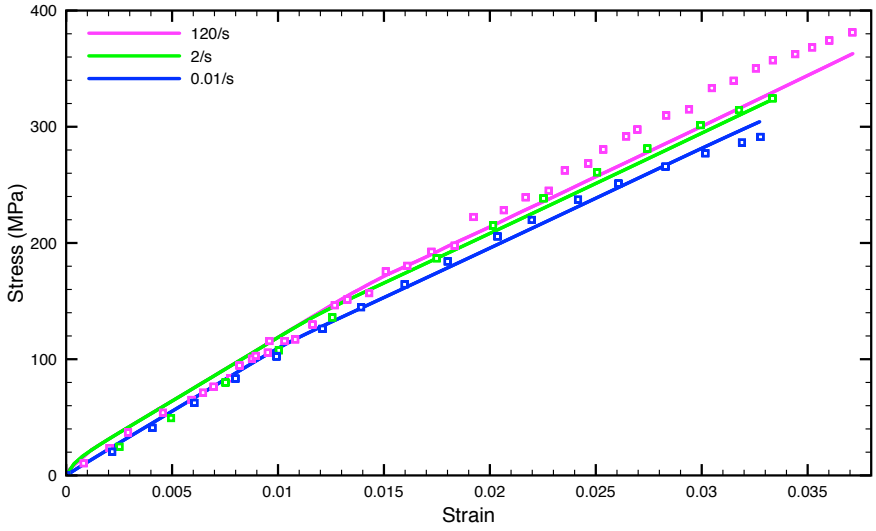

Figure 4.11: Transverse compression stress strain results compared to experimental data from [105] (points) [149]

and the experimental data points versus the strain is given in Figure 4.12. Note the first two data points for the 2/s and 120/s strain rate are excluded as they are above the range given in the graph, around 20-50% over prediction. At the lower strain values the percent difference is much higher as a difference of 5 MPa at 10 MPa stress is 50% versus 5% at 100 MPa stress levels. For strains above 1.3% the 2/s and 0.01/s model predicts ±5% of the experimental stress. The 120/s curve under-predicts the stress strain response above 2% strain to a maximum of 8% under the experimental response. The jaggedness of the 120/s curve is due to the results in [105] being presented as the raw data points versus the curves given for the other two strain rates.

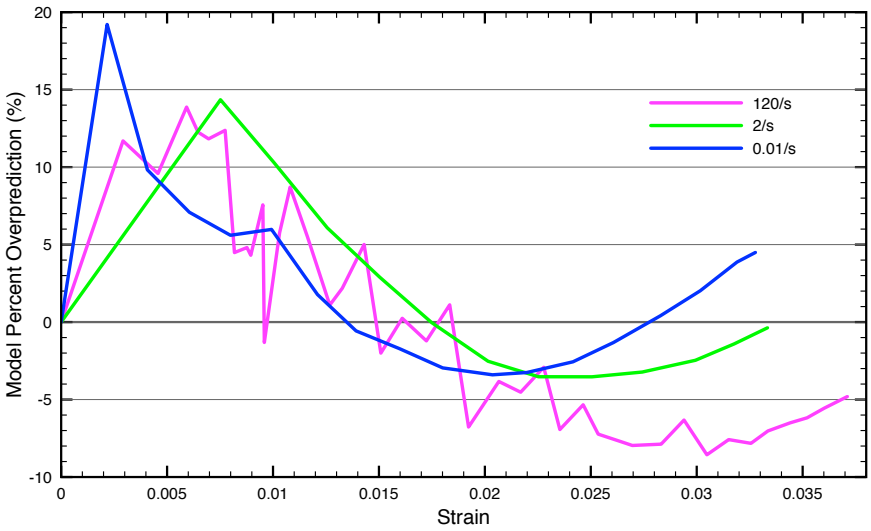

Figure 4.12: Comparison of the difference in the transverse compressive results between the proposed model and experimental data from [105] [149]

Under axial compression the material does not exhibit strain rate sensitivity as shown in Figure 4.13. The stress strain response of the different strain rates is co-linear as the fibre elasticity dominates the response. The only difference between the curves is the failure point. The strain to failure increases with increasing strain rate. The failure modes are not currently accounted for in the model. It is interesting to note that the axial stress strain response is different from those presented in Figure 4.8 where there was fibre waviness leading to more fibre micro buckling.

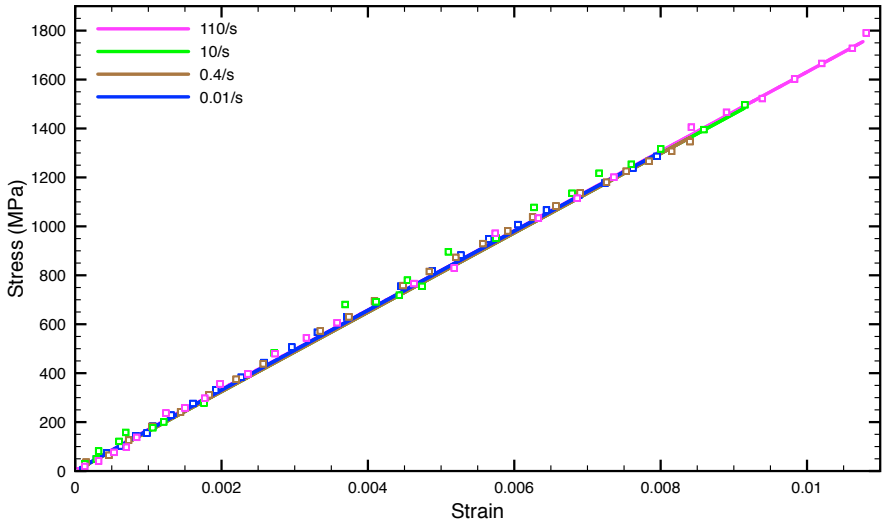

Figure 4.13: Rate sensitive axial compression response with experimental data from [105] represented as points [149]

4.3.3 Mesh Sensitivity Study

A mesh sensitivity study was conducted for transverse compression at 120/s strain rate. The element size used in the previous study was 1 mm cube hexahedral element. Herein the element size is varied from 0.5 mm to 3 mm to observe the effects of the element size on the models results. The effects of element size on computation time are also explored. Stress contour plots of the four element sizes considered are shown in Figure 4.14 for the same applied strain. As the element size is increased, the details of stress concentrations are lost, although the average stress stays the same. Therefore, higher mesh density near stress concentrations is advised to better capture the onset of failure when it is incorporated in the model.

The stress strain response for the four different mesh sizes is given in Figure 4.15. The change in element size has little consequences on the stress strain response of the model and the model is independent of mesh size. The only advantage to using a smaller mesh size is the extra detail obtained around stress concentrations.

Another important aspect to consider is whether the additional computational time is worth the detail gained through using a finer mesh. The total computation time required to complete the analysis of the four different mesh sizes is shown in Figure 4.16. It takes

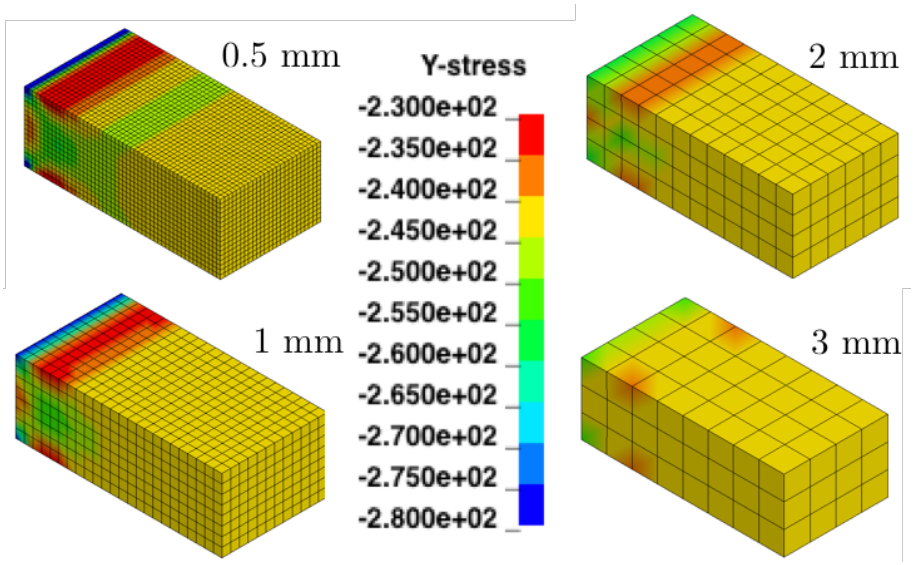

Figure 4.14: Stress contour plot results with varying mesh size subjected to transverse compression [149]

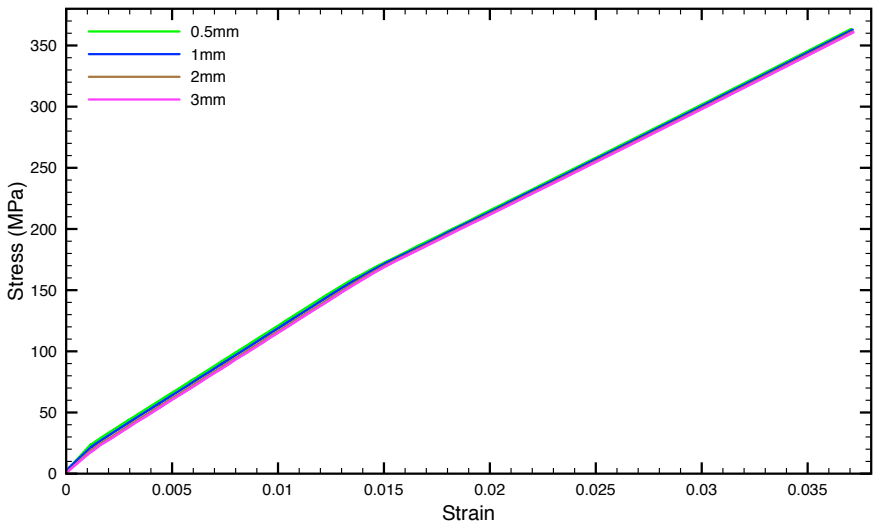

Figure 4.15: Results with varying mesh size subjected to transverse compression [149]

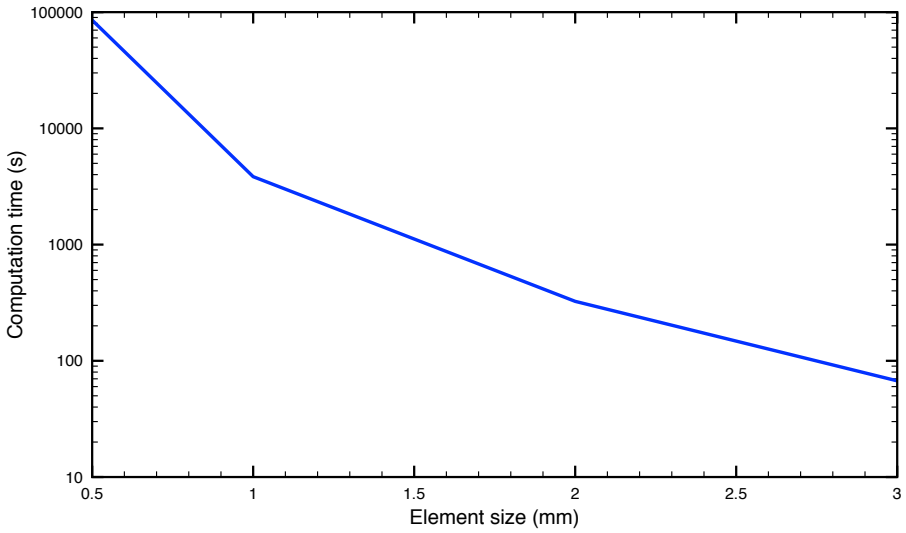

Figure 4.16: Computation time versus element size for the mesh sensitivity analysis [149]

nearly 1270 times more time to complete the simulation with 0.5 mm elements as compared to 3 mm elements. For the 0.5 mm mesh it requires over 24 hours of computation time to produce the results. It takes 22.2 times as long for the 0.5 mm mesh as the 1 mm mesh used for the analysis in the previous section and still captures nearly the same level as detail. Going to smaller element size results in a smaller explicit time step as well as increasing the number of locations the problem is solved so it has two negative consequences. It is recommended that the larger elements are used to reduce computation time while maintaining the accuracy of the stress strain response.

4.4 Discussion

The functionally graded interphase can be thought of as an infinite number of concentric layers surrounding the fibre where the stress traction changes ever so slightly to produce a nearly perfect interface between the layers. As such, equilibrium is slightly violated across the interphase. Each of these regions has its own associated displacement gradient which average to the interphase matrix displacement gradient $\mathbf{G}_{im}$. Adding additional layers in the interphase would complicate the problem and result in the stress and strain calculation being required in each additional portion of the interphase zone.

The stress is defined as a function of radial position, which is an axisymmetric definition of the stress state. This is misleading as the model was subjected to non-axisymmetric loads. The definition of the FGI is more general in describing how any stress component changes between that of the fibre and that of the bulk matrix material in three-dimensional space.

The strain partitioning assumes that the strain in the fibre is related to the overall strain applied to the unit cell. This strain contains both elastic and plastic contributions from the matrix material regions. In the transverse direction, the plastic strain in the matrix reduces the stress compared to the elastic assumption inherent in Eshelby's solution. Therefore, it is expected that as the matrix material deforms plastically less strain occurs in the fibres, which would reduce the stress predicted by the model at higher strains when matrix plasticity is present.

4.5 Conclusions

The elasto-visco-plastic response of a unidirectional composite material has been modeled using a stress based functionally graded interphase and Eshelbian strain partitioning. The model shows excellent agreement when compared with experimental data up to the onset of failure. A mechanism based glass rubber model is able to capture the intricacies of polymer material behaviour when combined with the elastic fibre material model to predict the response of the composite system. The functionally graded interphase allows for compatibility between the materials while maintaining quasi equilibrium between the phases.

The results are independent of the number of elements used in the analysis and there are major gains in computation time when using larger elements. The incorporation of failure or a better strain partitioning technique is required to improve the prediction of the model up to the point of failure. With the models implemented five orders of magnitude of strain rates have been simulated within 10% accuracy of the published experimental data using a single set of input parameters.

4.6 Summary of Model Limitations

The limitations of this model are:

- It is limited to fibre volume fractions up to 0.77 from the square packing

- The fibre is assumed to undergo no rotations
- The total strain is limited to approximately 20% due to the assumptions regarding the fibre strain, the theory breaks down after this point
- The interphase matrix volume fraction must be a positive non-zero quantity
- The model does not account for changes in the strain partitioning due to permanent deformation in the matrix
- The model does not account for failure

Chapter 5

Incremental Strain Partitioning

In the generalized functionally graded interphase model, the strain in the fibre is related to the total strain applied to the unit cell as per Eq. 4.21. The strain in the bulk matrix, which is equivalent to the strain applied to the unit cell has both elastic and plastic portions of strain in it at higher strains due to the plasticity in the matrix material. At higher strain, the matrix material deforms plastically and there is no longer a linear relationship between stress and strain. Thus, it is expected that less strain is transferred to the fibre from the applied deformation to the bulk matrix material.

Two methods have been developed to deal with this problem of non-linear behaviour by the homogenization of elasto plastic materials, known as the tangent and secant approach [56]. In both of these methods the elasticity tensors $\mathbb{L}_f$ and $\mathbb{L}_m$ are modified using either the tangent or secant modulus for the strain localization calculation given in Eq. 2.4. The tangent modulus method considers the derivative of the stress strain curve at the given stress and strain as

$$E = \frac{d\sigma}{d\varepsilon}. \tag{5.1}$$

The secant method considers the total stress and strain to develop the secant modulus as

$$E = \frac{\sigma}{\varepsilon}. \tag{5.2}$$

For a small strain, the moduli predicted using the two methods coincide with the elastic modulus. For larger strains the tangent modulus is lower than the secant modulus and it has been found that the experimental measured stress strain response is somewhere between the results generated by the tangent and secant method for updating the effective elastic tensors in the strain partitioning calculation [56].

5.1 Model Formulation

The version of LS-DYNA being used is an explicit dynamic finite element code, which uses forward Euler time integration. In a user defined material model, LS-DYNA provides the deformation gradient to calculate the next stress state $\mathbf{F}_{(t+1)}$ as well as the overall strain increment $\Delta\varepsilon_{(t+1)}$ and expects to be returned the stress in the element $\sigma_{(t+1)}$.

For our case the fibres are always elastic materials, such that they act linearly up until failure. Only the matrix material needs to undergo modification in the model to the elasticity tensor to account for plasticity. Instead of using an average modulus based on either the tangent or secant methods, a method to derive a new elastic tensor was proposed from the relationship:

$$\Delta\sigma_{bm} = \mathcal{L}\Delta\varepsilon_{bm}, \tag{5.3}$$

which is rearranged to solve for the pseudo elastic tensor as

$$\mathcal{L} = \Delta\sigma_{bm}\Delta\varepsilon_{bm}^{-1}. \tag{5.4}$$

$\mathcal{L}$ is known as the pseudo elastic tensor for the matrix and replaces $\mathbb{L}_m$ in Eq. 2.4. In Eq. 5.4 the strain is inverted as a 3 by 3 tensor, then represented in Voigt notation as a 1 x 6 and the stress as a 6 x 1 matrix. The resulting pseudo elastic tensor is a 6 x 6, which is the same size as the regular elasticity tensors $\mathbb{L}_m$ that it replaces. However, this expansion results in a non-symmetric pseudo elastic tensor and leads to stability issues with the explicit dynamic implementation. It also requires the calculation of a new pseudo elastic tensor for each time step in the explicit dynamic integration scheme and inversion of a 6 x 6 in the strain localization calculation.

As the fibres only undergo elastic deformation up to failure, a new mathematical approach was explored. What would happen to a composite material, which is loaded into matrix plasticity and subsequently unloaded? From cyclic loading assuming that the material unloads to zero stress, the elastic portion of the strain in both the fibres and matrix would be recovered. The permanent deformation in the bulk matrix would remain which arises due to matrix plasticity and viscous effects. It is postulated that for a composite with an elastic fibre, the strain in the representative fibre is related to the far field elastic strain in the bulk matrix material as

$$\varepsilon_{rf} = \mathbb{T}\varepsilon_{bm}^{(e)} \tag{5.5}$$

where $\varepsilon_{bm}^{(e)}$ is the elastic portion of the strain in the bulk matrix material.

5.1.1 Incremental deformation partitioning

As the matrix material model is time dependent and the simulations being performed are dynamic in nature and implemented in an explicit dynamic time integration scheme, the model is incremental in nature and the representative fibre strain increment is related to the bulk matrix elastic strain increment as

$$\Delta\varepsilon_{rf(t+1)} = \mathbb{T}\Delta\varepsilon^{(e)}_{bm(t+1)}. \tag{5.6}$$

The element deformation in the finite element analysis is equivalent to the bulk matrix deformation. The deformation gradient is the input to the glass rubber constitutive framework used to calculate the stress update for the matrix material given in Section 4.1.4. It is assumed that if the material is unloaded, the overall stress and bulk matrix stress become zero. The recoverable portion of the strain from unloading is the elastic strain experienced by the bulk matrix and is due to the elastic recovery of the stress. Therefore, in our incremental framework we calculate the bulk matrix elastic strain from the bulk matrix stress increment as

$$\Delta\varepsilon^{(e)}_{bm(t+1)} = \mathbb{L}_m^{-1}\Delta\sigma_{bm(t+1)} \tag{5.7}$$

where $\Delta\sigma_{bm(t+1)}$ is the bulk matrix stress increment used to update the stress for the next time step, it is also assumed that the stress recovery in the matrix is isotropic elastic in nature.

The fibre strain increment is used to determine the deformation that the interphase portion of the matrix undergoes to satisfy compatibility conditions. It is assumed that the fibres experience zero spin or rotation, and they only undergo small deformations before failure, therefore the total fibre strain is equivalent to the representative fibre displacement gradient as

$$\mathbf{G}_{rf(t+1)} = \varepsilon_{f(t+1)}. \tag{5.8}$$

The total representative fibre strain for the next time step is determined by adding the increment in representative fibre strain to the total representative fibre strain from the previous time step

$$\varepsilon_{rf(t+1)} = \varepsilon_{rf(t)} + \Delta\varepsilon_{rf(t+1)}. \tag{5.9}$$

The deformation in the matrix portion of the interphase is calculated by volumetrically averaging the displacement gradients to ensure that compatibility is maintained between the phases. The displacement gradient in the matrix portion of the interphase is

$$\mathbf{G}_{im(t+1)} = \frac{\mathbf{G}_{(t+1)}(V_{rf} + V_{im}) - \mathbf{G}_{rf(t+1)}V_{rf}}{V_{im}} \tag{5.10}$$

where $\mathbf{G}_{(t+1)}$ is the overall displacement gradient calculated from the deformation gradient $\mathbf{F}_{(t+1)}$ provided by the finite element code to calculate the stress at the next time step. The overall displacement gradient is calculated as

$$\mathbf{G}_{(t+1)} = \mathbf{F}_{(t+1)} - \mathbf{I}. \tag{5.11}$$

The overall displacement gradient is equivalent to displacement gradient for the bulk matrix material, and $\mathbf{G}_{rf(t+1)}$ is the displacement gradient of the representative fibre given in Eq. 5.8. The volume fractions are given in Eq. 3.41 and Eq. 4.56 for the fibre and interphase matrix respectively. The deformation gradient of the interphase matrix material is input to the glass rubber constitutive law given in Section 5.1.2 to calculate the stress in the matrix portion of the interphase. The deformation gradient is related to the displacement gradient as

$$\mathbf{F}_{im(t+1)} = \mathbf{G}_{im(t+1)} + \mathbf{I}, \tag{5.12}$$

which is the reverse operation to Eq. 5.11.

5.1.2 Glass rubber model implementation

The glass rubber model outputs the total stress from the deformation gradient and history variables stored from the previous time step. For the glass rubber model, the deformation gradient is modified to separate the deviatoric components. The volume ratio is defined as

$$J_{(t+1)} = \left|\mathbf{F}_{(t+1)}\right|. \tag{5.13}$$

The deviatoric portion of the deformation gradient for the polymeric material is

$$\bar{\mathbf{F}}_{(t+1)} = J_{(t+1)}^{-\frac{1}{3}} \mathbf{F}_{(t+1)}. \tag{5.14}$$

The time derivative of the deviatoric deformation gradient is required to calculate the velocity gradient, which is calculated as

$$\dot{\bar{\mathbf{F}}}_{(t+1)} = \frac{\bar{\mathbf{F}}_{(t+1)} - \bar{\mathbf{F}}_{(t)}}{\Delta t} \tag{5.15}$$

where $\bar{\mathbf{F}}_{(t)}$ is the solution to Eq. 5.14 at the last time step and Δt is the explicit dynamic time step. The deviatoric velocity gradient is

$$\bar{\mathbf{L}}_{(t+1)} = \dot{\bar{\mathbf{F}}}_{(t+1)} \bar{\mathbf{F}}_{(t+1)}^{-1}. \tag{5.16}$$

The velocity gradient is used to calculate the deformation rate and spin as the symmetric and skew symmetric portions of the deviatoric velocity gradient respectively given as

$$\bar{\mathbf{D}}_{(t+1)} = \frac{1}{2}\left(\bar{\mathbf{L}}_{(t+1)} + \bar{\mathbf{L}}^T_{(t+1)}\right) \tag{5.17}$$

$$\mathbf{W}_{(t+1)} = \frac{1}{2}\left(\bar{\mathbf{L}}_{(t+1)} - \bar{\mathbf{L}}^T_{(t+1)}\right) \tag{5.18}$$

where the spin is not deviatoric, since the skew symmetric portion is not effected by the modification to the deformation gradient. The last kinetics calculation of the deformation gradient is to calculate the left Cauchy Green tensor from the deviatoric deformation gradient

$$\bar{\mathbf{B}}_{(t+1)} = \bar{\mathbf{F}}_{(t+1)}\bar{\mathbf{F}}^T_{(t+1)}. \tag{5.19}$$

The mean stress is calculated from the matrix bulk modulus and volume ratio as

$$\sigma_{mean(t+1)} = K_m \ln J_{(t+1)}. \tag{5.20}$$

It is assumed that the mean relaxation time for the relaxation spectrum is used for all calculations and that the relaxation time is constant within a time step. The deviatoric bond stretching stress is updated objectively using the Jaumann rate increment as

$$\mathbf{S}_{b(t+1)} = \Delta\hat{\mathbf{S}}_{b(t+1)} + \Delta t\left[\mathbf{W}_{(t+1)}\mathbf{S}_{b(t)} - \mathbf{S}_{b(t)}\mathbf{W}_{(t+1)}\right]. \tag{5.21}$$

The Jaumann rate increment is calculated as

$$\Delta\hat{\mathbf{S}}_{b(t+1)} = \left(1 - \exp\left(-\frac{\Delta t}{\tau_{(t)}}\right)\right)\left[2G_{bm}\tau_{(t)}\bar{\mathbf{D}}_{(t+1)} - \mathbf{S}_{b(t)}\right] \tag{5.22}$$

where $\tau_{(t)}$ is the relaxation time calculated in the last time step, and G_{bm} is the bond stretching shear modulus.

To calculate the relaxation time for the next time step, first the equivalent octahedral stress is calculated from the bond stretching stress

$$\sigma_{oct(t+1)} = \sqrt{\frac{1}{3}\mathbf{S}_{b(t+1)} : \mathbf{S}_{b(t+1)}}. \tag{5.23}$$

Next, the viscous portion of the deformation rate is calculated as

$$\mathbf{D}_{v(t+1)} = \bar{\mathbf{D}}_{(t+1)} - \frac{\hat{\mathbf{S}}_{b(t+1)}}{2G_{bm}} \tag{5.24}$$

where and $\hat{\mathbf{S}}_{b(t+1)}$ is the Jaumann rate of bond stretching stress, which is calculated as

$$\hat{\mathbf{S}}_{b(t+1)} = 2G_{mb}\bar{\mathbf{D}}_{(t+1)} - \frac{\mathbf{S}_{b(t+1)}}{\tau_{(t)}}. \tag{5.25}$$

This is different than the Jaumann rate increment used to update the stress. The viscous strain is then calculated as

$$\varepsilon_{v(t+1)} = \varepsilon_{v(t)} + \Delta t\sqrt{\frac{2}{3}\mathbf{D}_{v(t+1)} : \mathbf{D}_{v(t+1)}} \tag{5.26}$$

where the viscous strain $\varepsilon_{v(t)}$ is stored as a history variable. The fictive temperature is calculated as

$$T_{fic(t+1)} = T_{gl} + (T_{fft} - T_{gl})\left(1 - \exp\left(-\left(\frac{\varepsilon_{v(t+1)}}{\varepsilon_0}\right)^{r_{fit}}\right)\right). \tag{5.27}$$

The relaxation time for the next time step $\tau_{(t+1)}$ is calculated as

$$\tau_{(t+1)} = \frac{V_s\sigma_{oct(t+1)}}{2RT}\frac{\exp\left(-\frac{V_p\sigma_{m(t+1)}}{RT}\right)}{\sinh\left(\frac{V_s\sigma_{oct(t+1)}}{2RT}\right)}\exp\left(\frac{C}{T_{fic(t+1)} - T_\infty} - \frac{C}{T_{gl} - T_\infty} + \frac{\Delta H_0}{RT} - \frac{\Delta H_0}{RT_{gl}}\right)\tau_0. \tag{5.28}$$

The third contribution to the stress is from the conformational stress. The eigenvalues ($\bar{\lambda}_{k(t+1)}$) and eigenvectors of the left Cauchy Green tensor ($\bar{\mathbf{B}}_{(t+1)}$) are calculated to find the principal values. The principal portions of the conformational stress are calculated using

$$\mathbf{S}_{c_k(t+1)} = \frac{\bar{\lambda}_{k(t+1)}}{J}\frac{\partial A_{cm(t+1)}}{\partial\bar{\lambda}_{k(t+1)}} - p \qquad \text{for } k = 1,2,3 \tag{5.29}$$

where p is the pressure arising from the trace of the conformational stress being zero. $A_{cm(t+1)}$ is the free energy function, which is calculated as

$$A_{cm(t+1)} = \frac{N_s k_B T}{2}\left[\begin{array}{c}\frac{(1+\eta)(1-\alpha^2)}{1-\alpha^2\sum_{i=1}^{3}\bar{\lambda}^2_{i(t+1)}}\sum_{i=1}^{3}\frac{\bar{\lambda}^2_{i(t+1)}}{1+\eta\bar{\lambda}^2_{i(t+1)}} \\ +\sum_{i=1}^{3}\ln(1+\eta\bar{\lambda}^2_{i(t+1)}) + \ln\left(1-\alpha^2\sum_{i=1}^{3}\bar{\lambda}^2_{i(t+1)}\right)\end{array}\right] \tag{5.30}$$

The principal stresses are rotated back to the reference frame using the eigenvectors ($q_{k(t+1)}$) of the left Cauchy Green tensor to calculate the conformational stress as

$$\mathbf{S}_{c(t+1)} = \mathbf{S}_{c_k(t+1)}q_{k(t+1)} \otimes q_{k(t+1)}. \tag{5.31}$$

The total stress for the glass rubber constitutive law is returned to the user defined material model by adding the three stress components

$$\sigma_{(t+1)} = \sigma_{m(t+1)} + \mathbf{S}_{b(t+1)} + \mathbf{S}_{c(t+1)}. \tag{5.32}$$

5.1.3 Stress update and LS-DYNA implementation

In the user defined material model, the stress increment for the bulk matrix and interphase matrix is calculated by subtracting the current total stress calculated by the glass rubber model from the stress calculated for the next time step as

$$\Delta\sigma_{bm(t+1)} = \sigma_{bm(t+1)} - \sigma_{bm(t)}, \tag{5.33}$$

$$\Delta\sigma_{im(t+1)} = \sigma_{im(t+1)} - \sigma_{im(t)}. \tag{5.34}$$

The stress increment in the bulk matrix Eq. 5.33 is used as input to Eq. 5.6 to calculate the fibre strain increment and the deformation gradient for the matrix portion of the interphase. The fibre stress increment is calculated using the fibre strain increment calculated in Eq. 5.6 and the fibre elastic tensor as

$$\Delta\sigma_{f(t+1)} = \mathbb{L}_f \Delta\varepsilon_{f(t+1)}. \tag{5.35}$$

The stress for the overall material is updated by volumetrically averaging the stresses in each constituent as

$$\sigma_{(t+1)} = \sigma_{(t)} + V_{rf}\Delta\sigma_{f(t+1)} + V_{im}\Delta\sigma_{im(t+1)} + (1 - V_{rf} - V_{im})\Delta\sigma_{bm(t+1)}, \tag{5.36}$$

which is an objective update of all the stresses and is returned to LS-DYNA. The stress in each individual constituent is also stored for the purpose of the incremental update and so that the stress is known for failure. The total stress for the bulk matrix and the matrix portion of the interphase is calculated in the glass rubber model and are stored as history variables. The stress in the fibre is updated as

$$\sigma_{f(t+1)} = \sigma_{f(t)} + \Delta\sigma_{f(t+1)}. \tag{5.37}$$

A block diagram of the model implementation in a user defined material model subroutine is shown in Figure 5.1. Note also that the method presented herein is a direct method to account for the strain partitioning whereas most tangent or secant methods require iteration to correctly capture the strain partitioning.

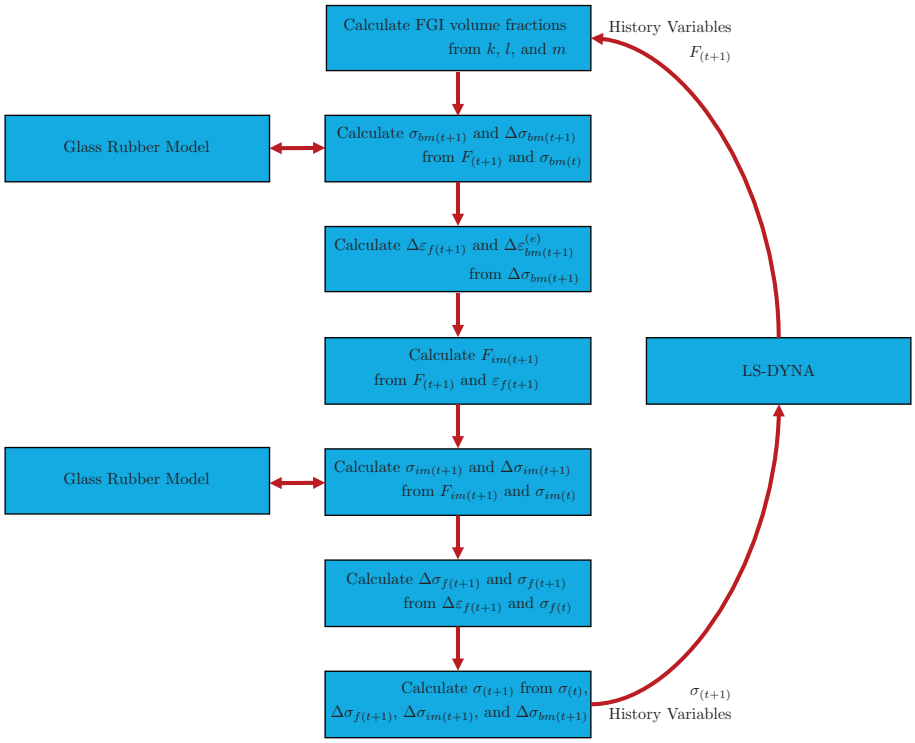

Figure 5.1: Block diagram for the implementation of the framework within a user defined material model in LS-DYNA

5.2 Results

The strain rate sensitive results in Section 4.3.2 are revisited using the same material properties given in Table 4.2. The exact same model setup was used as in Section 4.3.2 and only the axial and transverse compression load cases are considered. The results for transverse compression are shown in Figure 5.2, where the proposed model is presented as a solid line, the previous model is presented as a dashed line, and the experimental data are presented as points. The colours correspond to the three different strain rates as used previously. The proposed framework tends to predict a higher overall stress for a

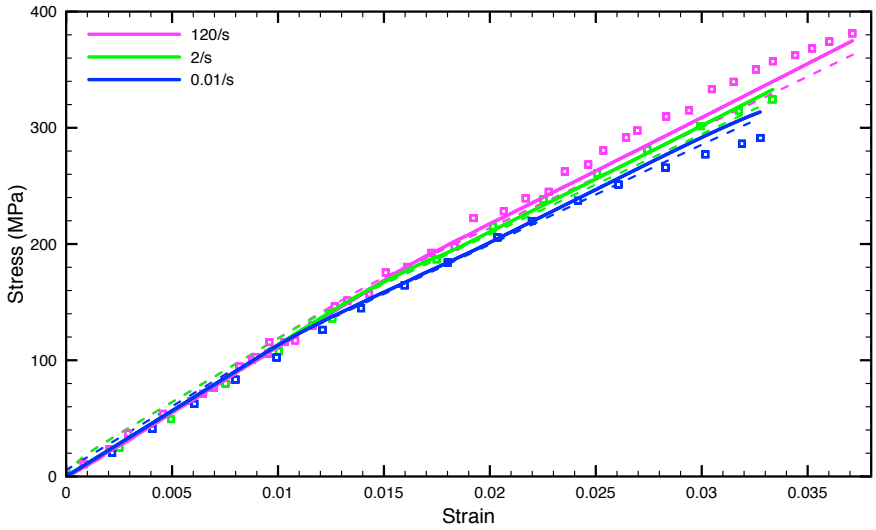

Figure 5.2: Comparison of the results of the proposed framework with the results presented in [149] and the experimental data from [105] for transverse compression

given strain when compared to the previous model for strains above 1%. This is due to increased deformation in the matrix portion of the interphase as the fibre strain is reduced in the transverse direction due to dependence on the elastic strain instead of the overall strain. At strains below 1%, the proposed model offers a better prediction of the stress strain response, as the stress is reduced due to the fibre strains only being related to the elastic bulk matrix strains. Viscous and plastic strains previously had an influence on the fibre strain leading to over prediction even at these low strain values. There is separation of the stress strain response at higher strains due to failure modes, which are not currently accounted for in the model.

A comparison between the error of the previous framework and the current proposed framework is given in Figure 5.3, where the solid lines represents the error of the proposed model and the dashed lines are the previous model error. Both are compared to the experimental data points from Hsiao and Daniel [105]. It is observed that the error is

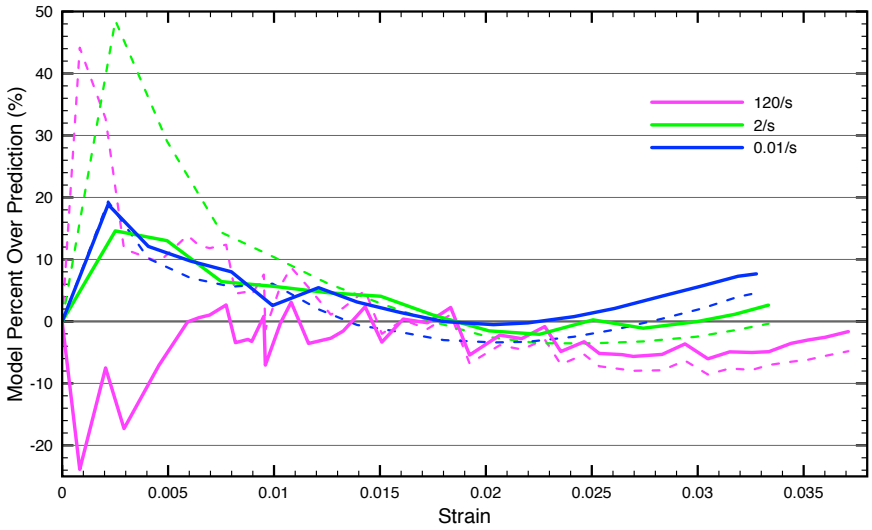

Figure 5.3: Error comparison between the proposed framework and the results presented in [149] with the experimental data from [105] for transverse compression

significantly reduced for the proposed framework for most of the transverse stress strain curves. There is a very large reduction in error at strains below 1%; the error in this portion of the stress strain curve is more prominent as small changes in stress cause a much larger change in percent error than they do at higher strains. For the 0.01/s strain rate, the proposed framework over-predicts the stress at higher strains, which is due to failure modes not accounted for in the model. Analysis is conducted on the average absolute error produced by the results presented in Figure 5.3 shown in Table 5.1. The average absolute error is calculated as

$$\bar{e} = \sqrt{\frac{\sum_{i=1}^{u} e_i^2}{u}} \tag{5.38}$$

where u is the number of data points and e_i is the percentage error calculated at each data point. On average, there is an 32% reduction in the average absolute error by using the proposed model as compared to the previous model. There is a large improvement for the higher two strain rates. If only the higher two strain rates are considered there is a 54% reduction in the error by using the proposed model.

Table 5.1: Error comparison over the strain range for transverse compression

Strain Rate	120/s	2/s	0.01/s
Absolute error proposed (%)	5.83	5.84	6.97
Absolute error from previous model (%)	10.79	15.51	6.16

For the axial direction, four strain rates were simulated and compared to the results presented in Section 4.3.2 and the experimental data from Hsiao and Daniel [105]. The axial results are shown in Figure 5.4. It appears that the previous model where the overall

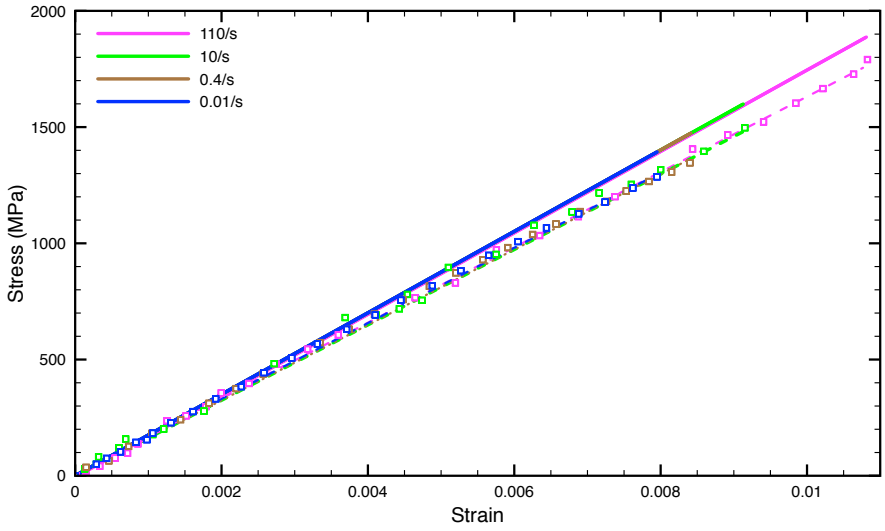

Figure 5.4: Comparison of the results of the proposed framework with the results presented in [149] and the experimental data from [105] for axial compression

strain is used to predict the fibre strain is more accurate, however this is not the case. The proposed model has a more accurate prediction up to 0.4% strain where linear elastic deformation occurs. The current model does not account for failure modes, which would occur such as fibre microbuckling or fibre rotation as the fibres are compressed along their primary axis. The previous model results given in Section 4.3.2 under-predicts the axial compression and intersects with the experimental results at higher strains. A comparison of the error is also conducted for the axial compression direction shown in Figure 5.5. Again, there are larger fluctuations in the error at low strains due to small differences in stress result in larger error percentage. It is observed that the error for the proposed framework is lower than the error for the previous framework up to 0.4% strain. Above

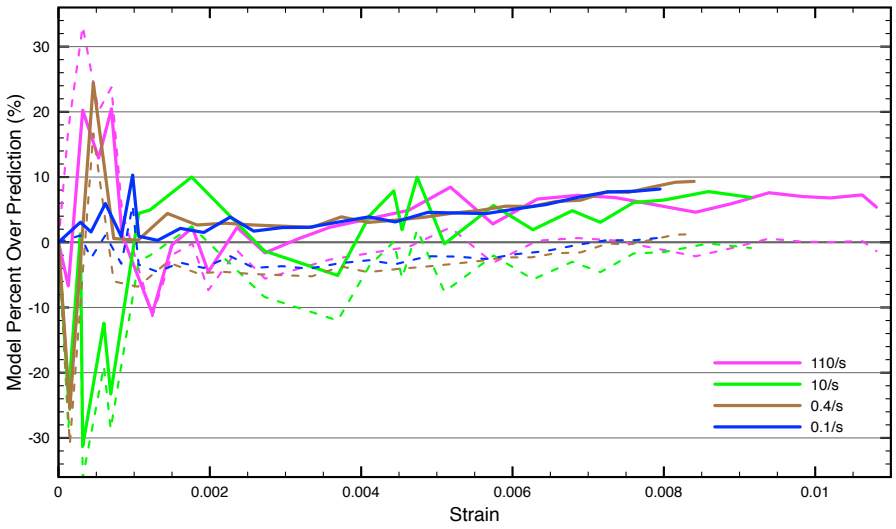

Figure 5.5: Error comparison between the proposed framework and the results presented in [149] with the experimental data from [105] for axial compression

Table 5.2: Error comparison for strains up to 0.4% under axial compression

Strain Rate	110/s	10/s	0.4/s	0.01/s
Absolute error proposed (%)	9.26	14.8	10.91	3.65
Absolute error from previous model (%)	13.70	18.00	11.44	3.34

this strain the proposed framework over-predicts the stress whereas the previous framework eventually meets the experimental results. For strains up to 0.4% the average of absolute error for the data points is given in Table 5.2 There is an improvement of 11.4% in the prediction of the elastic response of the proposed framework over the range of strain rates. However, if the entire strain range is considered, the proposed framework has on average 11.5% more error over all of the strain rates. The comparison over the entire strain range is given in Table 5.3. If the error at the lowest strain rate is removed, the averages for error reduction becomes 18.3% in the elastic range and 6.7% over the entire strain range

Table 5.3: Error comparison over the strain range for axial compression

Strain Rate	110/s	10/s	0.4/s	0.01/s
Absolute error proposed (%)	8.02	10.90	8.70	4.72
Absolute error from previous model (%)	9.92	12.48	7.80	2.84

so, there is improved predictions over the entire strain range if we ignore the lowest strain rate in the axial direction. Therefore, the proposed framework offers a better prediction of the elastic response for axial compression and improved predictive capabilities for the higher strain rates.

5.3 Discussion

Previously it was assumed that the axial direction followed a linear response and the model was calibrated to have the same stress value at the end of the stress strain curve. Therefore, the previous model under-predicts the response up until the point of intersection. Using the same parameters, the proposed framework predicts a stiffer stress strain response and it is still linearly dominated by the fibre stiffness. The increase in overall strain is attributed to plasticity in the matrix, resulting in less strain being transferred transversely to the fibres through Poisson's effects and a resulting increase of deformation and stress in the interphase. The curvature in the experimental results in the axial direction is attributed to fibre buckling and possible onset of other failure modes. As the experiment was a compression test the chances of bending of the specimen are high due to the buckling failure mode. It is unknown if Hsiao and Daniel used strain gauges on both sides of their specimens to detect bending [105].

This framework provides a direct approach to the strain partitioning in long fibre composite materials and the strain localization tensor Eq. 2.4 is constant since the tensors $\mathbb{L}_m$ and $\mathbb{L}_f$ are constant. In linearization techniques using either tangent or secant methods to linearize the deformation and assuming that the fibre is elastic, the effective matrix elastic tensor $\mathbb{L}^*_{m(t+1)}$ would change for each time step in the explicit dynamic time integration scheme. Therefore, in order to calculate the strain localization tensor, the effective bulk matrix elastic tensor would need to be calculated and inverted at each time step adding to the model complexity and computation time required. The strain partitioning procedure used herein avoids this complication reducing the computational time that would be required.

The initial viscous strain within the matrix material in the transverse direction does not contribute to the fibre strain. As a result, the stress strain response predicted by the model is reduced. The stress for a given strain in a later time step is increased, and leads to an over-prediction of the stress strain results at higher strain. Failure is not included in the model, which would result in the reduction of effective stiffness towards the end of the stress strain curve.

5.4 Conclusion

It is proposed that for elastic fibres, the strain in the fibre is related to only the elastic strain in the matrix material. The elastic strain is defined as the strain that is recovered by unloading the material to zero stress in the bulk matrix. The incremental framework to implement this theory in the previously proposed stress based FGI model for implementation in an explicit dynamic finite element code is shown. The framework is implemented and the model's predictions are compared to the previously proposed FGI model where the fibre strains are related to the overall strain and experimental data.

The proposed framework increases the predictive accuracy of the FGI framework reducing the average error by 32% for transverse compression and 11.4% for the prediction of the elastic axial response. For higher strain rates, there is a 54% reduction in average error in the transverse direction; an 18.3% improvement in the elastic prediction in the axial direction and a 6.7% improvement in the response over the entire strain range. Therefore, it is concluded that for fibres, which exhibit elastic material response, the strains in the fibre arise due to the elastic strains occurring in the surrounding matrix material.

5.5 Summary of Model Limitations

The limitations of this model are:

- It is limited to fibre volume fractions of 0.77 from the square packing
- The fibre is assumed to undergo no rotations
- The total strain is limited to approximately 20% due to the assumptions regarding the fibre strain, the theory breaks down after this point
- The interphase matrix volume fraction must be a positive non-zero quantity
- The model does not account for failure

Chapter 6

Incorporating Fibre Orientation in the FGI Framework

Up to this point the FGI model has been developed for composites where all the fibres are aligned within a unit cell. This can be used to model a layup through having one unit cell per layer with a unique orientation compared to the neighbouring plies. For the automotive composites of interest such as DLFT and SMC there is no laminate structure. An image of the fibre location in an SMC material is given in Figure 6.1. Most of the fibres

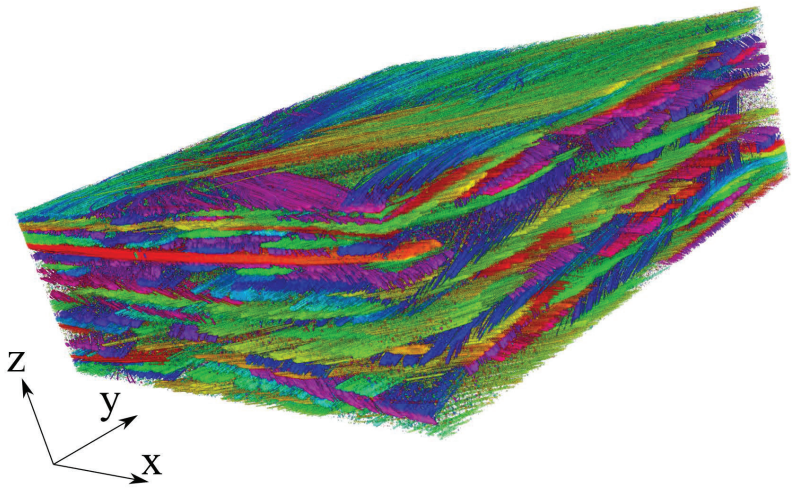

Figure 6.1: Three-dimensional representation of fibre structure in SMC material [151]

lie in the X Y plane, however the layers are not distinct and do not have a unique fibre orientation. There is also visible fibre bridging in the Z direction between fibre bundles.

The complex microstructure of SMC composites must be considered in order to eventually be able to predict the failure of these materials due to micro-scale phenomena. The orientation and location of fibres within a SMC material need to be included in the model.

The fibre orientation was analysed at 3 locations on a 457.2 mm by 254 mm plaque of SMC material with a thickness of approximately 3 mm. The sample locations are shown in Figure 6.2. The exact charge placement for the plaque is unknown however it was observed

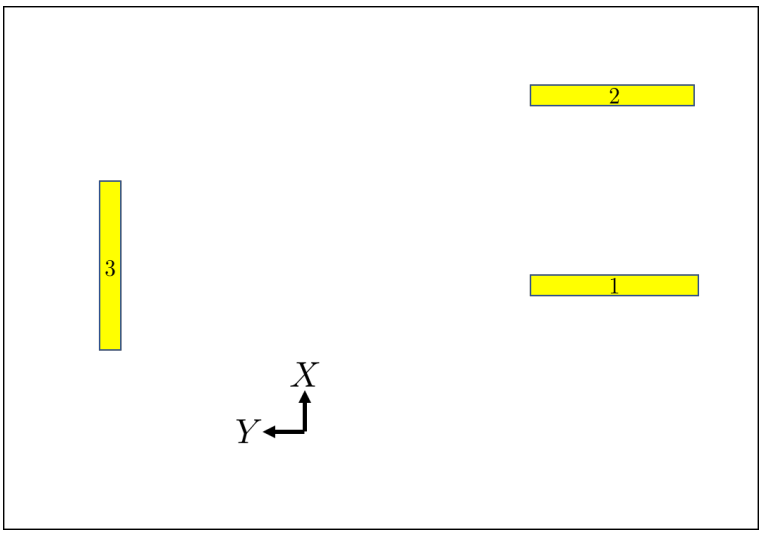

Figure 6.2: Sample locations for CT scans with the coordinate system used [151]

that there was flow in the forming due to visible swirls and weld marks in the corners. A weld in compression moulded material is where two flow fronts come in contact with each other leading to a resin rich area without fibres crossing it.

6.1 Model Formulation

Instead of a single representative fibre within the unit cell, a finite number of representative fibres with unique orientations are used in the model. These representative fibres are assumed to be independent of each other i.e. their deformation is not affected by the presence of other fibres. The representative fibres span the unit cell. The orientation of the representative fibres is given by the algorithm introduced by Leopardi for discretizing a

sphere into regions of equal surface area with a surface normal vector at their center [123]. The orientations are described in terms of the angles θ and ϕ as per Advani and Tucker [16].

6.1.1 Functionally Graded Interphase

A functionally graded interphase surrounds each of the representative fibres and a quartic interphase function is used to describe the stress as a function of radius of the specific representative fibre as

$$\begin{aligned}\sigma(r) =& \frac{1}{\left((l-k)r_{f(i)}\right)^4}\Bigg[(\sigma_f-\sigma_{bm})\Bigg((16m-8)\,r^4-\left(32mlr_{f(i)}+32mkr_{fi}-18lr_{f(i)}-14kr_{f(i)}\right)r^3+\\ &\left(16m(lr_{f(i)})^2+64mlkr_{f(i)}^2+16m(kr_{f(i)})^2-11(lr_{f(i)})^2-32klr_{f(i)}^2-5(kr_{f(i)})^2\right)r^2-\\ &\left(32l^2kr_{f(i)}^3+32mk^2lr_{f(i)}^3-22l^2kr_{f(i)}^3-10lk^2r_{f(i)}^3\right)r+16ml^2k^2r_{f(i)}^4\Bigg)+\\ &\sigma_f\left((lr_{f(i)})^4-4l^3kr_{f(i)}^4-5l^2k^2r_{f(i)}^4\right)+\sigma_{bm}\left(11k^2l^2r_{f(i)}^4-4k^3lr_{f(i)}^4+(kr_{f(i)})^4\right)\Bigg]\end{aligned} \tag{6.1}$$

where $r_{f(i)}$ is the radius of the specific representative fibre. This radius is given in terms of the area fraction of the specific orientation as

$$r_{f(i)} = \sqrt{\frac{4A_{f(i)}}{\pi}} \tag{6.2}$$

where the specific fibre area fraction $A_{f(i)}$ is equivalent to orientation specific fibre volume content $V_{f(i)}$. The orientation specific volume fractions sum over the number of orientations is equivalent to the overall fibre volume content of the region of interest

$$V_f = \sum_{i=1}^{n} V_{f(i)} \tag{6.3}$$

where n is the number of fibre orientations considered. The orientation specific fibre volume fraction is determined from analyzing the CT scan data.

The model is subdivided into three regions for each representative fibre with associated volume fractions as was done for the case of a single unidirectional fibre. The volume fraction of the representative fibre is calculated using the interphase parameters as

$$V_{rf(i)} = V_{f(i)}\left(\frac{16m(l^2-k^2)+l^2+12kl+17k^2}{30}\right). \tag{6.4}$$

Each representative fibre has an associated interphase matrix portion which has a volume fraction of

$$V_{im(i)} = V_{f(i)} \left(\frac{29l^2 - 16m(l^2 - k^2) - 12kl - 17k^2}{30} \right). \tag{6.5}$$

The remainder of the material deforms as the applied deformation to the unit cell.

Advani and Tucker define the fibre being aligned with the local Z axis of the of the coordinate system [16] the fibre is defined as being aligned with the x_1 axis of the unit cell in the FGI framework. A rotation of $\pi/2$ about the Y axis is completed to rotate the angles defined about the Z axis in the definition by Advani and Tucker to the x_1 axis of the local fibre coordinates in the unit cell. The fibre orientation is then defined as a rotation of ϕ about the X axis of the unit cell followed by a rotation of θ about the x_2 axis of the unit cell. The description of fibre orientation within the unit cell is shown in Figure 6.3. The

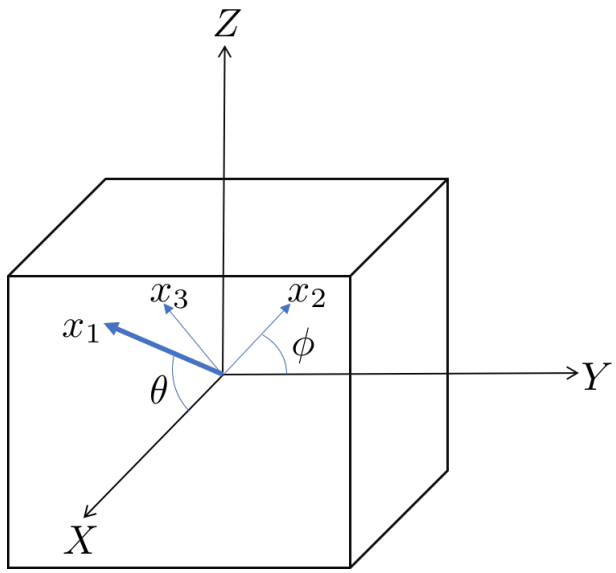

Figure 6.3: Definition of the fibre orientation for a representative fibre in terms of θ and ϕ [151]

coordinate transformation tensor $\mathbf{Q}$ is used to rotate from the global coordinate system to the local representative fibre orientation and is given as

$$\mathbf{Q}_{(i)} = \begin{bmatrix} -\cos\phi_{(i)}\sin\theta_{(i)} & \sin\phi_{(i)} & \cos\phi_{(i)}\cos\theta_{(i)} \\ \sin\phi_{(i)}\sin\theta_{(i)} & \cos\phi_{(i)} & -\sin\phi_{(i)}\cos\theta_{(i)} \\ -\cos\theta_{(i)} & 0 & -\sin\theta_{(i)} \end{bmatrix}. \tag{6.6}$$

Note that each representative fibre has a unique transformation tensor hence the subscript of $_{(i)}$ on the angles.

The strain localization tensor used to calculate the fibre strain given in Eq. 2.4 is defined with the fibre aligned to the x_1 axis through the Eshelby tensor given in Eq. 4.22. The fibre strain must be calculated with the reference frame where the fibre is aligned with the x_1 axis of the coordinate system. Therefore, the fibre strain calculation must be completed for each of the representative fibre orientations considered. The first step in the strain localization calculation is to project the overall applied strain to the unit cell in the local representative fibres coordinate system which as before is equivalent to the bulk matrix strain. This is given as

$$\epsilon_{bm(i)} = \mathbf{Q}_{(i)}^T \varepsilon_{bm} \mathbf{Q}_{(i)}. \tag{6.7}$$

The representative fibre strain is then calculated as

$$\epsilon_{rf(i)} = \mathbb{T} \epsilon_{bm(i)} \tag{6.8}$$

The representative fibre strain is then rotated back to the unit cell coordinate system using the transformation

$$\varepsilon_{rf(i)} = \mathbf{Q}_{(i)} \epsilon_{rf(i)} \mathbf{Q}_{(i)}^T. \tag{6.9}$$

The fibre stress and interphase matrix deformation are calculated in the unit cell coordinate system to make calculations easier.

The displacement gradient for the specific fibre orientation is equivalent to the specific representative fibre strain

$$\mathbf{G}_{rf(i)} = \varepsilon_{rf(i)} \tag{6.10}$$

The displacement gradient of the interphase matrix portion associated with the specific representative fibre is

$$\mathbf{G}_{im(i)} = \frac{\mathbf{G}\left(V_{rf(i)} + V_{im(i)}\right) - V_{rf(i)} \mathbf{G}_{rf(i)}}{V_{im(i)}}. \tag{6.11}$$

The interphase matrix strain is calculated using Green's definition of strain from the deformation gradient as

$$\varepsilon_{im(i)} = \frac{1}{2}\left(\mathbf{F}_{im(i)} \mathbf{F}_{im(i)}^T - \mathbf{I}\right) \tag{6.12}$$

where the relationship between the displacement gradient and deformation gradient is given in Eq. 4.36.

For every fibre orientation considered, the deformation of the representative fibre and associated interphase matrix must be calculated. Therefore, increasing the number of orientations considered will significantly affect the number of calculations that must be completed within the model. To make the model more efficient, the minimum number of orientations required to accurately predict the stress is desired.

The SMC of interest is a polystyrene matrix reinforced with glass fibres and is filled with an unknown quantity of hollow glass spheres to reduce the density along with calcium carbonate filler material. This material is used in production vehicles in applications such as body panels and closures. The filled resin is treated as one material collectively known as the matrix. Isotropic elasticity of the matrix material is assumed when comparing the model to experimental results. The stress is calculated for each representative fibre as

$$\sigma_{rf(i)} = \mathbb{L}_f \varepsilon_{rf(i)}. \tag{6.13}$$

The stress in each associated interphase matrix is calculated as

$$\sigma_{im(i)} = \mathbb{L}_m \varepsilon_{im(i)}. \tag{6.14}$$

The stress in the bulk matrix material is calculated as

$$\sigma_{bm} = \mathbb{L}_m \varepsilon \tag{6.15}$$

The overall stress is calculated by volumetrically averaging each of the fibre and associated interphase matrix portion stresses with the bulk matrix stress and is calculated as

$$\sigma = \left(1 - \sum_{i+1}^{n} \left(V_{rf(i)} + V_{im(i)}\right)\right) \sigma_{bm} + \sum_{i+1}^{n} \left(V_{rf(i)}\sigma_{rf(i)} + V_{im(i)}\sigma_{im(i)}\right). \tag{6.16}$$

This stress is equivalent to the average stress over a region of interest.

6.1.2 Mori Tanaka Implementation

The Mori-Tanaka model was also implemented for comparison of the material model predictions. In the Mori Tanaka scheme the pseudo grain is split into two regions (the fibre and matrix) instead of the three used with the FGI model. The Mori Tanaka model modifies Eshelby's strain localization tensor to include the effects of fibre volume content as

$$\mathbb{T}_{(i)} = \left[\left(1 - V_{f(i)}\right) \mathbb{S}_f \mathbb{L}_m^{-} 1 \left(\mathbb{L}_f - \mathbb{L}_m\right) + \mathbb{I}\right]^{-1}. \tag{6.17}$$

The strain in the representative fibre is calculated in a coordinate system aligned with the specific fibre orientation. As the Voigt assumption is made regarding the strain in each pseudo grain, the strain in the representative fibre for each grain is

$$\epsilon_{rf(i)} = \mathbb{T}_{(i)}\epsilon_{(i)}. \tag{6.18}$$

Since the strain localization tensor is a function of the orientation specific fibre volume content ($V_{f(i)}$), a new strain localization tensor is calculated and inverted for each pseudo grain. The strain applied is rotated to the representative fibre using the same method as Eq. 6.7, which for the strain applied to the unit cell becomes

$$\epsilon_{(i)} = \mathbf{Q}_{(i)}^{T}\varepsilon\mathbf{Q}_{(i)}. \tag{6.19}$$

The strain in the representative fibre is rotated back to the unit cell coordinate system using Eq. 6.9 to calculate the strain in the associated matrix phase for each pseudo grain. As only small strains are considered, the strain compatibility equation for each pseudo grain is

$$\varepsilon = V_{f(i)}\varepsilon_{rf(i)} + (1 - V_{f(i)})\varepsilon_{m(i)}, \tag{6.20}$$

which is rearranged to solve for the matrix strain in each pseudo grain as

$$\varepsilon_{m(i)} = \frac{\varepsilon - V_{f(i)}\varepsilon_{rf(i)}}{1 - V_{f(i)}}. \tag{6.21}$$

Now that the strains in each of the phases is known, the stress calculations are completed within each pseudo grain. The stress in the representative fibre is the same as the FGI model given in Eq. 6.13. The stress in the associated matrix portion for each pseudo grain is

$$\sigma_{m(i)} = \mathbb{L}_{m}\varepsilon_{m(i)}, \tag{6.22}$$

which assumes that the matrix is an isotropic elastic material. The stresses are volumetrically averaged for all the pseudo grains as

$$\sigma = \sum_{i+1}^{n} \left[V_{f(i)}\sigma_{rf(i)} + V_{f(i)}\big(\frac{1}{V_f} - 1\big)\sigma_{m(i)} \right]. \tag{6.23}$$

6.1.3 Comparison of Models

Both models have the same intent, to homogenize the response of a composite material containing misaligned fibres. The strain localization calculation for each model is based on

Eshelby's method [62], however the modification to account for the fibre volume content is different for the two models. In the Mori Tanaka model the volume fraction calculation is accounted for in the strain localization tensor given in Eq. 6.17, which requires a new strain localization for each pseudo grain with a different fibre volume content. This in turn requires the inversion of the strain localization tensor in Eq. 6.18 for each pseudo grain adding to the computational complexity of the model.

Through the modification to the Mori Tanaka strain localization tensor for fibre volume content there is a reduction in the strain of the fibres compared to Eshelby's method. Thus, more strain occurs in the matrix portion in each pseudo grain using the Mori Tanaka homogenization scheme. In the FGI model the volume fraction is modified as per the volumetric integration of the FGI, reducing the effective fibre volume content from the value of the composite. This modification to the volume fraction has the same effect as the modification to the strain localization tensor for the Mori Tanaka model, however it does not require the calculation and subsequent inversion of a new strain localization tensor for each pseudo grain.

The overall effects of the models are similar, however the FGI model is more computationally efficient than the Mori Tanaka model. The FGI model also allows for calculation of the stress in the interphase of each pseudo grain, whereas the Mori Tanaka model only predicts the stress in the fibre and the associated matrix within each pseudo grain. The FGI model allows for the prediction of the failure of the interphase between the fibres and matrix, which in the future could be used to predict fibre matrix debonding, or matrix micro cracking in the region around the fibre. The calculation of the bulk matrix stress in the FGI model allows for the prediction of microcracking in the bulk matrix region as well. Both models allow for the prediction of fibre failure through the fibre stress and strain states for each pseudo grain.

6.2 Analysis Procedure

The three CT scans were analysed to evaluate the fibre orientation. The CT scans consisted of approximately 500 images through the Z direction of the samples. The images were grouped together to consider the variation of properties throughout the material thickness and to give more data points for comparison. The images were divided into 12 regions across the sample thickness for evaluation. Eighteen numbers of orientations are considered with the number of orientations varied between 3 and 200 orientations over the half sphere given by Leopardi's algorithm [123]. The number of orientations over the half sphere are 3, 4, 9, 13, 21, 26, 38, 47, 60, 71, 87, 101, 119, 136, 156, 176, 198, and 200. These numbers of

orientations were selected as they all contain orientations aligned in the $X\ Y$ plane where most of the fibres are oriented. Other numbers of orientations do not contain orientations aligned in the $X\ Y$ plane which would result in these fibres being represented as having some angle of incline above the $X\ Y$ plane. Examples of the partitioning scheme are given in Figure 6.4

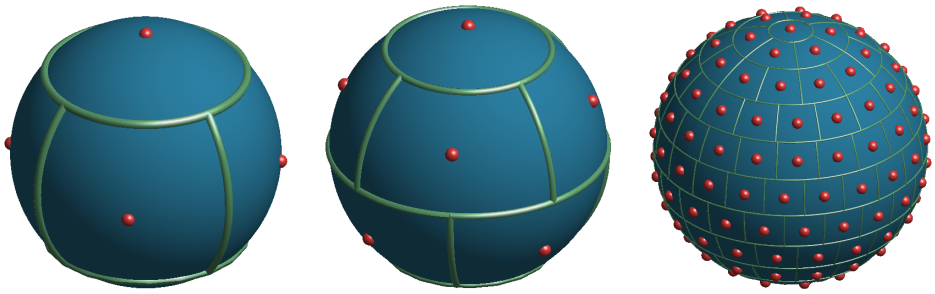

(a) Six Partitions (b) Ten Partions (c) 150 Partitions

Figure 6.4: Partitions of the sphere created with the *MATLAB* tool of Leopardi. Note that six partitions has centre points in the equator plane, ten and 150 partitions do not have centre points in the equator plane [151], the tool works over the entire sphere so the six partitions shown is equivalent to three over the half sphere, ten to five and 150 to 75

Each region in each image was subjected to the same seven deformation paths to compare the stress with different numbers of fibre orientations considered. The deformations were the normal and shear deformations along with in plane biaxial loading. The deformations were applied by a displacement gradient acting on the unit cell model. The displacement gradients applied to the different unit cells are

$$\mathbf{G}_X = \begin{bmatrix} 0.005 & 0 & 0 \\ 0 & 0 & 0 \\ 0 & 0 & 0 \end{bmatrix}, \tag{6.24}$$

$$\mathbf{G}_Y = \begin{bmatrix} 0 & 0 & 0 \\ 0 & 0.005 & 0 \\ 0 & 0 & 0 \end{bmatrix}, \tag{6.25}$$

$$\mathbf{G}_Z = \begin{bmatrix} 0 & 0 & 0 \\ 0 & 0 & 0 \\ 0 & 0 & 0.005 \end{bmatrix}, \tag{6.26}$$

$$\mathbf{G}_{XY} = \begin{bmatrix} 0 & 0.005 & 0 \\ 0.005 & 0 & 0 \\ 0 & 0 & 0 \end{bmatrix}, \tag{6.27}$$

$$\mathbf{G}_{YZ} = \begin{bmatrix} 0 & 0 & 0 \\ 0 & 0 & 0.005 \\ 0 & 0.005 & 0 \end{bmatrix}, \tag{6.28}$$

$$\mathbf{G}_{ZX} = \begin{bmatrix} 0 & 0 & 0.005 \\ 0 & 0 & 0 \\ 0.005 & 0 & 0 \end{bmatrix}, \tag{6.29}$$

$$\mathbf{G}_{Biaxial} = \begin{bmatrix} 0.005 & 0 & 0 \\ 0 & 0.005 & 0 \\ 0 & 0 & 0 \end{bmatrix}. \tag{6.30}$$

The stress state for each of the eighteen number of orientations is calculated for each of the twelve regions through the thickness to compare the results and observe convergence of the stress state. The applied displacement gradients were chosen to be in the elastic deformation regime. The stress predicted by the last 4 number of partitions is averaged and considered to be the converged stress value. The convergence criterion is met if the absolute error of the last 4 number of orientations is less than 10% and the range of error is within 10% for these last four number of orientations which are 156, 176, 198 and 200.

6.3 Model Calibration

As only the fibre properties of the SMC were know, the matrix properties had to be interpolated knowing the macroscopic properties of the SMC material provided by General Motors Canada.

6.3.1 Material Properties

The overall density and weight fraction of the fibres are given as 1.23 g/cm^3 and 0.379 respectively. The material also contains a filler of unknown quantity. To determine the fibre volume fraction, two equations relating the volume fraction to density and the weight fraction to volume fraction and density are required. The rule of mixtures applies for composite materials giving an overall density for a composite (ρ_c) of

$$\rho_c = V_f \rho_f + (1 - V_f)\, \rho_m, \tag{6.31}$$

which is rearranged for the filled matrix material density (ρ_{fm}) as

$$\rho_{fm} = \frac{\rho_c - V_f \rho_f}{1 - V_f}. \tag{6.32}$$

The fibre weight fraction (W_f) is calculated using a burn off test where the weight that remains is the weight of the fibres (w_f). The total weight of a composite is the sum of the weight of the fibre and the weight of the filled matrix (w_{fm}). The fibre weight fraction is calculated as

$$W_f = \frac{w_f}{w_f + w_{fm}} \tag{6.33}$$

The weight of a phase is given by its density and the volume it occupies and gravity (g), therefore Eq. 6.33 is rewritten in terms of the material densities and volume fractions as

$$W_f = \frac{V_f \rho_f g}{V_f \rho_f g + (1 - V_f)\, \rho_{fm} g}, \tag{6.34}$$

which is normalized with respect to gravity to give

$$W_f = \frac{V_f \rho_f}{V_f \rho_f + (1 - V_f)\, \rho_{fm}}. \tag{6.35}$$

Substituting in the filled matrix material density given in Eq. 6.32 and rearranging the equation in terms of volume fraction, the resulting fibre volume fraction is

$$V_f = \frac{W_f \rho_c}{\rho_f}. \tag{6.36}$$

For the material, it is assumed that the fibres are E-glass which has a density of 2.55 g/cm^3. Substituting the known values into Eq. 6.36, the resulting fibre volume fraction is 0.183 for the SMC. The filled matrix material density is calculated using Eq. 6.32, which results in a density of 0.934 g/cm^3 for the filled matrix material.

6.3.2 Model Calibration

A uniaxial load case was used to calibrate the model compared to experimental results for the same material. The model was calibrated using the experimental Young's modulus reported in the experiments performed by General Motors of $7348MPa$, the Poisson's ratio is 0.300. A strain of 0.005 was applied in the x_1 direction while a strain of -0.0015 was applied in the x_2 direction with no strain applied in the x_3 direction. It was found that

Table 6.1: SMC material properties used in the model [151]

Known Properties	Value	Calibrated and Calculated Properties	Value
ρ_c	1.23 g/cm^3	V_f	0.183
ρ_f	2.55 g/cm^3	k	0.83
W_f	0.40	l	1.08
E_f	73 GPa	m	0.4
ν_f	0.25	E_m	4 GPa
E_c	7.35 GPa	ν_m	0.25
ν_c	0.3		

Table 6.2: Calibration stress state

Stress/Modulus	FGI	Mori-Tanaka
σ_X	36.68 MPa	37.88 MPa
σ_Y	2.76 MPa	-9.01 MPa
σ_Z	-0.75 MPa	-17.30 MPa
σ_{XY}	-0.03 MPa	0.05 MPa
σ_{YZ}	-0.04 MPa	0.05 MPa
σ_{ZX}	-0.80 MPa	0.88 MPa
E_x	7.37 GPa	7.58 GPa

adding a strain in the x_3 direction resulted in compressive stresses in the x_3 direction and increased stress in the x_2 direction to an amount that could no longer be considered insignificant for the FGI model. One region through the thickness in sample one was considered for the calibration. The calibrated parameters are given in Table 6.1. The resulting stress state from the calibration is given in Table 6.2. There is a stress induced in the Y direction for the FGI model although the primary deformation is in the X direction, however the stress value is significantly lower than the X direction at around 7.5% of its value. The remaining stresses induced from the FGI model are several orders of magnitude lower and are neglected. For the Mori Tanaka model both the Y and Z stresses have a value and it is compressive the Z component is 45.7% of the X stress component. In order to reduce these stress components for the Mori Tanaka model a through thickness tensile strain is required. This infers that if the material was pulled in one direction the through thickness direction would expand, which violates Poisson's ratio. This arises due to the difference in the strain partitioning between the two methods in that each pseudo grain has a different matrix strain for the Mori Tanaka approach whereas most of the material

comprises of bulk matrix for the FGI approach.

Additional testing was performed on the SMC material resulting in a tensile modulus varying between 7440 MPa and 7040 MPa for a 90% coverage plaque made out of the same material. The initial charge coverage of the material provided for the CT scan analysis is unknown. Orientation analysis was not completed on the material which was used for the additional tensile testing. The additional testing confirmed the tensile properties predicted by the models is within a reasonable range for the material. At this point the exact values are less important, as the purpose of this study is to evaluate the number of pseudo grains required for this material.

6.4 Results

The second order orientation tensors for the three samples have been produced to allow for comparison between the models. The variation in fibre volume content is evaluated by comparing the relative quantity of fibre orientation voxels across the thickness of the CT scans. The stress state predicted by the Mori Tanaka and FGI frameworks are compared for the seven-applied deformation and the stress error is evaluated over the 18 different number of orientations to determine the minimum number of orientations required for a two-step homogenization of the SMC material.

6.4.1 Orientation Analysis

The second order orientation tensor as defined by Advani and Tucker in Eq. 2.5 [16] is calculated for the three samples to ease the interpretation of the stress results. For the first sample the orientation is

$$\mathbf{A} = \begin{bmatrix} 0.5150 & 0.0119 & -0.0038 \\ 0.0119 & 0.4264 & -0.0021 \\ -0.0038 & -0.0021 & 0.0587 \end{bmatrix}.$$

For the second sample the orientation is

$$\mathbf{A} = \begin{bmatrix} 0.5231 & 0.0215 & 0.0006 \\ 0.0215 & 0.4119 & -0.0088 \\ 0.0006 & -0.0088 & 0.0650 \end{bmatrix}.$$

For the third sample the orientation is

$$\mathbf{A} = \begin{bmatrix} 0.4453 & 0.0401 & 0.00181 \\ 0.0401 & 0.4928 & 0.0029 \\ 0.0181 & 0.0029 & 0.0619 \end{bmatrix}.$$

The fibre orientation tensors represent the probability of finding a fibre along a certain direction. As the orientation tensors are symmetric only 6 pieces of data are used to represent the fibre orientation, which would be the third lowest of the number of orientations considered in this analysis. The fibre orientation distribution is used herein to create the fibre orientation histograms for input to the models. The fibre orientation histograms for the selected number of orientations is given in Appendix A.

6.4.2 Volume Fraction Variation

The variation in fibre volume content over the 12 regions is calculated by comparing the number of fibre voxels in the different regions. It is assumed that each of the three samples evaluated contains the average fibre volume fraction of 0.183, the fibre volume content in the 12 regions has to average to this value. The variation of fibre volume content is shown in Figure 6.5. All three samples present the same general trend where the volume fraction

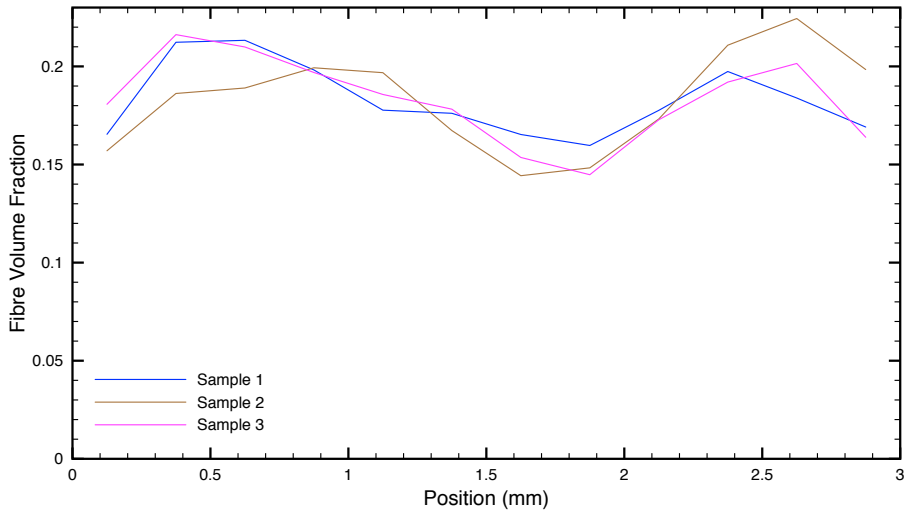

Figure 6.5: Variation of fibre volume content across the sample thickness [151]

is lowest at the edges of the material and in the middle. This indicates that the plaque was moulded using two sheets of the SMC material as the charge. It is expected that this variation in fibre volume content towards the surfaces affects the bending stiffness of the material as the local stiffness of the material at the surface would be reduced.

6.4.3 Stress Results and Error Convergence

The seven applied displacement gradients correspond to the following strain states assuming infinitesimal strains: Biaxial strain $\varepsilon_x = \varepsilon_y = 0.005$, X Strain $\varepsilon_x = 0.005$, Y Strain $\varepsilon_y = 0.005$, Z Strain $\varepsilon_z = 0.005$, XY Strain $\gamma_{xy} = 0.005$, YZ Strain $\gamma_{yz} = 0.005$, and ZX strain $\gamma_{zx} = 0.005$. The other strain components are set to zero. For the 12 regions through the thickness the error is compared for each of the 18 numbers of orientations considered, and the average error, range in error and error standard deviation is calculated for the 12 regions. The stress results for each of the 12 regions is calculated using both the FGI and Mori Tanaka models as the first step in the two-step homogenization taking the volume fraction variation into account. For the error statistics only the values for the stress components, which satisfied the convergence criteria previously defined are plotted. The range of the average error plots has been reduced to ±20% error to show more detail of the error convergence, this excludes some error values for lower number of orientations. Similarly, the range of the error range is truncated at 20% error to show the details of the convergence. The standard deviation plot range is restricted to 4% error, which does not show some of the data points for lower numbers of orientations. The results of the FGI model are given as solid lines and the results of the Mori Tanaka model are given by the dashed lines.

The results of the analysis for the applied biaxial strain is given in Fig. 6.6, the stress as a function of position is given in Fig. 6.6a, the average error is shown in Fig. 6.6b, the error range is given in Fig 6.6c, and the error standard deviation is given in Fig. 6.6d. The X and Y stress component predicted by the Mori Tanaka model is significantly lower than the X and Y stress components predicted by the FGI model. The variation in the X and Y stress components of the Mori Tanaka model also very closely match the shape of the volume fraction variation given in Figure 6.5. The X and Y stress components predicted by the FGI model show much less variation due to fibre volume content. The shape of the Z stress component is the same for the FGI and Mori Tanaka model, however the Mori Tanaka model predicts that this stress component is compressive. The Z stress should be tensile as the plane stress applied prevents contraction in the Z direction, which should occur due to Poisson effects. This difference arises due to each pseudo grain having a different matrix strain in the Mori Tanaka homogenization. The shear stress components for both models are zero as expected. The average stress error is higher for the Mori Tanaka model than the FGI model for the X, Y, Z and XY stress components. The average error for the YZ stress component that converge is the exact same for both the Mori Tanaka and FGI model. One of these YZ stress errors is not in the range of the plot until 119 orientations and starts off at -100% error. The trends in error range and standard deviation

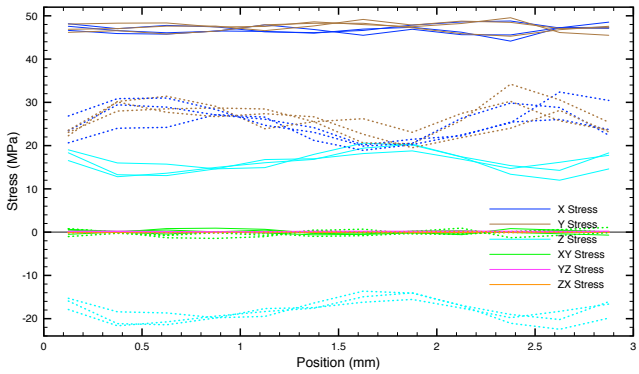

(a) Stress vs. position

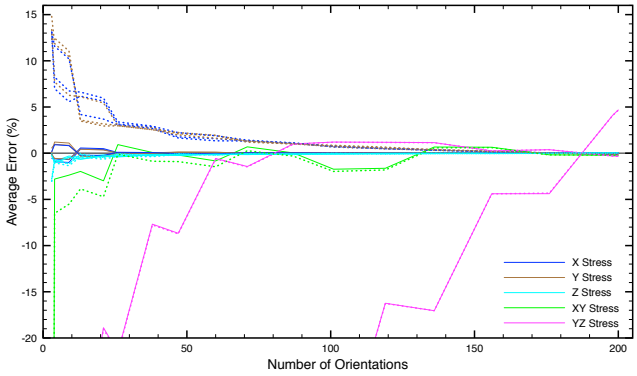

(b) Average Error

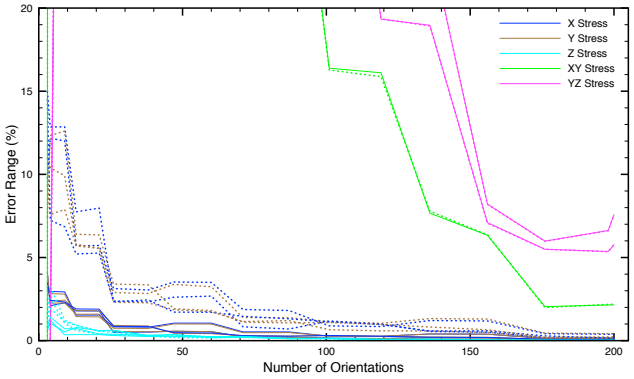

(c) Error Range

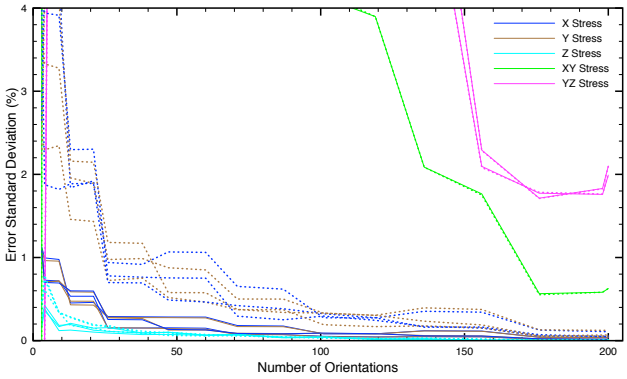

(d) Error Deviation

Figure 6.6: Stress state induced by biaxial strain and the associated stress error statistics [151]

are the same with the FGI model being better for the X, Y and Z stress components while the shear stress components are the same for the two models.

The results of the analysis for the applied X strain is given in Fig. 6.7, the stress as a function of position is given in Fig. 6.7a, the average error is shown in Fig. 6.7b, the error range is given in Fig 6.7c, and the error standard deviation is given in Fig. 6.7d. The X

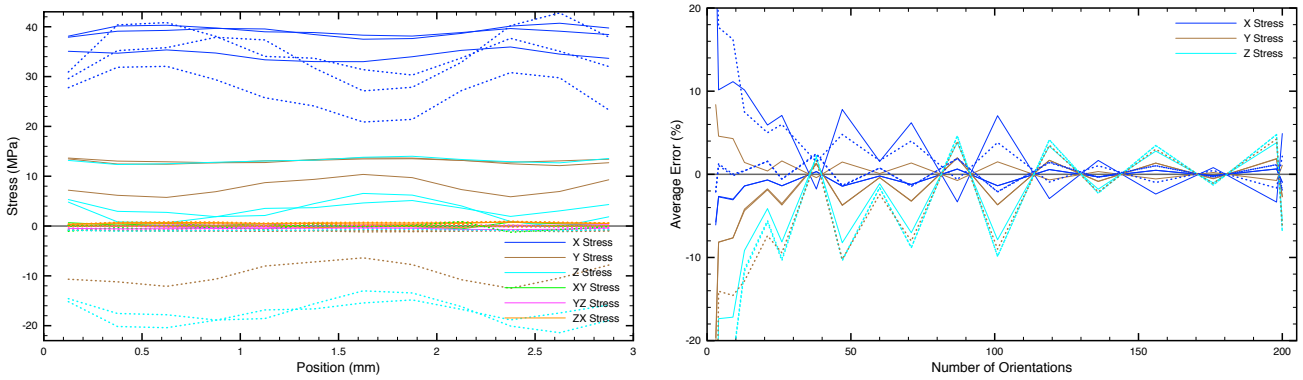

(a) Stress vs. position

(b) Average Error

(c) Error Range

(d) Error Deviation

Figure 6.7: Stress state induced by X strain and the associated stress error statistics [151]

stress results for the Mori Tanaka model are closer to the FGI model than they were for the applied biaxial strain given in Figure 6.6a, however on average the X stress component is still lower for the Mori Tanaka model than it is for the FGI model. The shape of the X stress for the Mori Tanaka model matches the variation in fibre volume content given in Figure 6.5. There is slight variation in the X stress component due to the variation in fibre volume content in the FGI model, but it is definitely less prominent than the Mori Tanaka

model. The Mori Tanaka model predicts that the Y stress for samples one and two and the Z stress component for sample three is zero, however the FGI model predicts that these values are around 14 MPa. This is attributed to the matrix strain being different in each pseudo grain for the Mori Tanaka model. The shape of the Z stress component for samples one and two along with the Y stress component for sample three matches between the FGI and Mori Tanaka models, however the Mori Tanaka model predicts that these stresses are compressive and the FGI model predicts that they are tensile. It makes sense for these stresses to be tensile due to the applied deformation. The average stress for both models show similar trends and in some cases the Mori Tanaka model has lower error in X stress prediction. Less of the stresses converged for the Mori Tanaka model as it predicted those stress components were zero when the FGI model gave a value for three stresses. Two of the Z stresses predicted by the FGI model did not converge as some of their values across the material thickness is close to zero stress. The error range and standard deviation are higher for the Mori Tanaka model than the FGI model for nearly all the stress components and particularly for the X stress, which corresponds to the loading direction.

The results of the analysis for the applied Y strain is given in Fig. 6.8, the stress as a function of position is given in Fig. 6.8a, the average error is shown in Fig. 6.8b, the error range is given in Fig 6.8c, and the error standard deviation is given in Fig. 6.8d. Similarly, to the applied X strain the Y stress component predicted by the Mori Tanaka model is lower on average than the Y stress predicted by the FGI model, but the peak stresses predicted for the Y stress by the Mori Tanaka model are similar to the FGI model. The shape of the Y stress component predicted by the Mori Tanaka model matches the shape of the volume fraction variation given in Figure 6.5. The Y stress is higher for sample three than samples one and two due to the fibre orientation tensor components and preferred fibre orientations. Comparing the X stress values in Figure 6.7a to the Y stress values in Figure 6.8a the X stress is slightly higher in samples one and two than the Y stress in sample three and the Y stress in samples one and two is at a similar level to the X stress in sample three, which indicates the effects of the overall fibre orientation tensor on the stress states. Similarly, to the applied X strain, the Mori Tanaka model predicts that the X stress component for samples one and two and the Z stress for sample three are in compression but the shape is a close match between the Mori Tanaka and FGI models. The FGI model predicts three stresses with a value of approximately 14 MPa, which the Mori Tanaka model predicts as zero stress The Mori Tanaka model results for these stress components do not meet the convergence criteria. The average Y stress error for samples one and two is higher for the Mori Tanaka model than the FGI model. The average error follows similar trends between the two models. The error range and standard deviation for the Mori Tanaka model is larger than it is for the FGI model especially for fewer numbers

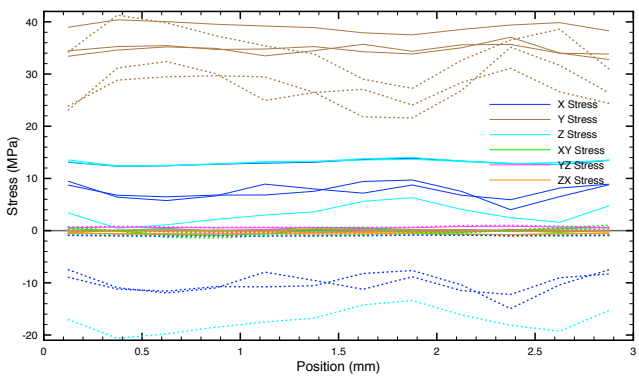

(a) Stress vs. position

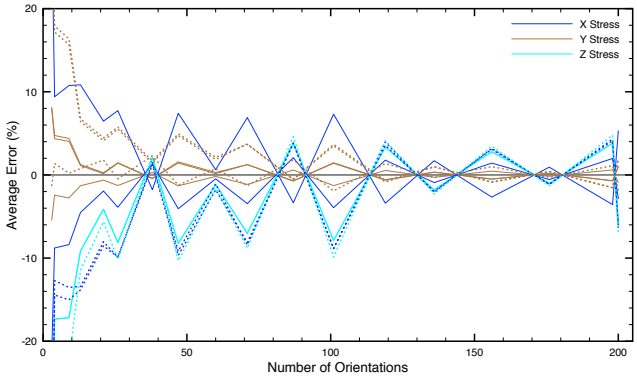

(b) Average Error

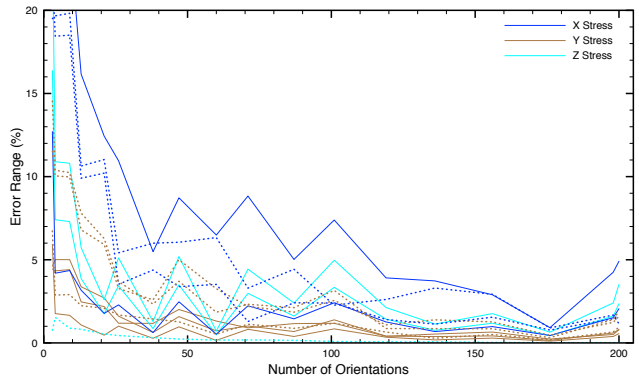

(c) Error Range

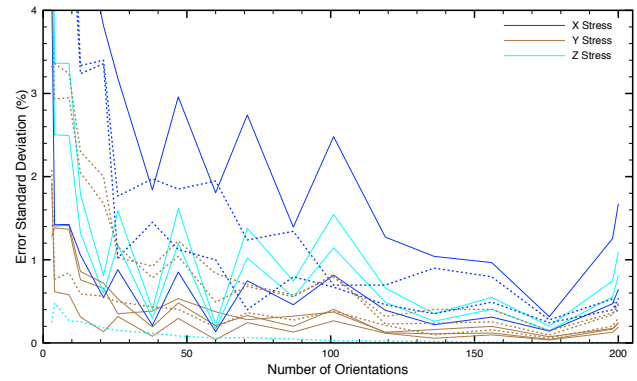

(d) Error Deviation

Figure 6.8: Stress state induced by Y strain and the associated stress error statistics [151]

of orientations.

The results of the analysis for the applied Z strain is given in Fig. 6.9, the stress as a function of position is given in Fig. 6.9a, the average error is shown in Fig. 6.9b, the error range is given in Fig 6.9c, and the error standard deviation is given in Fig. 6.9d. All

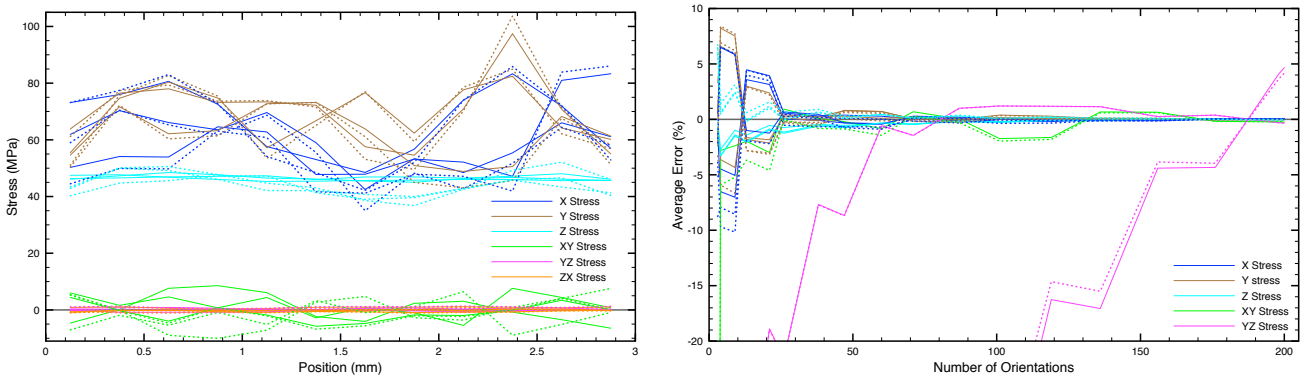

(a) Stress vs. position

(b) Average Error

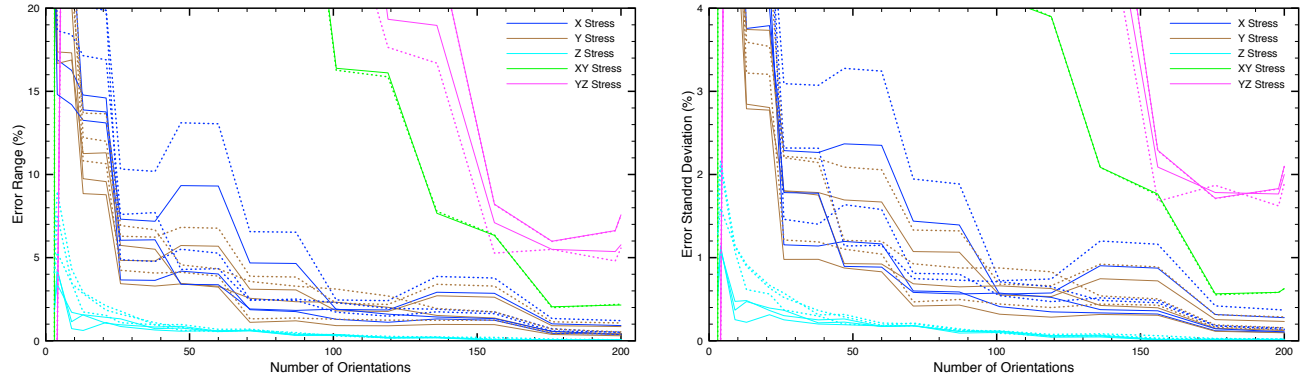

(c) Error Range

(d) Error Deviation

Figure 6.9: Stress state induced by Z strain and the associated stress error statistics [151]

the stress components for the applied Z strain match between the FGI and Mori Tanaka model. The X and Y stresses are higher than the Z stress due to the quantity of fibres in these directions. Both the Mori Tanaka and FGI models predict that the X and Y stress components are in tension, which is correct for the applied strain. The Z stress component predicted by the Mori Tanaka model has slightly more variation across the samples thickness compared to the FGI model, and the shape is similar to the volume fraction variation given in Figure 6.5. The other stress components do not vary with

the fibre volume content as much as the stress in the direction of the applied strain. The average error in stress prediction by the two models is very similar and no clear conclusions are drawn. The stress error range and standard deviation indicate that the Mori Tanaka model has a larger range in stress error and larger deviation of the error over the 12 regions compared to the FGI model.

The results of the analysis for the applied XY strain is given in Fig. 6.10, the stress as a function of position is given in Fig. 6.10a, the average error is shown in Fig. 6.10b, the error range is given in Fig 6.10c, and the error standard deviation is given in Fig. 6.10d. The XY stress predicted by the Mori Tanaka model is again lower on average than the

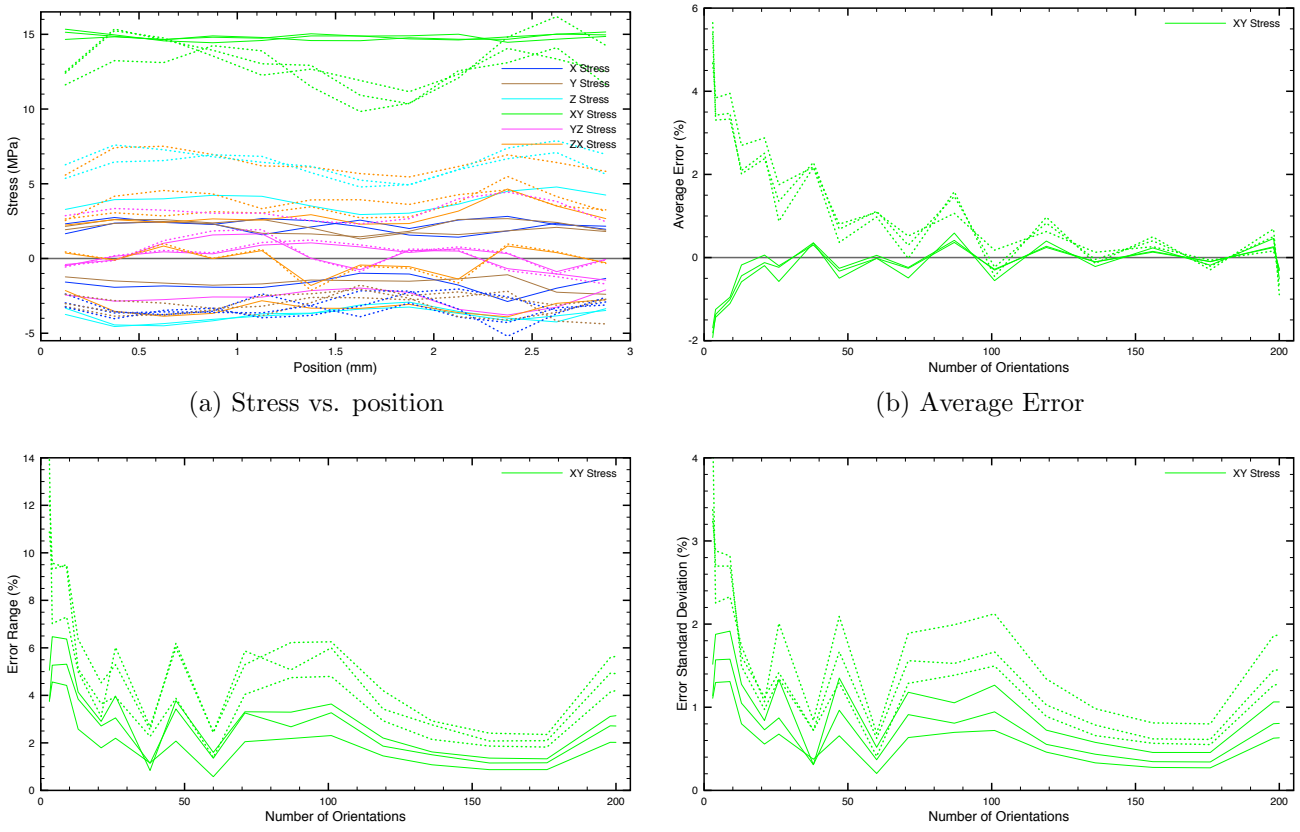

(a) Stress vs. position

(b) Average Error

(c) Error Range

(d) Error Deviation

Figure 6.10: Stress state induced by XY strain and the associated stress error statistics [151]

FGI model and there is more variation in the Mori Tanaka results as a function of the fibre

volume content. The remainder of the stress components should be around zero for the applied strain, however they are all very noisy and below a magnitude of 5 MPa for the FGI model. The magnitudes of these stress components are higher for the Mori Tanaka model with some peaking at around 8 MPa. The magnitude of the average stress error is higher for the Mori Tanaka model than it is for the FGI model. The error range and standard deviation is also larger for the Mori Tanaka models than for the FGI model. For the applied XY strain only the XY stress component satisfies the convergence criteria for both the FGI and Mori Tanaka models.

The results of the analysis for the applied YZ strain is given in Fig. 6.11, the stress as a function of position is given in Fig. 6.11a, the average error is shown in Fig. 6.11b, the error range is given in Fig 6.11c, and the error standard deviation is given in Fig. 6.11d. The YZ stress predicted by the Mori Tanaka model tends to be lower than the FGI model. The Mori Tanaka model again shows more dependence on the fibre volume fraction than the FGI model. Like the applied XY strain, the other stress components should be zero however they are noisy with magnitudes of around 5 MPa with the stress values for the Mori Tanaka model being higher than those of the FGI model. Only the YZ stress component converges in samples one and two. In sample three the YZ, Z, and ZX stress components converge for both models. The average error is higher for the Mori Tanaka model for the YZ stress component. For samples one and two the stress error oscillates about the 0% axis. This is attributed to there being a negative probability of having fibres aligned with the YZ direction in samples one and two. for sample three the error range and standard deviation is higher for the Mori Tanaka model than the FGI model, however no conclusions can be drawn for samples one and two with regards to the error range and standard deviation.

The results of the analysis for the applied ZX strain is given in Fig. 6.12, the stress as a function of position is given in Fig. 6.12a, the average error is shown in Fig. 6.12b, the error range is given in Fig 6.12c, and the error standard deviation is given in Fig. 6.12d. The stresses predicted for the ZX strain are similar to those predicted by the applied YZ strain. Again, there is variation in the ZX stress predicted by the Mori Tanaka model due to the variation in fibre volume content. The other stress components are noisy, but should be zero. The magnitude of the other stress components is higher for the Mori Tanaka model than the FGI model. The ZX stress converges in all the samples and the YZ and Z stress component for samples one and two converges. The values of the YZ and Z stress that converge are more consistent across the sample thickness than the other stress components. The average error for the Mori Tanaka model is higher for the ZX stress component while the average error for the other stress components is similar between the two models. The error range and standard deviation for samples one and two are greater for the Mori Tanaka

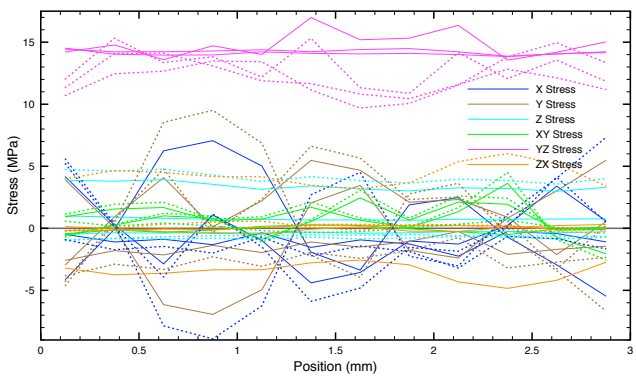

(a) Stress vs. position

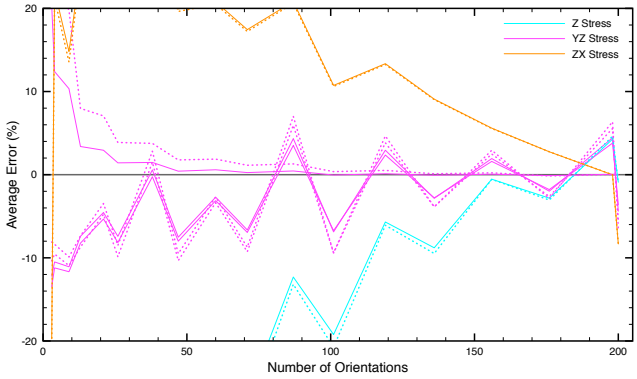

(b) Average Error

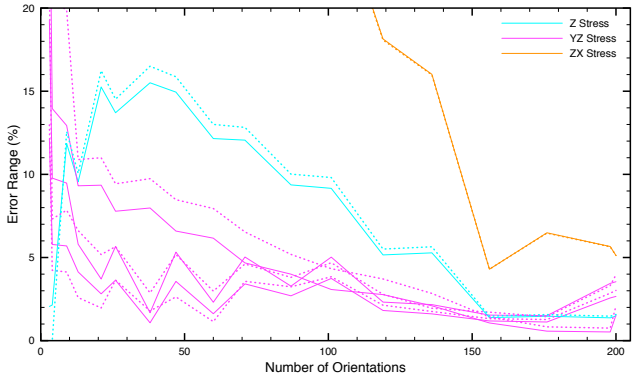

(c) Error Range

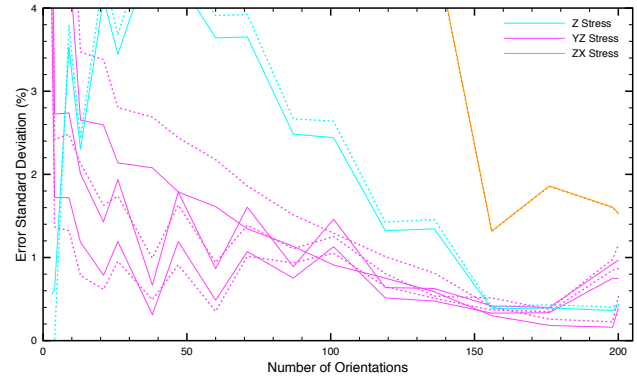

(d) Error Deviation

Figure 6.11: Stress state induced by YZ strain and the associated stress error statistics [151]

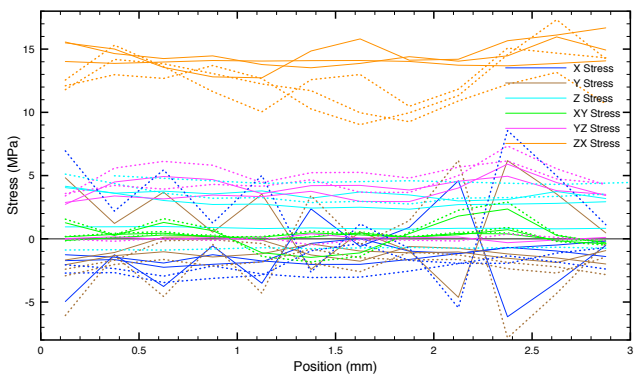

(a) Stress vs. position

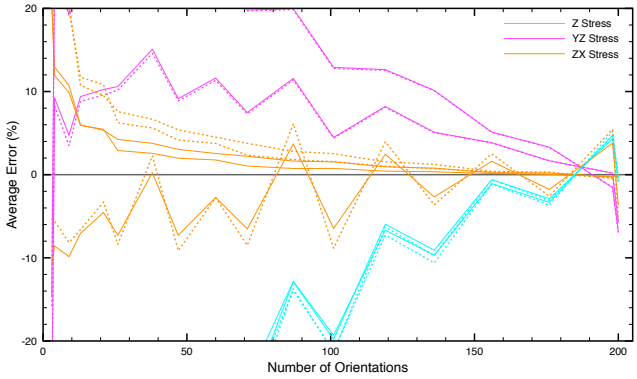

(b) Average Error

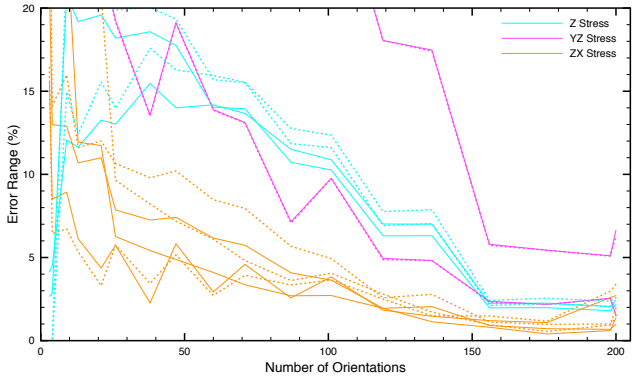

(c) Error Range

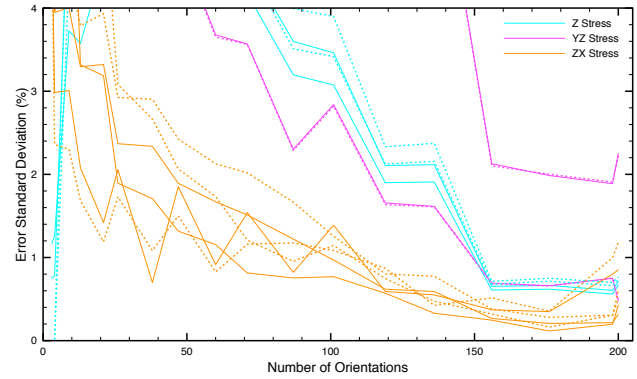

(d) Error Deviation

Figure 6.12: Stress state induced by ZX strain and the associated stress error statistics [151]

Table 6.3: Comparing the percentage that 38 or 60 fibre orientations reduced the error statistics [151]

Model	Average Error		Error Range		Error Deviation	
Number of Orientations	38	60	38	60	38	60
FGI	22.6	77.4	30.2	69.8	15.1	84.9
MT	23.5	76.5	19.6	80.4	5.9	94.1

model compared to the FGI model except for the YZ stress component.

Some general observations are made regarding the stress and stress errors for the seven applied strains:

- The variation of stress as a function of position in the direction of the applied strain depends heavily on the fibre volume content for the Mori Tanaka model
- The stress always converges in the direction of the applied strain
- If the stress component is always above 5 MPa the stress is likely to converge for the FGI model

The first minima in the stress error statistics tend to occur at 38 and 60 orientations. The percentage of occurrences that 38 versus 60 orientations provides lower error statistics is compared for all the converged stress components for both the FGI and Mori Tanaka models and is given in Table 6.3. For both the Mori Tanaka and FGI model more often the predictions with 60 orientations is more accurate than the prediction with 38 orientations. Choosing 60 orientations should be considered in future modelling efforts.

6.4.4 Effect of Fibre Volume Fraction Variation

For each of the 12 regions over the samples thickness the Von Mises equivalent stress resulting from the 6 stress components is calculated. It is found that there tends to be a linear relationship between the fibre volume fraction and the Von Mises equivalent stress. Linear regression is completed to verify this, using the equation form

$$\sigma_{eq} = aV_f + b \tag{6.37}$$

the values for a, b and the r^2 value for the models, for each applied strain is given in Table 6.4. There is a very good linear fit for the equivalent stress for the applied biaxial strain

Table 6.4: Equation 6.37 constants for both models for each sample and r^2 value of the fit

Strain	Sample	FGI			Mori Tanaka		
		a	b	r^2	a	b	r^2
Biaxial	1	96.486	13.262	0.994	257.14	-3.116	0.996
	2	98.861	12.738	0.997	259.56	-3.819	0.998
	3	93.898	13.675	0.998	251.93	-2.363	0.999
X	1	104.82	12.94	0.994	265.64	-2.424	0.997
	2	103.7	13.081	0.999	265.14	-2.540	0.999
	3	101.55	13.511	0.999	261.36	-1.764	0.999
Y	1	59.698	13.852	0.423	191.9	-1.215	0.727
	2	46.899	16.421	0.328	172.14	2.672	0.699
	3	71.342	11.343	0.564	213.16	-5.826	0.805
Z	1	204.48	-12.821	0.290	224.28	-13.514	0.192
	2	321.83	-33.487	0.572	326.97	-30.655	0.455
	3	229.11	-18.114	0.487	170.35	-4.988	0.226
XY	1	6.232	25.903	0.114	128.16	2.019	0.970
	2	16.491	23.72	0.681	146.51	-1.736	0.989
	3	5.268	25.808	0.151	129.83	1.246	0.978
YZ	1	1.827	25.115	0.001	124.52	0.133	0.644
	2	-14.133	27.854	0.467	96.35	4.738	0.903
	3	4.259	24.173	0.021	133.21	-2.285	0.837
ZX	1	-20.359	30.62	0.035	94.457	7.475	0.343
	2	26.985	21.449	0.269	150.66	-3.507	0.882
	3	-29.016	32.162	0.152	85.109	9.021	0.518

and applied X strain for both models. The Mori Tanaka model has a better linear fit for the other strain components where the FGI model has a weak correlation for the applied shear strains. Both models have porer correlation in the Z direction with the FGI model being slightly better than the Mori Tanaka model. In the Y strain the linear fit is slightly worse than the X strain. This is attributed to there being fewer fibres in the Y direction in samples one and two. Comparing the b value for strains where there is a strong linear correlation, it is noted that for the Mori Tanaka model they are on average -2.671 MPa and for the FGI model they are positive 13.2 MPa on average. This indicates that if the fibre volume fraction was reduced to zero the equivalent stress for the Mori Tanaka model would be negative where the FGI model would be positive which is expected due to the matrix properties. Thus, the Mori Tanaka model has too much dependence on the fibre volume content for predicting the stress state. The FGI model behaves as one would expect in this respect.

6.5 Discussion

The two homogenization schemes studied have similar results for the SMC samples considered. The volume fraction dependence of the predicted stress is greater in the Mori Tanaka model than it is in the FGI model. Using the Voigt assumption for the second homogenization step results in some non-physical compressive stresses predicted by the Mori Tanaka model. Therefore, a different second homogenization may be appropriate for the Mori Tanaka model with dependence on the fibre orientation. The FGI model does not have this issue as it is assumed that the strain in the bulk matrix is the same for every pseudo grain through the use of the interphase matrix portion of the interphase.

Ogierman and Kokot claim that 9 pseudo grains are required to recreate the fourth order orientation tensor and stiffness tensors [135]. The ratio of the stiffness of the matrix to the inclusion material used by Ogierman and Kokot is only 6.28 times as stiff [135]. Doghri and Tinel have discussed that a higher ratio of stiffness will affect the results of a homogenization as the direction of the inclusions will have a greater effect on the overall stiffness [57]. The ratio of the stiffness of the matrix and the fibres of the SMC studied is 18.25, which is roughly 3 times the ratio used by Ogierman and Kokot. A larger ratio of stiffness between the matrix and fibres requires a larger number of orientations in the model.

Doghri and Tinel have shown that the number of pseudo grains has an effect on the yield point of an elastic plastic material system, and that thousands of pseudo grains were required to match the plastic behaviour [57]. Doghri and Tinel use a closure approximation to predict the fibre orientation distribution from an assumed random inclusion orientation. They did not report a large variation in the elastic properties with the number of orientations considered [57]. The measured fibre orientation distribution from CT scans are used herein to evaluate the number of pseudo grains required so that the variation due to the number of pseudo grains in the plastic behaviour is not observed due to only considering the elastic response.

The fibre volume content also has an effect on the homogenized material response as demonstrated in the comparison of the equivalent stresses. The fibre volume content studied is approximately twice that of Doghri and Tinel or Ogierman and Kokot [57, 135]. It is expected that as the fibre volume content increases, the level of anisotropy produced by the fibre orientation also increases. The effect of fibre volume fraction on modelling results has been discussed in section 6.4.4 above.

The shape of the inclusion affects the Eshelby tensor and by extension the strain localization tensor for the material pairing. The fibre studied is assumed to be infinitely

long and aligned with the x_1 axis of the pseudo grain. This means that the strain in the fibre along the x_1 axis of the pseudo grain is the same as the strain applied to the unit cell in the x_1 direction of the pseudo grain. If the fibre does not span the unit cell, less strain along this x_1 direction would be transferred to the fibre. In the work of Doghri and Tinel a fibre aspect ratio of 20 was used [57]. In Ogierman and Kokot a fibre aspect ratio of 10 was used [135]. The smaller fibre aspect ratios reduce the amount of fibre strain in the x_1 direction of the pseudo grains, which reduces the anisotropy of the pseudo grains. Therefore, additional pseudo grains should be required as the fibre aspect ratio increases such as the case for long fibres.

The orientation distribution functions used by Doghri and Tinel and Ogierman and Kokot are both found using a closure approximation from the fibre orientation tensors [57, 135]. The closure approximation gives a mathematical relationship between the quantity of fibres at a specific orientation and the fibre orientation tensor. Using a closure approximation always allows for a calculated number of fibres within each pseudo grain. The measured fibre orientation distribution is used herein and the orientation of each fibre voxel must be assigned to one of the pseudo grain orientations. Increasing the number of pseudo grains also increases the number of boundaries between pseudo grains and can make it more difficult to assign fibre voxels to an orientation. There are also limitations on the precision of the prediction of the voxel orientation, which leads to increased error with higher number of orientations considered. This could explain why the error was observed to be larger for 198 and 200 orientations versus 156 and 176 orientations. As the number of boundaries increases, the accuracy of the fibre orientation prediction for a voxel becomes problematic due to conflicts between the boundaries.

6.6 Conclusions

Sixty orientations are sufficient to predict the elastic response of an SMC material using a two-step homogenization procedure with the Mori Tanaka and FGI models. The Mori Tanaka model has more dependence on the fibre volume content than the FGI model and it has been shown that this dependence may be too large based on the equivalent stress states. CT scan data determining fibre orientation distribution in 12 regions through the material thickness on three samples were used to evaluate the stress state convergence of the models to end up with sixty orientations.

The stress predicted by the FGI converges faster than the Mori Tanaka model. The error range and standard deviation of the FGI model also tends to be lower than the Mori Tanaka model. Additionally, the FGI model is more computationally efficient than the

Mori Tanaka model due to the strain localization tensor being constant for each orientation. The shear stress components require more orientations to converge than the normal stress components. For the FGI model as long as the stress component is above 5 MPa it is likely to converge. The stress component in the strain direction is also likely to converge. The following factors affect the number of orientations required for a composite system: fibre aspect ratio, fibre volume content, the difference in stiffness between the fibre and matrix material, and fibre orientation.

6.7 Summary of Model Limitations

The limitations of the model are:

- Limited to the elastic response
- Plastic response and failure is not considered in the number of orientation evaluation
- Limited to 0.77 fibre volume fraction due to square packing, but realistic boundaries may be lower since the model neglects fibre-fibre interactions
- Fibres are considered to be continuous across the boundaries of the unit cell, and of infinite length for modelling purposes, since they are much longer than the unit cell size. In the SMC material used for model comparisons, the fibres have a length of 25 mm. The assumption is valid as long as the unit cell is smaller than the fibre length
- Voigt strain assumption for each pseudo grain is made, however there may be some issues with the validity of this assumption especially for the two-phase Mori Tanaka model
- Fibre curvature is not directly taken into account in the model formulation but can be calibrated using the interphase parameters

Chapter 7

Conclusions

In this thesis, a new micromechanics based model for composite materials with a polymer matrix and elastic fibres has been developed. These materials are of interest to the automotive industry as they have very high specific strength and stiffness compared to other engineering materials. The light-weighting of vehicles is crucial to the improvement of vehicle fuel economy and reduced environmental impact of the automotive industry. Materials such as SMC and DLFT allow for production cycle times and part cost to be acceptable for use in mass production vehicles. They offer reduced mass, increased formability, and corrosion resistance as compared to traditional metallic materials. DLFT materials are also recyclable at end of life. Additional challenges exist with these materials such as the changes to the matrix material over time due to environmental degradation and the prediction of the location of the reinforcements within a formed compression moulded part.

The microstructure of the finished part is crucial to its mechanical performance. The complexity of the microstructure of compression moulded parts must be properly accounted for when attempting to mathematically model their behaviour. The theory has been well developed for dealing with laminated composite structures such as those used for decades in the aerospace industry and in luxury automobiles. These structures are two dimensional in nature and have well established layers of composite material with known fibre orientations. Compression moulded composites on the other hand, are usually three dimensional structures and the fibre orientation within the finished parts is unknown. The size of automotive composite parts is large compared to size of the reinforcing fibres and a homogenization technique is necessary to account for the effects at the micro-scale, which control the material response.

Before dealing with the complexity of the microstructure for compression moulded

parts, the three-dimensional response of polymer matrix composites containing aligned fibres needs to be understood. In Chapter 3, the elastic response of a composite with aligned fibres is developed. It is assumed that the material properties close to the representative fibre change radially as a function of position, creating the FGI. It is assumed that the fibre and matrix materials undergo the same deformations and the fibre is transversely isotropic, allowing for the reduction in stiffness under loading perpendicular to the fibres. Using the FGI there is an effective reduction in the fibre volume fraction allowing the model to predict lower than the upper bound on the elastic properties of the Voigt assumption, which is used. The stress in the fibre and matrix are predicted separately and then combined. This will allow for the future use of these stresses in failure prediction. This model is shown to offer improvements over the method of cells model which is commonly used for micromechanics predictions. Due to the volumetric assumption of the interphase, the quantity of interphase material is independent of the fibre size allowing any number of aligned fibres to be represented as a single representative fibre.

The FGI model is extended to predict the situation where the matrix material is deforming plastically in Chapter 4. It is assumed that instead of the material properties changing as a function of position around the fibre, the stress changes as a function of position. The previous assumption that the material properties change as a function of position is a subset of the new assumption that stress changes as a function of position. A third region is introduced as the strain partitioning between the fibre and bulk matrix material is assumed to follow Eshelby's solution, the additional strain to bridge the difference occurs in the interphase matrix portion. An advanced polymer material model (glass rubber constitutive model) is used to capture the plasticity and strain rate effects of the polymer matrix material using the materials thermodynamic properties where temperature and viscous effects can be captured. The stress in the three regions can be used to capture the onset of failure in the matrix, fibre, and interphase. The model is able to capture the response up until the onset of failure modes in axial and transverse compression as well as shear. The strain rate dependent response is evident in the transverse compression where the matrix response is dominant.

The FGI model is extended to account for strain partitioning when the matrix is deforming irreversibly in Chapter 5. It was previously assumed that the strain in the fibre is related to the overall strain applied to the unit cell. The assumption is now changed to the fibre strain being related to the elastic strain in the bulk matrix material. It is shown that this assumption improves the prediction of the transverse response of the material greatly, while being more computationally efficient than other homogenization schemes which involve the calculation of a tangent or secant modulus.

The fibre orientation is incorporated into the FGI model in Chapter 6, through the

use of a two-stage homogenization scheme. Before the model can be implemented in LS-DYNA for routine use in industrial applications, the number of unique orientations required to accurately reproduce the stress strain response of the material is required. As each orientation requires the calculation and storage of 12 additional stress terms in addition to the 6 of the bulk matrix material, the minimum number of orientations is desirable. The microstructure of an SMC plaque was evaluated at three locations and the model containing the microstructure data was subjected to a series of strain states to predict the resulting stress state. The fibre orientations were assigned to unique representative fibre orientations over the half sphere where 18 different number of orientations were considered ranging from 3 up to 200 representative fibre orientations. It was found that 60 orientations over the half sphere are required to accurately capture the response of the SMC composite for the calibrated material properties, fibre volume content, and inclusion shape. The results of the FGI model are compared to the two-step Mori Tanaka model and it is found that the FGI model allows for more accuracy with fewer orientations and increased computational efficiency compared to the Mori Tanaka model.

Overall, a three-dimensional homogenization scheme has been developed for composite materials that works in all loading directions. Both elasticity and the plastic response of the composite are captured through the stress based FGI. The model has been designed to incorporate failure by allowing the user access to the stress and strain states of each constituent of the composite material. The model is designed with computational efficiency in mind. Only one strain localization tensor is required for all the representative fibres, and a single representative fibre represents all fibres aligned in a given direction. This also results in size independence of the model allowing for larger element sizes in finite element simulations. Finally, the models have been developed to be implemented in LS-DYNA. Thus, all the goals outlined in the introduction have been achieved. It has been shown that the response of a long fibre reinforced composite material can be modeled considering a unit cell containing a finite number of representative fibres at specific orientations using the material properties of the fibre and matrix and accounting for the mechanical interaction between them using a functionally graded interphase.

7.1 Future Work

The three CT scanned samples used in Chapter 6 were subjected to three-point bending up to the point of failure. Once the model is implemented in LS-DYNA, the macroscopic response of the three-point bend tests will be correlated to a finite element model containing the fibre orientation and fibre volume fraction variation in a finite number of layers of

element over the material thickness.

The failure modes including fibre failure, fibre buckling, matrix cracking, and fibre matrix debonding need to be incorporated into the modeling framework. As discussed, the FGI model predicts the homogenized stress and strain in the fibre, bulk matrix and interphase matrix regions allowing for the implementation of failure theories which have been developed for unidirectional composite materials. Additional complications arise from the compression moulding process, such as fibre curvature, fibre end effects, and fibre bundle effects. These will also have to be accounted for in the model.

A coupled manufacturing and solid mechanics model is required for these compression moulded materials since the final material properties are a function of the re-orientation of the fibres during the manufacturing process. Codes exist to predict the orientation tensor for short rigid fibre composites and how they flow during moulding, however these cannot account for high aspect ratio fibres which exhibit curvature post manufacturing. Closure approximations to work with the 60 orientations from either a second or fourth order fibre orientation tensor would be required before this additional predictive ability could be incorporated.

7.2 Summary of Limitations

The model is restricted to a fibre volume content of 77%. This is not a limitation in practice, since composite materials cannot be manufactured with such a high fibre content due to issues with wetability of the fibres. For the compression moulding composites of interest for the automotive industry, the bulk material typically has a maximum fibre content of approximately 30%.

The fibre is assumed to undergo no rotations, which is not an issue for solid mechanics simulations, however this would become a problem for manufacturing simulations. The limitation on the fibre strain is also not a limitation since fibre failure would occur before large strains for the classes of fibres considered.

The interphase quantity must be positive and non-zero. This does not cause problems as long as the interphase zone exists. The whole model breaks down if this condition is not.

Failure is not accounted for currently, but there are plans for the implementation of failure as discussed throughout and in the future work section.

The fibre end effects of an SMC are not accounted for but could be added in the future.

References

[1] J. Aboudi. Generalized effective stiffness theory for the modeling of fiber-reinforced composites. *International Journal of Solids and Structures*, 17:1005–1018, 1981.

[2] J. Aboudi. A continuum theory for fiber-reinforced elastic-viscoplastic composites. *International Journal of Engineering Science*, 20:605–621, 1982.

[3] J. Aboudi. The effective moduli of short-fiber composites. *International Journal of Solids and Structures*, 19:693–707, 1983.

[4] J. Aboudi. Effective thermoelastic constants of short-fiber composites. *Fibre Science and Technology*, 20:211–225, 1984.

[5] J. Aboudi. Damage in composites - modeling of imperfect bonding. *Composites Science and Technology*, 28:103–128, 1987.

[6] J. Aboudi. Micromechanical analysis of the strength of unidirectional fiber composites. *Composites Science and Technology*, 33:79–96, 1988.

[7] J. Aboudi. Micromechanical analysis of composites by method of cells. *Applied Mechanics Reviews*, 42(7):193–221, 1989.

[8] J. Aboudi. Micromechanics prediction of fatigue failure of composite materials. *Journal of Reinforced Plastics and Composites*, 8:150–166, 1989.

[9] J. Aboudi. Micromechanical characterization of the non-linear viscoelastic behavior of resin matrix composites. *Composites Science and Technology*, 38:371–386, 1990.

[10] J. Aboudi, S.M. Arnold, and B.A. Bednarcyk. *Micromechanics of Composite Materials*. Butterworth-Heinemann, Oxford, 2013.

[11] J. Aboudi and Y. Benveniste. An average theory for the dynamic behaviour of a laminated elastic-viscoplastic medium under general loading. *International Journal of Solids and Structures*, 17:69–81, 1981.

[12] J.D. Achenbach and H. Zhu. Effect of interfacial zone on mechanical behavior and failure of fiber-reinforced composites. *Journal of the Mechanics and Physics of Solids*, 37(3):381–393, 1989.

[13] D.F. Adams and D.A. Crane. Combined loading micromechanical analysis of a unidirectional composite. *Composites*, 15(3):181–192, 1984.

[14] D.F. Adams and D.R. Doner. Longitudinal shear loading of a unidirectional composite. *Journal of Composite Materials*, 1:4–17, 1967.

[15] D.F. Adams and D.R. Doner. Transverse normal loading of a unidirectional composite. *Journal of Composite Materials*, 1:152–164, 1967.

[16] S.G. Advani and C.L. Tucker III. The use of tensors to describe and predict fiber orientation in short fibre composites. *Journal of Rheology*, 31:751–784, 1987.

[17] E.M. Arruda and M.C. Boyce. A three-dimensional constitutive model for the large stretch behavior of rubber elastic materials. *Journal of the Mechanics and Physics of Solids*, 41:389–412, 1993.

[18] L.E. Asp, L.A. Berglund, and P. Gudmundson. Effects of a composite-like stress state on the fracture of epoxies. *Composites Science and Technology*, 53:27–37, 1995.

[19] L.E. Asp, L.A. Berglund, and R. Talreja. A criterion for crack initiation in glassy polymers subjected to a composite-like stress state. *Composites Science and Technology*, 56:1291–1301, 1996.

[20] L.E. Asp, L.A. Berglund, and R. Talreja. Prediction of matrix-initiated transverse failure in polymer composites. *Composites Science and Technology*, 56:1089–1097, 1996.

[21] V.D. Azzi and S.W. Tsai. Anisotropic strength of composites. *Experimental Mechanics*, 5(9):283–288, 1965.

[22] B. Bar-On and H.D. Wagner. Effective moduli of multi-scale composites. *Composites Science and Technology*, 72:566–573, 2012.

[23] B.A. Bednarcyk, J. Aboudi, and S.M. Arnold. Micromechanics of composite materials governed by vector constitutive laws. *International Journal of Solids and Structures*, 110-111:137–151, 2017.

[24] Y. Benveniste. The effective mechanical behaviour of composite materials with imperfect contact between the constituents. *Mechanics of Materials*, 4:197–208, 1985.

[25] Y. Benveniste. A new approach to the application of Mori-Tanaka's theory in composite materials. *Mechanics of Materials*, 6:147–157, 1987.

[26] Y. Benveniste and J. Aboudi. Crack propagation in a laminated composite material modeled by a two-dimensional mixture theory. *Acta Mechanica*, 29:213–227, 1978.

[27] Y. Benveniste and J. Aboudi. A continuum model for fiber reinforced materials with debonding. *International Journal of Solids and Structures*, 20:935–951, 1984.

[28] Y. Benveniste, G.J. Dvorak, and T. Chen. Stress fields in composites with coated inclusions. *Mechanics of Materials*, 7:305–317, 1989.

[29] Y. Benveniste and T. Miloh. Imperfect soft and stiff interfaces in two-dimensional elasticity. *Mechanics of Materials*, 33:309–323, 2001.

[30] V. Birman and L.W. Byrd. Modeling and analysis of functionally graded materials and structure. *Applied Mechanics Reviews*, 60:195–216, 2007.

[31] J. Boudet, F. Auslender, M. Bornert, and Y. Lapusta. An incremental variational formulation for the prediction of the effective work-hardening behavior and field statistics of elasto-(visco)plastic composites. *International Journal of Solids and Structures*, 83:90–113, 2014.

[32] M.C. Boyce, D.M. Parks, and A.S. Argon. Large inelastic deformation of glassy polymers. Part I: Rate dependent constitutive model. *Mechanics of Materials*, 7:15–33, 1988.

[33] M.C. Boyce, G.G. Weber, and D.M. Parks. On the kinematics of finite strain plasticity. *Journal of the Mechanics and Physics of Solids*, 37:647–665, 1989.

[34] L. Brassart, L. Stainier, I. Doghri, and L. Delannay. Homogenization of elasto-(visco) plastic composites based on an incremental variational principle. *International Journal of Plasticity*, 36:86–112, 2012.

[35] C.P. Buckley, P.J. Dooling, J. Harding, and C. Ruiz. Deformation of thermosetting resins at impact rates of strain. Part 2: Constitutive model with rejuvenation. *Journal of the Mechanics and Physics of Solids*, 52:2355–2377, 2004.

[36] C.P. Buckley, J. Harding, J.P. Hou, C. Ruiz, and A. Trojanowski. Deformation of thermosetting resins at impact rates of strain. Part 1: Experimental study. *Journal of the Mechanics and Physics of Solids*, 49:1517–1538, 2001.

[37] C.P. Buckley and D.C. Jones. Glass-rubber constitutive model for amorphous polymers near the glass transition. *Polymer*, 36(17):3301–3312, 1995.

[38] C.P. Buckley, D.C. Jones, and D.P. Jones. Hot-drawing of poly(ethylene terephthalate) under biaxial stress: application of a three-dimensional glass-rubber constitutive model. *Polymer*, 37:2403–2414, 1996.

[39] B. Budiansky. Micromechanics. *Computers & Structures*, 16:3–12, 1983.

[40] B. Budiansky and N.A. Fleck. Compressive failure of fibre composites. *Journal of the Mechanics and Physics of Solids*, 41:183–211, 1993.

[41] V.N. Bulsara and R. Talreja amd J. Qu. Damage initiation under transverse loading of unidirectional composites with arbitrarily distributed fibers. *Composites Science and Technology*, 59:673–682, 1999.

[42] B.P. Bussadori, K. Schuffenhauer, and A. Scattina. Modelling of CFRP crushing structures in explicit crash analysis. *Composites: Part B*, 60:725–735, 2014.

[43] J.J. Carruthers, A.P. Kettle, and A.M. Robinson. Energy absorption capability and crashworthiness of composite material structures: A review. *Applied Mechanics Reviews*, 51(10):635–649, 1998.

[44] C.C. Chamis. Simplified composite micromechanics for predicting microstresses. NASA Technical Memorandum 87295, National Aeronautics and Space Administration, 1986.

[45] K.K. Chawla. *Composite Materials Science and Engineering*. Springer, New York, 3 edition, 2012.

[46] X. Chen and Y. Liu. Multiple-cell modeling of fiber-reinforced composites with the presence of interphase using the boundary element method. *Computational Materials Science*, 21:86–94, 2001.

[47] M. Cherkaoui, H. Sabar, and M. Berveiller. Elastic behavior of composites with coated inclusions: Micromechanical approach and applications. *Composites Science and Technology*, 56:877–882, 1996.

[48] R.M. Christensen. Viscoelastic properties of heterogeneous media. *Journal of the Mechanics and Physics of Solids*, 17:23–41, 1969.

[49] R.M. Christensen and K.H. Lo. Solution for effective shear properties in three phase sphere and cylinder models. *Journal of the Mechanics and Physics of Solids*, 27:315–330, 1979.

[50] C. Czarnota, K. Kowalczyk-Gajewska, A. Salahouelhadj, M. Martiny, and S. Mercier. Modeling of the cyclic behavior of elastic-viscoplastic composites by the additive tangent Mori-Tanaka approach and validation by finite element calculations. *International Journal of Solids and Structures*, 56-57:96–117, 2015.

[51] P. Dasappa, P. Lee-Sullivan, and X. Xiao. Temperature effects on creep behavior of continuous fiber GMT composites. *Composites: Part A*, 40:1071–1081, 2009.

[52] P. Dasappa, P. Lee-Sullivan, and X. Xiao. Development of viscoplastic strains during creep in continuous fiber GMT composites. *Composites: Part B*, 41:48–57, 2010.

[53] F. Dinzart and H. Sabar. New micromechanical modeling of the elastic behavior of composite materials with ellipsoidal reinforcements and imperfect interfaces. *International Journal of Solids and Structures*, 108:254–262, 2017.

[54] I. Doghri, L. Adam, and N. Bilger. Mean-field homogenization of elasto-viscoplastic composites based on a general incrementally affine linearization method. *International Journal of Plasticity*, 26:219–238, 2010.

[55] I. Doghri, L. Brassart, L. Adam, and J.-S. Gérard. A second-moment incremental formulation for the mean-field homogenization of elasto-plastic composites. *International Journal of Plasticity*, 27:352–371, 2011.

[56] I. Doghri and A. Ouaar. Homogenization of two-phase elasto-plastic composite materials and structures Study of tangent operators, cyclic plasticity and numerical algorithms. *International Journal of Solids and Structures*, 40:1681–1712, 2003.

[57] I. Doghri and L. Tinel. Micromechanics of inelastic composites with misaligned inclusions: Numerical treatment of orientation. *Computer methods in applied mechanics and engineering*, 195:1387–1406, 2006.

[58] H. Dong, J. Wang, and B.L. Karihaloo. An improved Puck's failure theory for fibre-reinforced composite laminates including the in situ strength effect. *Composites Science and Technology*, 98:86–92, 2014.

[59] N.E. Dowling. *Mechanical Behavior of Materials Engineering Methods for Deformation, Fracture, and Fatigue*. Pearson, Upper Saddle River, New Jersey, 4 edition, 2013.

[60] D. Dray, P. Gilormini, and G. Régnier. Comparison of several closure approximations for evaluating the thermoelastic properties of an injection molded short-fiber composite. *Composites Science and Technology*, 67:1601–1610, 2007.

[61] A. Erdelyi. *Higher Transcendental Functions*, volume 1. Robert E. Krieger Publishing Company, Malabar, Florida, 1981.

[62] J.D. Eshelby. The determination of the elastic field of an ellipsoidal inclusion, and related problems. *Proceedings of the Royal Society of London. Series A, Mathematical and Physical Science*, 241(1226):376–396, 1957.

[63] J.D. Eshelby. The elastic field outside an ellipsoidal inclusion. *Proceedings of the Royal Society of London. Series A, Mathematical and Physical Sciences*, 252:561–569, 1959.

[64] Henry Eyring. Viscosity, plasticity, and diffusion as examples of absolute reaction rates. *The Journal of Chemical Physics*, 4:283–291, 1936.

[65] N. Feld, C. Maeyens, B. Delattre, and N. Grandmaison. Modelling the effect of process-induced anisotropy on the constitutive behavior of chopped fiber composites. *Composites: Part A*, 101:334–343, 2017.

[66] P. Feraboli and A. Masini. Development of carbon/epoxy structural components for a high performance vehicle. *Composites: Part B*, 35:323–330, 2004.

[67] L. Figiel and C.P. Buckley. On the modelling of highly elastic flows of amorphous thermoplastics. *International Journal of Non-Linear Mechanics*, 44:389–395, 2009.

[68] N.A. Fleck and P.M. Jelf. Deformation and failure of a carbon fibre composite under combined shear and transverse loading. *Acta Metallurgica et Materialia*, 43:3001–3007, 1995.

[69] N.A. Fleck and J.Y. Shu. Microbuckle initiation in fibre composites: A finite element study. *Journal of the Mechanics and Physics of Solids*, 43:1887–1918, 1995.

[70] S. Fliegener, M. Luke, and P. Gumbsch. 3D microstructure modeling of long fiber reinforced thermoplastics. *Composites Science and Technology*, 104:136–145, 2014.

[71] I.G. Garcia, V. Mantic, and E. Graciani. A model for the prediction of debond onset in spherical-particle-reinforced composites under tension. application of a coupled stress and energy criterion. *Composites Science and Technology*, 106:60–67, 2015.

[72] F. Garesci and S. Fliegener. Young's modulus prediction of long fiber reinforced thermoplastics. *Composites Science and Technology*, 85:142–147, 2013.

[73] E. Ghossein and M. Lévesque. Homogenization models for predicting local filed statistics in ellipsoidal particles reinforced composites: Comparison and validations. *International Journal of Solids and Structures*, 58:91–105, 2015.

[74] R.F. Gibson. A review of recent research on nanoindentation of polymer composites and their constituents. *Composites Science and Technology*, 105:51–65, 2014.

[75] F. Gommer, A. Endruweit, and A.C. Long. Analysis of filament arrangements and generation of statistically equivalent composite micro-structures. *Composites Science and Technology*, 99:45–51, 2014.

[76] J.J. Gu and Q.-C. He. Exact connections between the effective elastic moduli of fibre-reinforced composites with general imperfect interfaces. *International Journal of Solids and Structures*, 104-105:65–72, 2017.

[77] M. Haghighi-Yazdi, J.K.Y. Tang, and P. Lee-Sullivan. Moisture uptake of a polycarbonate blend exposed to hygtothermal aging. *Polymer Degradation and Stability*, 96:1858–1865, 2011.

[78] L.T. Harper, C. Qian, T.A. Turner, S. Li, and N.A. Warrior. Representative volume elements for discontinuous carbon fibre composites - Part 1: Boundary conditions. *Composites Science and Technology*, 72:225–234, 2012.

[79] L.T. Harper, C. Qian, T.A. Turner, S. Li, and N.A. Warrior. Representative volume elements for discontinuous carbon fibre composites - Part 2: Determining the critical size. *Composites Science and Technology*, 72:204–210, 2012.

[80] Z. Hashin. The elastic moduli of heterogeneous materials. *Journal of Applied Mechanics*, 29:143–150, 1962.

[81] Z. Hashin. On elastic behaviour of fibre reinforced materials of arbitrary transverse phase geometry. *Journal of the Mechanics and Physics of Solids*, 13:119–134, 1965.

[82] Z. Hashin. Failure criteria for unidirectional fiber composites. *Journal of Applied Mechanics*, 47:329–334, 1980.

[83] Z. Hashin. Analysis of composite materials - A survey. *Journal of Applied Mechanics*, 50:481–505, 1983.

[84] Z. Hashin. Analysis of cracked laminates: A variational approach. *Mechanics of Materials*, 4:121–136, 1985.

[85] Z. Hashin. Cumulative damage theory for composite materials: Residual life and residual strength methods. *Composites Science and Technology*, 23:1–19, 1985.

[86] Z. Hashin. Analysis of stiffness reduction of cracked cross-ply laminates. *Engineering Fracture Mechanics*, 25:771–778, 1986.

[87] Z. Hashin. The differential scheme and its application to cracked materials. *Journal of the Mechanics and Physics of Solids*, 36:719–734, 1988.

[88] Z. Hashin, D. Bagchi, and B.W. Rosen. Non-linear behavior of fiber composite laminates. NASA Contractor Report CR-2313, National Aeronautics and Space Administration, 1974.

[89] Z. Hashin and B.W. Rosen. The elastic moduli of fiber-reinforced materials. *Journal of Applied Mechanics*, 31:223–232, 1964.

[90] Z. Hashin and A. Rotem. A fatigue failure criterion for fiber reinforced materials. *Journal of Composite Materials*, 7:448–464, 1973.

[91] Z. Hashin and A. Rotem. A cumulative damage theory of fatigue failure. *Materials Science and Engineering*, 34:147–160, 1978.

[92] Z. Hashin and S. Shtrikman. Note on a variational approach to the theory of composite elastic materials. *Journal of the Franklin Institute*, 271:336–341, 1961.

[93] Z. Hashin and S. Shtrikman. A variational approach to the theory of the elastic behaviour of multiphase materials. *Journal of the Mechanics and Physics of Solids*, 11:127–140, 1963.

[94] S. Herasati, L.C. Zhang, and H.H. Ruan. A new method for characterizing the interphase regions of carbon nanotube composites. *International Journal of Solids and Structures*, 51:1781–1791, 2014.

[95] R. Hill. A theory of the yielding and plastic flow of anisotropic metals. *Proceedings of the Royal Society of London. Series A, Mathematical and Physical Sciences*, 193:281–297, 1948.

[96] R. Hill. *The Mathematical Theory of Plasticity*. Oxford University Press, Oxford, 1950.

[97] R. Hill. Elastic properties of reinforced solids: Some theoretical principles. *Journal of the Mechanics and Physics of Solids*, 11:357–372, 1963.

[98] R. Hill. Theory of mechanical properties of fibre-strengthened materials: I. Elastic behaviour. *Journal of the Mechanics and Physics of Solids*, 12:199–212, 1964.

[99] R. Hill. Theory of mechanical properties of fibre-strengthened materials: II. Inelastic behaviour. *Journal of the Mechanics and Physics of Solids*, 12:213–218, 1964.

[100] R. Hill. A self-consistent mechanics of composite materials. *Journal of the Mechanics and Physics of Solids*, 13:213–222, 1965.

[101] R. Hill. Theory of mechanical properties of fibre-strengthened materials: III. Self-consistent model. *Journal of the Mechanics and Physics of Solids*, 13:189–198, 1965.

[102] M.J. Hinton and P.D. Soden. Predicting failure in composite laminates: The background to the exercise. *Composites Science and Technology*, 58:1001–1010, 1998.

[103] O. Hoffman. The Brittle Strength of Orthotropic Materials. *Journal of Composite Materials*, 1:200–206, 1967.

[104] H.M. Hsiao and I.M. Daniel. Nonlinear elastic behavior of unidirectional composites with fiber waviness under compressive loading. *Journal of Engineering Materials and Technology*, 118:561–570, 1996.

[105] H.M. Hsiao and I.M. Daniel. Strain rate behavior of composite materials. *Composites: Part B*, 29B:521–533, 1998.

[106] D. Hull and D.J. Bacon. *Introduction to Dislocations*. Butterworth-Heinemann, Kidlington, Oxford, 5 edition, 2011.

[107] J.M. Hutchinson. Physical aging of polymers. *Progress in Polymer Science*, 20:703–760, 1995.

[108] J.W. Hutchinson and K.W. Neale. Influence of strain-rate sensitivity on necking under uniaxial tension. *Acta Metallurgica*, 25:839–846, 1977.

[109] J.W. Hutchinson and K.W. Neale. Neck propagation. *Journal of the Mechanics and Physics of Solids*, 31:405–426, 1983.

[110] S. Jacques, I. De Baere, and W. Van Paepegem. Application of periodic boundary conditions on multiple part finite element meshes for the meso-scale homogenization of textile fabric composites. *Composites Science and Technology*, 92:41–54, 2014.

[111] M. Jalalvand, G. Czel, and M.R. Wisnom. Numerical modelling of the damage modes in UD thin carbon/glass hybrid laminates. *Composites Science and Technology*, 94:39–47, 2014.

[112] I. Jasiuk and M.W. Kouider. The effect of an inhomogeneous interphase on the elastic constants of transversely isotropic composites. *Mechanics of Materials*, 15:53–63, 1993.

[113] P.M. Jelf and N.A. Fleck. Compression failure mechanisms in unidirectional composites. *Journal of Composite Materials*, 26:2706–2726, 1992.

[114] M. Kant and D. Penumadu. Fracture behavior of individual carbon fibers in tension using nano-fabricated notches. *Composites Science and Technology*, 89:83–88, 2013.

[115] J. Karger-Kocsis, H. Mahmood, and A. Pegoretti. Recent advances in fiber/matrix interphase engineering for polymer composites. *Progress in Materials Science*, 73:1–43, 2015.

[116] J.K. Kim, M.L. Sham, and J. Wu. Nanoscale characterisation of interphase in silane treated glass fibre composites. *Composites: Part A*, 32:607–618, 2001.

[117] T.R. King, D.M. Blackketter, D.E. Walrath, and D.F. Adams. Micromechanics prediction of the shear strength of carbon fiber/epoxy matrix composites: The influence of the matrix and interface strengths. *Journal of Composite Materials*, 26(4):558–573, 1992.

[118] M. Koizumi. FGM activities in japan. *Composites Part B: Engineering*, 28B:1–4, 1997.

[119] V.I. Kushch, S.V. Shmegera, and L. Mishnaevsky. Explicit modeling the progressive interface damage in fibrous composite: Analytical vs. numerical approach. *Composites Science and Technology*, 71:989–997, 2011.

[120] S. Kyriakides, R. Arseculeratne, E.J. Perry, and K.M. Liechti. On the compressive failure of fiber reinforced composites. *International Journal of Solids and Structures*, 32:689–738, 1995.

[121] J. Lambert, A.R. Chambers, I. Sinclair, and S.M. Spearing. 3D damage characterisation and the role of voids in the fatigue of wind turbine blade materials. *Composites Science and Technology*, 72:337–343, 2012.

[122] T.-H. Le, P.J.J. Dumont, L. Orgéas, D. Favier, L. Salvo, and E. Boller. X-ray phase contrast microtomography for the analysis of the fibrous microstructure of SMC composites. *Composites Part A: Applied science and manufacturing*, 39:91–103, 2008.

[123] P. Leopardi. A partition of the unit sphere into regions of equal area and small diameter. *Electronic Transactions on Numerical Analysis*, 25:309–327, 2006.

[124] H.X. Li and C.P. Buckley. Evolution of strain localization in glassy polymers: A numerical study. *International Journal of Solids and Structures*, 46:1607–1623, 2009.

[125] M. Li, Y.Z. Gu, H. Liu, Y.X. Li, S.K. Wang, Q. Wu, and Z.G. Zhang. Investigation the interphase formation process of carbon fiber/epoxy composites using a multiscale simulation method. *Composites Science and Technology*, 86:117–121, 2013.

[126] G. Lielens, P. Pirotte, A. Couniot, F. Dupret, and R. Keunings. Prediction of thermo-mechanical properties for compression moulded composites. *Composites Part A: applied science and manufacturing*, 29A:63–70, 1998.

[127] B.Y. Low, S.D. Gardner, C.U. Pittman, and R.M. Hackett. A micromechanical characterization of graphite-fiber/epoxy composites containing a heterogeneous interphase region. *Composites Science and Technology*, 52:589–606, 1994.

[128] B.Y. Low, S.D. Gardner, C.U. Pittman, and R.M. Hackett. A micromechanical characterization of thermal stresses in carbon fiber/epoxy composites containing a non-uniform interphase region. *Composites Engineering*, 5(4):375–396, 1995.

[129] D. Lui, N.A. Fleck, and M.P.F. Sutcliffe. Compressive strength of fibre composites with random fibre waviness. *Journal of the Mechanics and Physics of Solids*, 52:1481–1505, 2004.

[130] V. Massardier-Nageotte, A. Maazouz, G. Peix, and S. Bres. Methodologies for the characterisation of glass fibre orientation and distribution in large components

moulded from sheet moulding compounds (SMC). *Polymer Testing*, 22:867–873, 2003.

[131] M. Mohammadi, J.R. Dryden, and L. Jiang. Stress concentration around a hole in a radially inhomogeneous plate. *International Journal of Solids and Structures*, 48:483–491, 2011.

[132] T. Mori and K. Tanaka. Average stress in matrix and average elastic energy of materials with misfitting inclusions. *Acta Metallurgica*, 21:571–574, 1973.

[133] V. Müller, M. Kabel, H. Andrä, and T. Böhlke. Homogenization of linear elastic properties of short-fiber reinforced composites - A comparison of mean field and voxel-based methods. *International Journal of Solids and Structures*, 67-68:56–70, 2015.

[134] D.J. O'Dwyer, N.P. O'Dowd, and C.T. McCarthy. Micromechanical investigation of damage processes at composite-adhesive interfaces. *Composites Science and Technology*, 86:61–69, 2013.

[135] W. Ogierman and G. Kokot. Homogenization of inelastic composites with misaligned inclusions by using the optimal pseudo-grain discretization. *International Journal of Solids and Structures*, 113-114:230–240, 2017.

[136] D. Olmos and J. Gonzalez-Benito. Composites formed by glass fibers and PS-modified epoxy matrix. influence of the glass fibers surface on the morphologies and mechanical properties of the interphases generated. *Polymer Composites*, 31:946–955, 2010.

[137] Committee on the Effectiveness and Impact of Corporate Average Fuel Economy (CAFE) Standards. *Effectiveness and Impact of Corporate Average Fuel Economy (CAFE) Standards*. National Academy Press, Washington, D.C., 2002.

[138] M. Ostoja-Starzewski, I. Jasiuk, W. Wang, and K. Alzebdeh. Composites with functionally graded interphases: mesocontinuum concept and effective transverse conductivity. *Acta Metallurgica*, 44(5):2057–2066, 1996.

[139] O. Pierard, C. Friebel, and I. Doghri. Mean-field homogenization of multi-phase thermo-elastic composites: a general framework and its validation. *Composites Science and Technology*, 64:1587–1603, 2004.

[140] P. Ponte Castañeda. The effective mechanical properties of nonlinear isotropic composites. *Journal of the Mechanics and Physics of Solids*, 39:45–71, 1991.

[141] A. Puck, J. Kopp, and M. Knops. Guidelines for the determination of the parameters in Puck's action plane strength criterion. *Composites Science and Technology*, 62:371–378, 2002.

[142] A. Puck and H. Schürmann. Failure analysis of FRP laminates by means of physically based phenomenological models. *Composites Science and Technology*, 58:1045–1067, 1998.

[143] A. Puck and H. Schürmann. Failure analysis of FRP laminates by means of physically based phenomenological models. *Composites Science and Technology*, 62:1633–1662, 2002.

[144] J. Qu and M. Cherkaoui. *Fundamentals of Micromechanics of Solids*. Wiley, Hoboken, NJ, 2006.

[145] L. Raimondo, L. Iannucci, P. Robinson, and P.T. Curtis. Modelling of strain rate effects on matrix dominated elastic and failure properties of unidirectional fibre-reinforced polymer-matrix composites. *Composites Science and Technology*, 72:819–827, 2012.

[146] J. Richeton, S. Ahzi, K.S. Vecchio, F.C. Jiang, and R.R. Adharapurapu. Influence of temperature and strain rate on the mechanical behavior of three amorphous polymers: Characterization and modeling of the compressive yield stress. *International Journal of Solids and Structures*, 43:2318–2335, 2006.

[147] M. Ricotta, M. Quaresimin, and R. Talreja. Mode I strain energy release rate in composite laminates in the presence of voids. *Composites Science and Technology*, 68:2616–2623, 2008.

[148] R.E. Robertson. Theory for the plasticity of glassy polymers. *The Journal of Chemical Physics*, 44:3950–3956, 1966.

[149] T. Sabiston, M. Mohammadi, M. Cherkaoui, J. Lévesque, and K. Inal. Micromechanics based elasto-visco-plastic response of long fibre composites using functionally graded interphases at quasi-static and moderate strain rates. *Composites: Part B*, 100:31–43, 2016.

[150] T. Sabiston, M. Mohammadi, M. Cherkaoui, J. Lévesque, and K. Inal. Micromechanics for a long fibre reinforced composite model with a functionally graded interphase. *Composites: Part B*, 84:188–199, 2016.

[151] T. Sabiston, P. Pinter, J Lévesque, K.A. Weidenmann, and K. Inal. Evaluating the number of pseudo grains required in a two-step homogenization to predict the response of sheet moulding compound composites from the exact fibre orientation distribution. *Submitted to Composites: Part A*, 2017.

[152] R. Sburlati and R. Cianci. Interphase zone effect on the spherically symmetric elastic response of a composite material reinforced by spherical inclusions. *International Journal of Solids and Structures*, 71:91–98, 2015.

[153] J. Schjødt-Thomsen and R. Pyrz. The Mori-Tanaka stiffness tensor: diagonal symmetry, complex fibre orientations and non-dilute volume fractions. *Mechanics of Materials*, 33:531–544, 2001.

[154] K. Schladitz, A. Büter, M. Godehardt, O. Wirjadi, J. Fleckenstein, T. Gerster, U. Hassler, K. Jaschek, M. Maisl, U. Maisl, S. Mohr, U. Netzelmann, T. Potyra, and M.O. Steinhauser. Non-destructive characterization of fibre orientation in reinforced SMC as input for simulation based design. *Composite Structures*, 160:195–203, 2017.

[155] A.E. Scott, I. Sinclair, S.M. Spearing, M.N. Mavrogordato, and W. Hepples. Influence of voids on damage mechanisms in carbon/epoxy composites determined via high resolution computed tomography. *Composites Science and Technology*, 90:147–153, 2014.

[156] L. Shikhmanter, I. Eldror, and B. Cina. Fractography of unidirectional CFRP composites. *Journal of Materials Science*, 24:167–172, 1989.

[157] F. Sket, R. Seltzer, J.M. Molina-Aldareguia, C. Gonzalez, and J. LLorca. Determination of damage micromechanisms and fracture resistance of glass fiber/epoxy cross-ply laminate by means of x-ray computed microtomography. *Composites Science and Technology*, 72:350–359, 2012.

[158] W.S. Slaughter and N.A. Fleck. Viscoelastic microbuckling of fiber composites. *Journal of Applied Mechanics*, 60:802–806, 1993.

[159] W.S. Slaughter and N.A. Fleck. Microbuckling of fiber composites with random initial fiber waviness. *Journal of the Mechanics and Physics of Solids*, 42:1743–1766, 1994.

[160] P.D. Soden, A.S. Kaddour, and M.J. Hinton. Recommendations for designers and researchers resulting from the world-wide failure exercise. *Composites Science and Technology*, 64:589–604, 2004.

[161] R. Stone and J.K. Ball. *Automotive Engineering Fundamentals*. SAE International, Warrendale, Pa., 2004.

[162] Z. Sun, X. Zhao, X. Wang, and J. Ma. Predicting the elastic properties of sisal fiber reinforced polypropylene composites by a new method based on generalized method of cells and laminate analogy approach. *Composites Science and Technology*, 91:45–49, 2014.

[163] M.P.F. Sutcliffe and N.A. Fleck. Microbuckle propagation in carbon fibre-epoxy composites. *Acta Metallurgica et Materialia*, 42:2219–2231, 1994.

[164] R. Talreja. Defect damage mechanics: broader strategy for performance evaluation of composites. *Plastics, Rubber and Composites*, 38:49–54, 2009.

[165] R. Talreja. Assessment of the fundamentals of failure theories for composite materials. *Composites Science and Technology*, 105:190–201, 2014.

[166] T.A. Tervoort, E.T.J. Klompen, and L.E. Govaert. A multi-mode approach to finite, three-dimensional, nonlinear viscoelastic behaviour of polymer glasses. *Journal of Rheology*, 40:779–797, 1996.

[167] Q.-D. To, G. Bonnet, and D.-H. Hoang. Explicit effective elasticity tensors of two-phase periodic composites with spherical or ellipsoidal inclusions. *International Journal of Solids and Structures*, 94-95:100–111, 2016.

[168] S.W. Tsai. Strength characteristics of composite materials. NASA Contractor Report CR-224, National Aeronautics and Space Administration, 1965.

[169] S.W. Tsai. A survey of macroscopic failure criteria for composite materials. *Journal of Reinforced Plastics and Composites*, 3:40–62, 1984.

[170] S.W. Tsai and E.M. Wu. A general theory of strength for anisotropic materials. *Journal of Composite Materials*, 5:58–80, 1971.

[171] C.L. Tucker III and E. Liang. Stiffness predictions for unidirectional short-fiber composites: Review and evaluation. *Composites Science and Technology*, 59:655–671, 1999.

[172] P. Upadhyaya and S. Kumar. Micromechanics of stress transfer through the interphase in fiber-reinforced composites. *Mechanics of Materials*, 89:190–201, 2015.

[173] L.C.A. van Breemen, T.A.P Engels, E.T.J. Klompen, D.J.A. Senden, and L.E. Govaert. Rate- and temperature-dependent strain softening in solid polymers. *Journal of Polymer Science Part B: Polymer Physics*, 50:1757–1771, 2012.

[174] L.C.A. van Breemen, E.T.J. Klompen, L.E. Govaert, and H.E.H Meijer. Extending the EGP constitutive model for polymer glasses to multiple relaxation times. *Journal of the Mechanics and Physics of Solids*, 59:2191–2207, 2011.

[175] L.J. Walpole. On the overall elastic moduli of composite materials. *Journal of the Mechanics and Physics of Solids*, 17:235–251, 1969.

[176] W. Wang and I. Jasiuk. Effective elastic constants of particulate composites with inhomogeneous interphases. *Journal of Composite Materials*, 32(15):1391–1424, 1998.

[177] I.M. Ward. *Mechanical Properties of Solid Polymers*. John Wiley & Sons, New York, 2 edition, 1983.

[178] C.A. Weeks and C.T. Sun. Modeling non-linear rate-dependent behavior in fiber-reinforced composites. *Composites Science and Technology*, 58:603–611, 1998.

[179] A. Wongsto and S. Li. Micromechanical FE analysis of UD fibre-reinforced composites with fibres distributed at random over the transverse cross-section. *Composites Part A: Applied science and manufacturing*, 36:1246–1266, 2005.

[180] J.J. Wu and C.P. Buckley. Plastic deformation of glassy polystyrene: A unified model of yield and the role of chain length. *Journal of Polymer Science: Part B: Polymer Physics*, 42:2027–2040, 2004.

[181] Y. Xu, Q.-C. He, and S.-T. Gu. Effective elastic moduli of fiber-reinforced composites with interfacial displacement and stress jumps. *International Journal of Solids and Structures*, 80:146–157, 2016.

[182] R.N. Yancey and M.J. Pindera. Micromechanical analysis of the creep response of unidirectional composites. *Journal of Engineering Materials and Technology*, 112:157–163, 1990.

[183] F. Yang and R. Pitchumani. Processing-interphase-property relationship in fiber-reinforced thermosetting-matrix composites. *Polymer Composites*, 26:193–208, 2005.

[184] L. Yang, Y. Yan, Y. Liu, and Z. Ran. Microscopic failure mechanisms of fiber-reinforced polymer composites under transverse tension and compression. *Composites Science and Technology*, 72:1818–1825, 2012.

[185] S. Zhandarov and E. Mäder. Characterization of fiber/matrix interface strength: applicability of different tests, approaches and parameters. *Composites Science and Technology*, 65:149–160, 2005.

[186] H. Zhou, T.L. Attard, K. Dhiradhamvit, Y. Wang, and D. Erdman. Crashworthiness characteristics of a carbon fiber reinforced dual-phase epoxy-polyurea hybrid matrix composite. *Composites: Part B*, 71:17–27, 2015.

[187] M.M. Zhou and G. Meschke. Strength homogenization of matrix-inclusion composites using the linear comparison composite approach. *International Journal of Solids and Structures*, 51:259–273, 2014.

[188] L. Zhuang and R. Talreja. Effects of voids on postbuckling delamination growth in unidirectional composites. *International Journal of Solids and Structures*, 51:936–944, 2014.

APPENDICES

Appendix A

Fibre Orientation Histograms

CT scan analysis was conducted on a plaque of SMC material at three locations. The fibre orientation histograms for the three samples are plotted as discrete pole figures. The colour and size of each point represents the relative fibre volume content for each fibre orientation. The fibre volume contents for the regions of interest are given in Figure 6.5.

Orientation analysis is completed for each sample on a region of 9×9 mm^2 in the X-Y plane of the samples. Histograms are calculated for the 12 regions over the material thickness at discrete points along the Z axis. Figure A.1, Figure A.2 and Figure A.3 show the pole figures for twelve regions over the thickness for samples one, two, and three respectively. Note, that the origin of the azimuth angle is aligned to the X-axis for samples one and two. The Y-axis for sample three is used as the azimuth angle. Almost all fibres are aligned to the $X-Y$-plane, as there are few orientations detected in Z-direction. This is due to the SMC manufacturing process and is true for all three samples. The in-plane fibre orientation distributions change over thickness as seen in Figure A.1, Figure A.2, and Figure A.3.

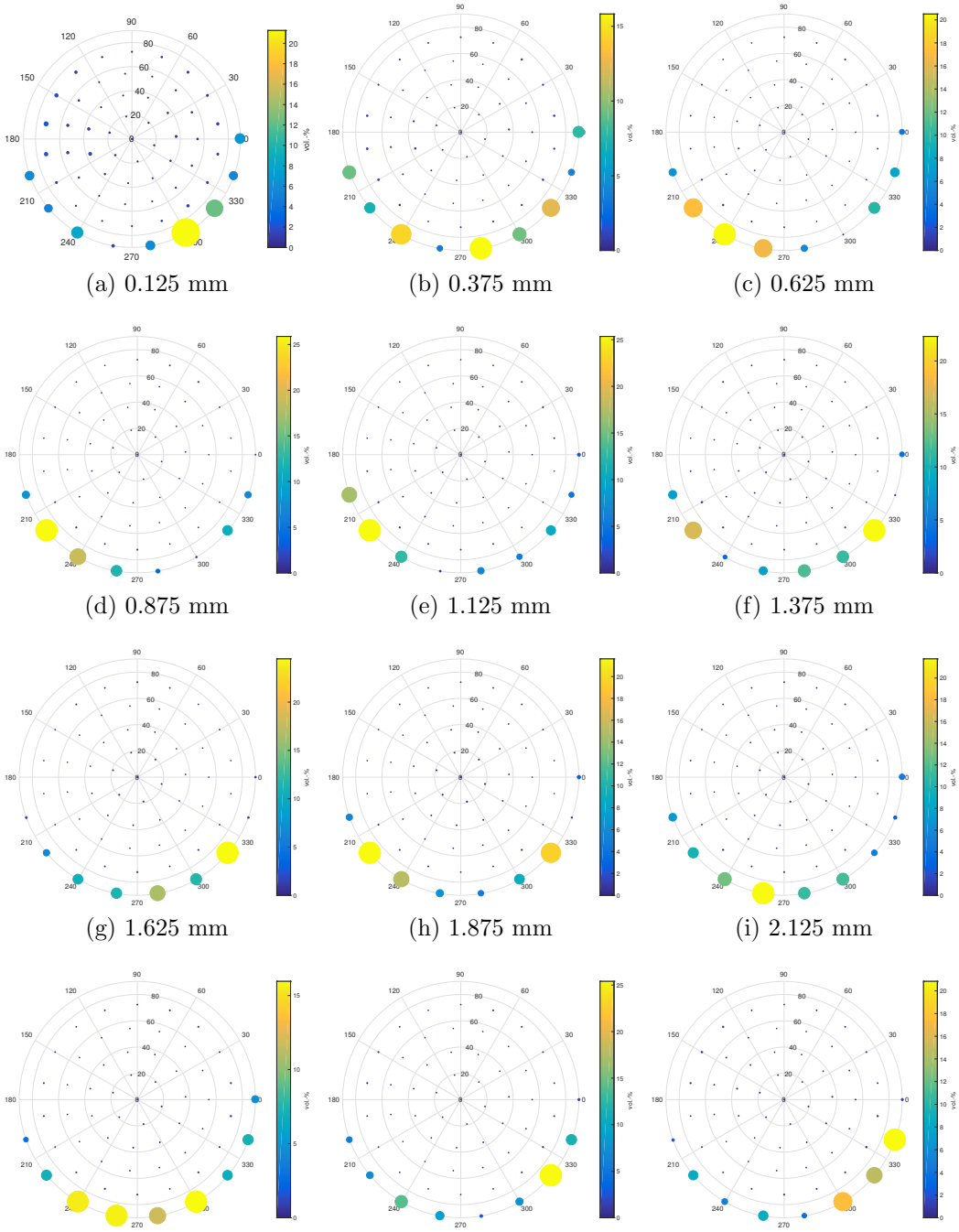

(a) 0.125 mm (b) 0.375 mm (c) 0.625 mm

(d) 0.875 mm (e) 1.125 mm (f) 1.375 mm

(g) 1.625 mm (h) 1.875 mm (i) 2.125 mm

(j) 2.375 mm (k) 2.625 mm (l) 2.875 mm

Figure A.1: Pole figure histograms for sample one with 12 regions over Z. The origin of the azimuth angle is aligned to the X-axis of the global coordinate system in Fig. 6.2 [151].

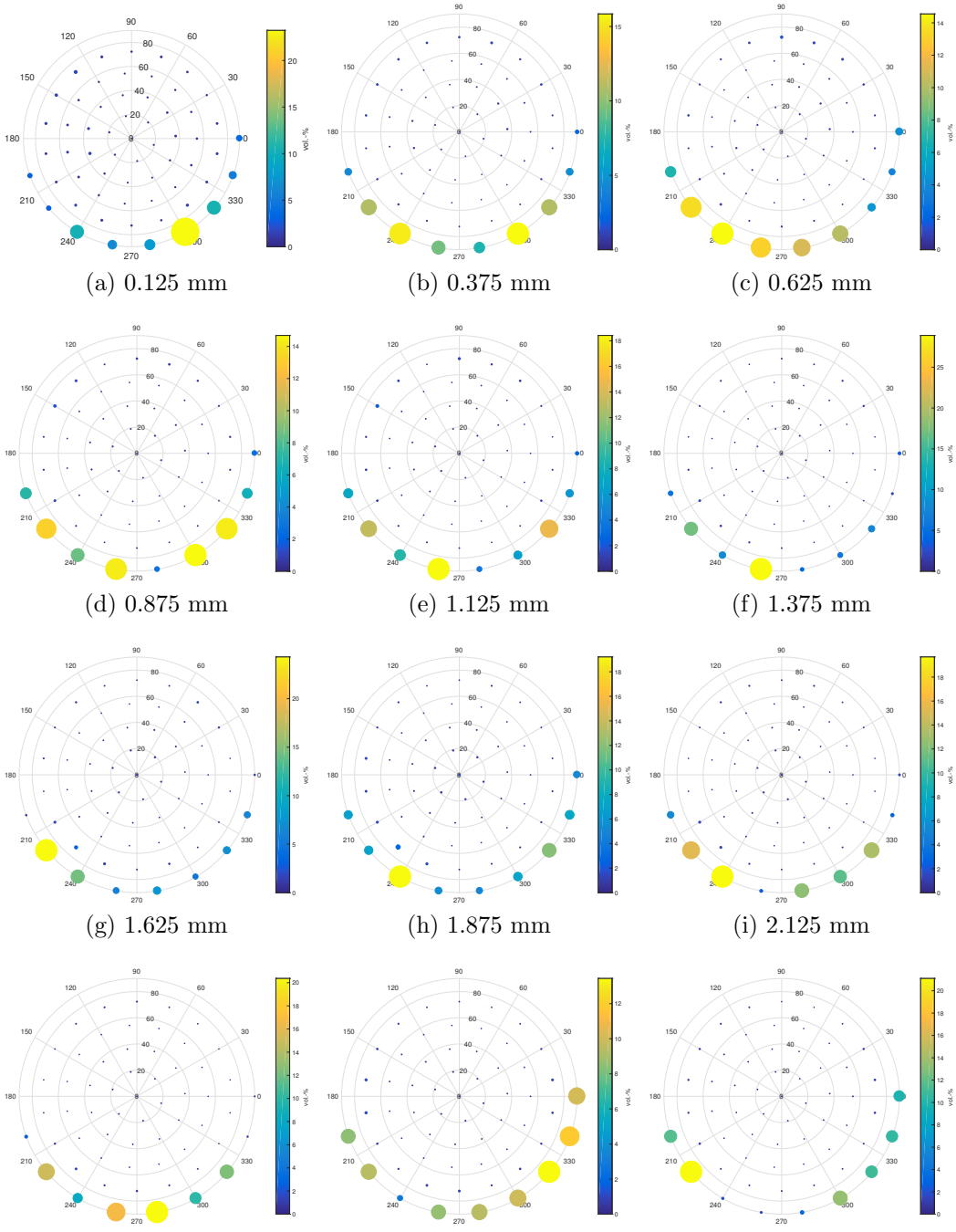

(a) 0.125 mm (b) 0.375 mm (c) 0.625 mm

(d) 0.875 mm (e) 1.125 mm (f) 1.375 mm

(g) 1.625 mm (h) 1.875 mm (i) 2.125 mm

(j) 2.375 mm (k) 2.625 mm (l) 2.875 mm

Figure A.2: Pole figure histograms for sample two with 12 regions over Z. The origin of the azimuth angle is aligned to the X-axis of the global coordinate system in Fig. 6.2 [151].

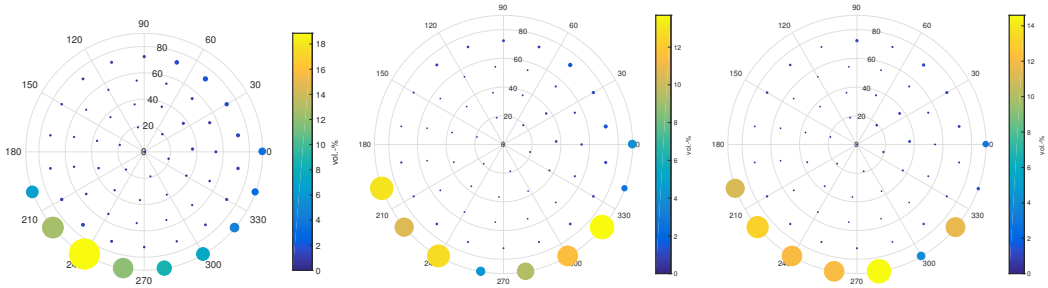

(a) 0.125 mm (b) 0.375 mm (c) 0.625 mm

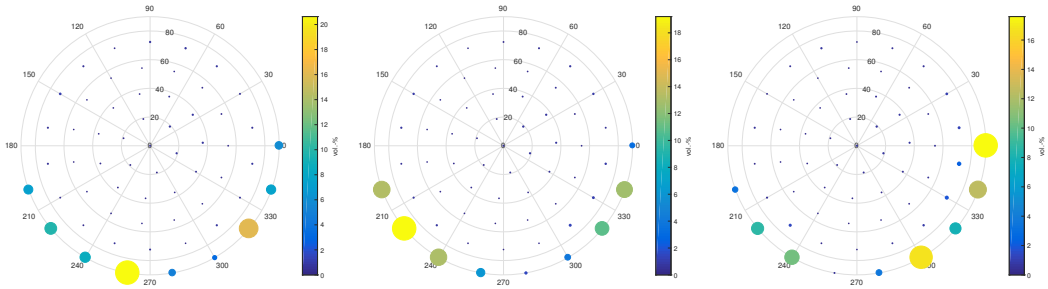

(d) 0.875 mm (e) 1.125 mm (f) 1.375 mm

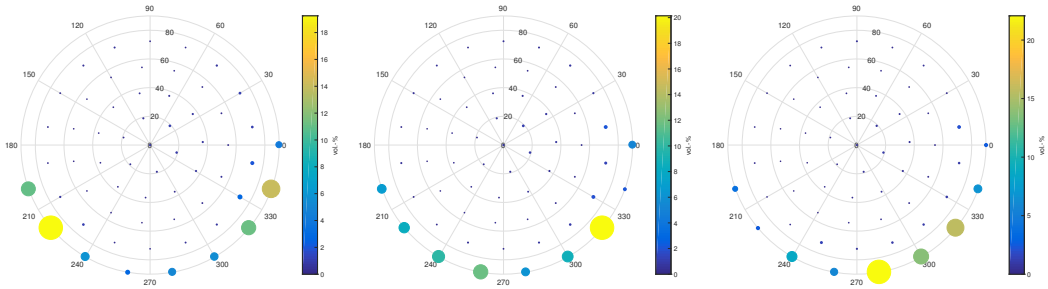

(g) 1.625 mm (h) 1.875 mm (i) 2.125 mm

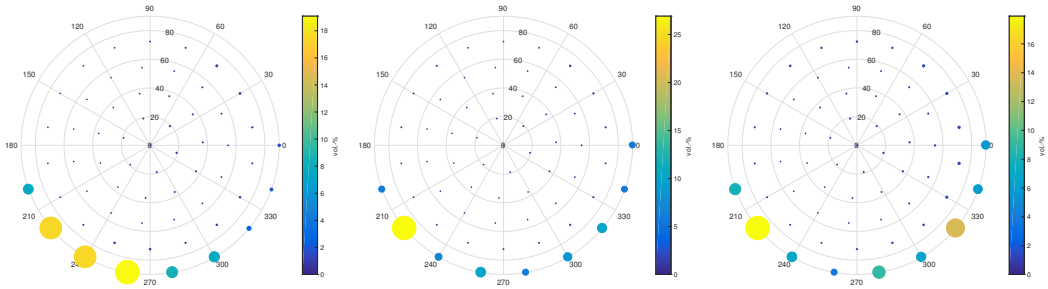

(j) 2.375 mm (k) 2.625 mm (l) 2.875 mm

Figure A.3: Pole figure histograms for sample three with 12 regions over Z. The origin of the azimuth angle is aligned to the Y-axis of the global coordinate system in Fig. 6.2 [151].